



Eidgenössische Technische Hochschule Zürich
Swiss Federal Institute of Technology Zurich

Observability of Forming Planets with Near Future Telescopes

Xueqing Chen

Master Thesis

Department of Physics
Swiss Federal Institute of Technology (ETH) Zurich

Supervision

Prof. Dr. Judit Szulágyi

September 2021

Contents

Abstract	1
1 Backgrounds	2
1.1 Overview	2
1.2 Planet formation in a nutshell	3
1.2.1 Young Stellar Objects	3
1.2.2 Planet formation scenarios	3
1.2.3 Structure of circumstellar disks	5
1.3 Observation of forming planets	6
1.4 Simulation of planet-disk interaction	7
2 Hydrodynamic Simulations	9
2.1 The JUPITER Code	9
2.2 Simulation setup	10
2.3 Output conversion pipeline	11
3 RADMC-3D Radiative Transfer	14
3.1 Basics of radiative transfer	14
3.2 Functionalities of RADMC-3D	16
3.3 Running RADMC-3D	16
3.3.1 Model setup	16
3.3.2 Running from command line	18
3.3.3 Tips and tricks	18
4 Simulating Telescope Images	21
4.1 Overview of near future telescope and instruments	21
4.1.1 James Webb Space Telescope	21
4.1.2 ELT	22
4.1.3 Giant Magellanic Telescope	22
4.2 Telescope simulators in detail	23
4.2.1 Mirage	23
4.2.2 MIRISim	27
4.2.3 SimCADO and SimMETIS	30
4.2.4 GMT simulation routine	32

5 Results	35
5.1 Synthetic images	35
5.2 Predicted magnitudes	35
5.3 Results for each instrument	37
5.3.1 JWST/NIRCam	37
5.3.2 JWST/NIRISS	38
5.3.3 JWST/MIRI	38
5.3.4 ELT/MICADO	39
5.3.5 ELT/METIS	40
5.3.6 GMT/GMTIFS	40
5.4 Discussion	40
6 Conclusion	66
Acknowledgement	68

Abstract

Planets are formed in circumstellar disks around young stars. It is believed that the planets form their sub-disk, the so-called circumplanetary disk (CPD) from ongoing gas accretion to the forming giant planet. There are only few observations of forming planets and their disks to date. Hydrodynamic simulations serve as an important tool to study the interaction between planet and disk and to bridge the gap between theory and observation.

This thesis aims to address how well we can observe forming giant planets with the imaging instruments of near future telescopes including JWST, ELT and GMT. We combine the results from 3D hydrodynamic simulations of forming planets with various masses and separations with 3D radiative post-processing to produce intensity images, which are then processed by the specific instrument simulators to create synthetic observation images in a wide range of filters in near-IR and mid-IR.

We found that 10- and 5-Jupiter mass planets can be observed by all near-IR and mid-IR instruments in most of their filters, whereas 1-Jupiter and Saturn mass planets require wavelength longer than $15\ \mu\text{m}$. In the near-IR, we found that the best observability is achieved in longer wavelengths, such as F356W and F444W for NIRCam & NIRISS on JWST and K band for ELT/MICADO and GMT/GMTIFS. JWST/MIRI and ELT/METIS are both able to image massive giant planets in N band around $10\ \mu\text{m}$, and MIRI will provide unique chances to image less massive giant planets above $15\ \mu\text{m}$. Finally, the observed planet fluxes and predicted magnitudes as well as the detection Signal-to-Noise ratios for each instrument are presented.

Chapter 1

Backgrounds

1.1 Overview

One of the goal of astronomy is to reveal the origin of ourselves and answer the ultimate question: are we alone in the universe? By studying planets around other stars and their formation processes, we can get closer to answering these long sought-after questions.

Since the first detection of an extrasolar planet around a pulsar in 1992 (Wolszczan & Frail) and the discovery of first planet orbiting another solar-like star by Mayor & Queloz (1995), astronomers has now discovered 4834 confirmed exoplanets in 3575 planetary systems (as of Aug 2021)¹, with various masses, orbits and chemical compositions. The birthplace of these planets, the circumstellar disks, have been imaged and characterized thoroughly in the past decade (e.g. Andrews et al. 2018). It is now believed that the young planets also forms a sub-disk from gas accretion onto themselves, the so-called circumplanetary disks (e.g. Quillen & Trilling 1998; Kley 1999; Lubow & D'Angelo 2006; Ayliffe & Bate 2009, 2012). Traces of emission from the sub-disk surrounding the planets have been found (e.g. Kraus & Ireland 2011; Sallum et al. 2015), and our current instruments are just beginning to detect bona fide these circumplanetary disks (Isella et al. 2019; Benisty et al. 2021). The next generation telescopes such as the James Webb Space Telescope (JWST) and Extremely Large Telescope (ELT) will offer a chance to image planets and their forming regions in unprecedented details, and provide insights that may revolutionize the current theory of planet formation.

This thesis aims to address the question of how well can we observe forming giant planets with these near future telescopes. To reach this goal, synthetic observation images are made from high resolution hydrodynamic simulations followed by radiative post-processing, and magnitude tables for an observation parameter space are calculated.

In this first chapter, the theoretical backgrounds of planet formation is briefly introduced, as well as the advances in this research field. In chapter 2, the hydrodynamic code used to model the circumstellar disks is described. The physical model

¹<http://exoplanet.eu/catalog/>

and numeric methods of the code are briefly introduced, followed by the processing method of the code output files. In chapter 3, the radiative post-processing step is described, with a focus on the usage of RADMC-3D code. Chapter 4 presents the details of how mock observations of the key imaging instruments in the near future are created using the existing simulators or self-made routines. The result images are presented in chapter 5, along with calculated magnitude tables, so that they can serve as a reference for future astronomer planning their observations. Chapter 6 summarizes the work and gives a discussion on the limitations of this work and the future directions to work on.

1.2 Planet formation in a nutshell

1.2.1 Young Stellar Objects

A star is born from the collapse of massive, dense molecular clouds. In its different evolutionary stages, the young stellar object (YSO) exhibits distinct characteristics in its spectral energy distribution (SED). In the beginning, the pre-stellar core is surrounded by a massive, accreting envelope. The SED of YSO in this phase (Class 0 object) resembles that of a cold blackbody peaking in the sub-mm wavelengths. In the next phase, an accretion disk forms around the core due to the initial angular momentum in the cloud. Gas spirals inwards, feeding and heating up the core, while angular momentum is transported outwards. In these Class I objects, most radiation from the core is absorbed and re-emitted in far-IR by the surrounding dust. The SED is then composed of a warmer blackbody from the core and a large excess in far-mid IR. As the object evolves, the accretion decreases. In the SED of Class II objects, the main energy comes from the central star as a warm blackbody, while there are still some excess in the near-mid IR from dust in the circumstellar disk. These objects are also known as T Tauri stars. In the last stage, gas dissipated away and only a little dust is left around. The disk becomes optically thin and the SED has little or no excess in IR. A diagram of these evolution stages and their corresponding SEDs are shown in Fig 1.1.

1.2.2 Planet formation scenarios

Exoplanets have been detected from around the mass of Earth to more than 10 times the mass of Jupiter, and with orbital periods from days to million years. Some planets are the so-called terrestrial planets made of rocky materials, while others are giants that have a solid core and gaseous envelope. The vastly different characteristics of existing planets suggests that they are formed in different ways.

Rocky planets mainly form via collision of dusts and rocky materials. They can form slower as they can still grow without existing gas in the disk. On the other hand, gas giants need to form before gas are dissipated away, in 3-5 Myrs. There are two proposed mechanism for the formation of gas giants: Disk instability and core accretion. They operate in different regimes and can result in planets with

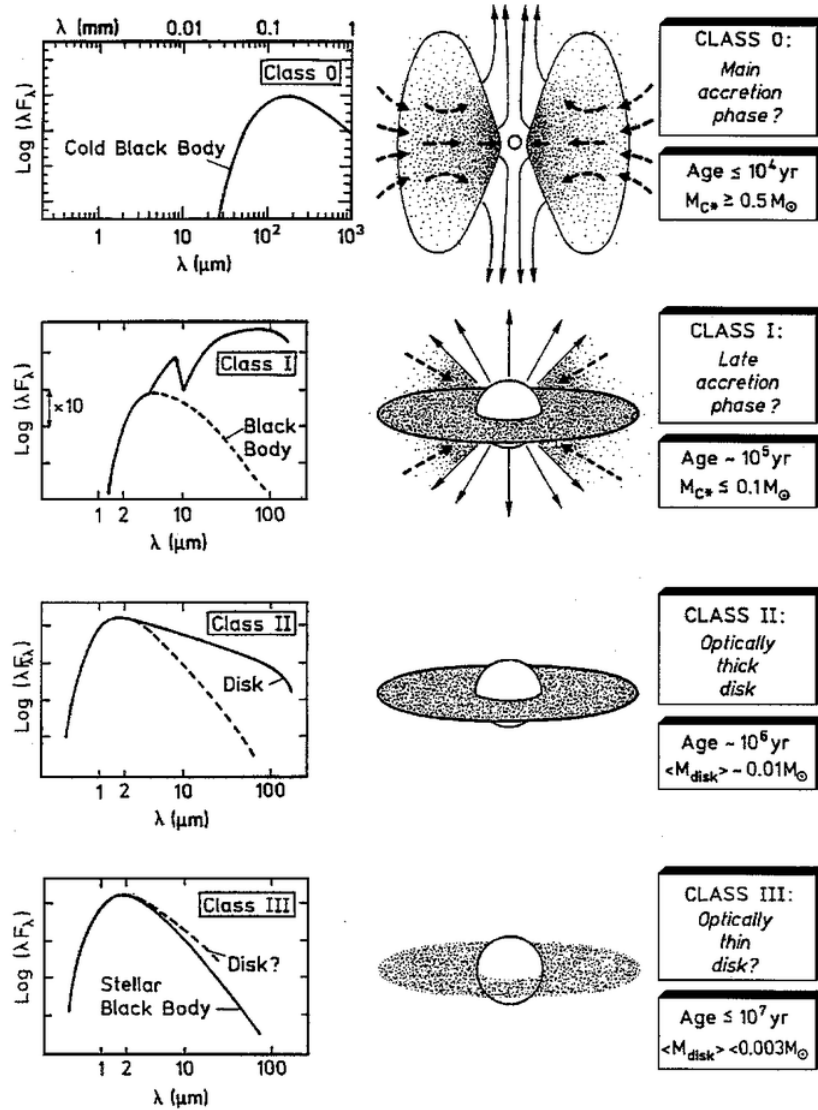


Figure 1.1: The evolution stages of young stellar objects. Taken from Palla (1996).

different masses and locations.

In the disk instability model, proto-planets are formed via gravitational instability of gas. They create arms and clumps in the disk, which then collapse to form proto-planets (Boss, 1997). This mechanism requires a massive disk, so it happens in the early stage (Class 0 or Class I objects). The Toomre criterion (Toomre, 1964) is usually used to measure whether a disk is gravitationally unstable. Gravitational instability usually only happen in the outer part of disk, so this mechanism can explain planets that has a wide orbit.

In general, the most accepted formation mechanism is core accretion (Pollack et al., 1996). This is also the mechanism that is considered in the hydrodynamic simulation used in this work. It happens in three phases: First is solid core coagulation, where a rocky core of $\sim 10 M_{Earth}$ builds up. The phase is ended when

the proto-planet is massive enough to empty its feeding zone. In the second phase of slow envelope accretion, the gravity of planet is big enough to accrete gas. The envelope is in a state of hydrostatic equilibrium, which can be described by a set of hydrodynamic and radiative equations that can be numerically solved. This phase is the longest and can last some Myrs. In the third phase of runaway gas accretion, the hydrostatic equilibrium is broken and the accretion of gas goes exponential. There are still unsolved problems regarding this model, including its unclear stopping mechanism, the long timescale needed compared to disk lifetime, and problem with mass distribution of giant planets formed this way. Some of the problems can be addressed with models like pebble accretion or formation of a circumplanetary disks around the proto-planet. The gas giants formation mechanism is a rapidly evolving field of research, and new observations can greatly help constraining the current models.

1.2.3 Structure of circumstellar disks

From the previous section we know that planets are formed in dust and gas disks surrounding young stars, i.e. the circumstellar disks (CSD). Therefore, understanding the physics of these disks are key to the study of forming planets.

The vertical structure of disks can be modeled assuming an equilibrium between the gravitational and pressure forces. With an isothermal equation of state $P = c_s^2 \rho$, the balance can be written as

$$c_s^2 \frac{d\rho}{dz} = -G \frac{M_* z}{r^3} \quad (1.1)$$

where c_s is the isothermal speed of sound, ρ the gas density, z the vertical distance from midplane, r the radial distance from star, G the gravitational constant and M_* the mass of star. For an isothermal thin disk, c_s is vertically constant and $z \ll r$. The solution is then

$$\rho(z) = \rho_0 \exp\left(-\frac{z^2}{2H^2}\right) \quad (1.2)$$

where ρ_0 is density at midplane and $H = \frac{c_s(r)}{\sqrt{GM_*/r^3}}$ is the disk *scale height*. Note that it is in the form of a Gaussian function with exponential fall-off, which we will later use for density extrapolation. The *aspect ratio* of the disk is H/r .

The radial structure of the disk can be described by its *surface density*, defined by vertically integrating the density,

$$\Sigma(r) = \int_{-\infty}^{+\infty} \rho(r, z) dz \quad (1.3)$$

Another important disk parameter related to the surface density is the *viscosity* ν , which is believed to mainly arise from the turbulence of disk. One result that the rotation of disks approximately follows Kepler's law is that the velocity of rotation varies at different radius, i.e. differential rotation. Thus, the neighbouring rotating rings will experience a friction force due to the presence of viscosity. This effect

is important in the modelling of disk dynamics. A widely used parametrization of viscosity proposed by Shakura & Sunyaev (1973), i.e. the α -viscosity prescription, links the viscosity to sound speed by $\nu = \alpha c_s H$, where α is a dimensionless constant.

Since planets forms also from infalling gas with angular momentum like the stars themselves, it is believed that a sub-disk also forms around these planets, called the circumplanetary disk (CPD), where the moons of the planets eventually form. Studies have shown that the accretion from CSD to the CPD are dominated by a vertical inflow, which determines the shape of CPD (Szulágyi et al., 2014). The high velocity influx creates a hot shock front above the CPD surface, which may be observed as a hot spot at the planet location. In this case, detecting an embedded planet is actually detecting its CPD. Other substructures in the CSD like spiral arms and gaps are also believed to link with the forming planets. These substructures of circumstellar disks have only recently been observed and also studied in detail by numerical models. These progress will be introduced in the following sections.

1.3 Observation of forming planets

Since the 1990s, circumstellar disks has been intensively observed from optical/near-IR to sub-mm wavelengths, resulting in few hundreds of resolved disk observations till now (Aug 2021)². In the past decade, thanks to the advancement of high contrast imaging instruments like VLT/SPHERE and the revolutionary Atacama Large Millimeter/submillimeter Array (ALMA), CSDs can be studied and characterized in details, revealing the rich substructures in the disk, such as gaps, rings, spirals and asymmetries (e.g. see Ansdell et al. 2017, Andrews et al. 2018).

On the other hand, the direct observation of forming planets or circumplanetary disks embedded in the CSD are scarce. A first claimed detection is LkCa 15 b by Kraus & Ireland (2011) with an age of ~ 2 Myrs, followed by the candidates LkCa 15 c and d found by Sallum et al. (2015). A younger planet of about 1 Myr age, HD 100546 b, was confirmed by Quanz et al. (2015) through direct imaging techniques. There is also a planet candidate around HD 169142 discovered by Reggiani et al. (2014) and around MWC 758 by Reggiani et al. (2018). However, the planetary nature of most of the detected sources remain in controversy. Keppler et al. (2018) reported the first robust detection of a young planet still embedded in its disk, the now-famous PDS 70 b, and followed by a confirmation of another young planet PDS 70 c Mesa et al. (2019). Only very recently, the first clear signatures of a circumplanetary disk around the planet PDS 70 c are observed with ALMA (Isella et al., 2019; Benisty et al., 2021). The stunning image of the circumplanetary disk of PDS 70 c is shown in Fig 1.2.

²<https://www.circumstellardisks.org/>

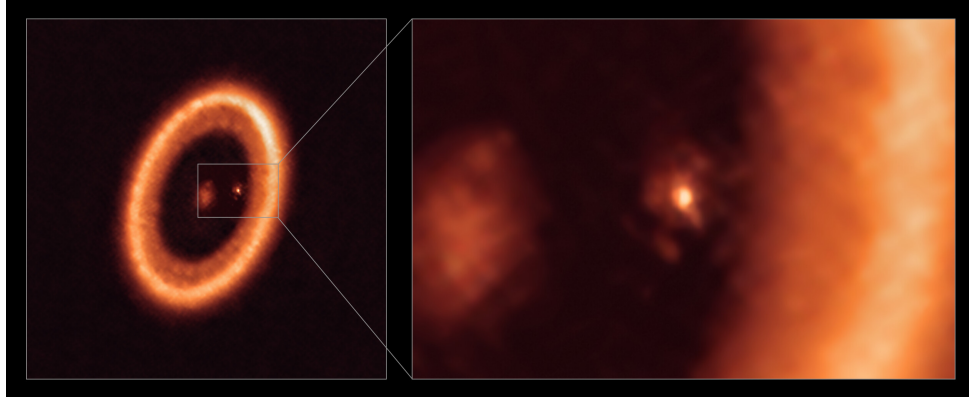


Figure 1.2: Image of the circumplanetary disk around PDS 70 c taken with ALMA.
Source: Benisty et al. (2021)

1.4 Simulation of planet-disk interaction

Due to the small number of young planet observations, numerical simulation of the disk serves as an important tool to study the interaction between planet and disk, which allows better interpretation of the observed disk structures. There are many different processes that goes on in a planet-forming disk, such as gravity, dust and gas dynamics, radiation, magnetic fields and chemistry, etc, which make the accurate modelling of a circumstellar disk an extremely challenging job. Often in a simulation, only the most relevant processes are included, which are gas and dust dynamics and radiative processes in the case of young planet observation. To model these processes, computational fluid dynamics (also called hydrodynamics) is needed.

Current hydrodynamic numerical methods are developed in two approaches. The first is the *grid-based* approach or *Eulerian* approach, where the computational is carried out discrete cells and the hydrodynamic fields evolve in time. The other is the *Lagrangian* approach where the co-ordinates move with the fluid, an example of which widely used in astrophysical simulation is Smoothed-particle hydrodynamics (SPH). In this work, we use the simulation results from the JUPITER code, which is a grid-based hydrodynamic code with Godunov-type solvers. This type of solver works well in situations involving shock fronts because of the usage of Riemann solvers, so it is most suitable for our science case of modelling circumplanetary regions.

With the density and temperature distribution of gas and dust in the disk obtained from simulation, synthetic observations can be made to predict observability and provide guidance for planning and interpreting real observations. Often the hydrodynamic fields are run through a radiative transfer post-processing code to calculate the observed flux distribution from a viewing angle. Wolf & D'Angelo (2005) studied the detectability of embedded planets by ALMA from 2D hydrodynamical simulations. Ertel et al. (2012) studied planet-disk interaction in debris disks with analytical models and N-body simulations, and created simulated images for HST/ASC and JWST/MIRI with simple PSF residual addition/PSF convolu-

tion. Observations in polarized scattered light are simulated in [de Juan Ovelar et al. (2013)] for VLT/SPHERE and Subaru/HiCIAO with 2D simulations. [Perez et al. (2015)] adopted 3D SPH simulation to show that CPDs are detectable by ALMA via signposts from gas kinematics. Disk features such as gaps opened by planets and spirals induced by gravitational instability are simulated by [Dong et al. (2015b)], [Dong et al. (2015a)], and observed disk morphology from varying viewing angles are further investigated in [Dong et al. (2016)]. [Zhang et al. (2018)] modeled disks from the ALMA DSHARP project for interpreting the observed disk substructures and inferred embedded planet mass from the gap properties. The study of [Isella & Turner (2018)] highlighted the importance of vertical temperature profile on the observability of planet-disk interactions. In the three consecutive paper by [Szulágyi et al. (2017), (2019); Szulágyi & Garufi (2021)], the observability of CPD is studied in sub-mm, near-IR and polarized scattered light with radiative effect-included 3D hydrodynamic simulations. This work is a continuation of the previous works by [Szulágyi et al.], adopting the same hydrodynamic simulation and processing methods but extending the scope of study to future telescopes. The results of this study would benefit the astronomy community by providing better understanding of what we can expect from these new instruments about discovering planets in formation.

Chapter 2

Hydrodynamic Simulations

2.1 The JUPITER Code

The hydrodynamic simulation models used in this work are computed by the three-dimensional, grid-based code JUPITER, developed by F.Masset and J. Szulágyi. It uses a higher order Godunov scheme and nested meshes to solve the hydrodynamic equations of circumstellar disk evolution. The adaptive mesh refinement (AMR) grids allows a highest spatial resolution of about 0.8 Jupiter radii at the forming planet's vicinity. A radiative module is also built in JUPITER to account for realistic thermal effect in the disk. The gas can heat due to stellar irradiation, viscous heating and adiabatic compression caused by accretion onto planet, while it can cool through radiation and adiabatic expansion. The governing equations of the code are as listed in Szulágyi et al. (2016), the first two equations are mass and momentum conservation, Eq 2.3 is the energy equation, and Eq 2.4 describes the coupling between thermal energy and radiation energy ϵ_{rad} :

$$\frac{\partial \rho}{\partial t} + \nabla \cdot (\rho \mathbf{v}) = 0 \quad (2.1)$$

$$\frac{\partial(\rho \mathbf{v})}{\partial t} + \nabla \cdot (\rho \mathbf{v} \otimes \mathbf{v}) + \nabla P = -\rho \mathbf{v} \cdot \nabla \Phi + \nabla \cdot \bar{\tau} \quad (2.2)$$

$$\frac{\partial E}{\partial t} + \nabla \cdot [(P \bar{\mathbb{I}} - \bar{\tau}) \cdot \mathbf{v} + E \mathbf{v}] = \rho \mathbf{v} \cdot \nabla \Phi - \rho \kappa_R c \left[\frac{B(T)}{c} - \epsilon_{\text{rad}} \right] \quad (2.3)$$

$$\frac{\partial \epsilon_{\text{rad}}}{\partial t} = -\nabla \cdot F_{\text{rad}} + \rho \kappa_R c \left[\frac{B(T)}{c} - \epsilon_{\text{rad}} \right] \quad (2.4)$$

where ρ is gas density, \mathbf{v} is the gas velocity vector, P is pressure, ϕ is the gravitational potential, E is the total energy per unit volume, i.e. the sum of internal energy and kinetic energy of the gas, c is speed of light, κ_R is the Rossland mean opacity as defined in Bitsch et al. (2013), $B(T) = 4\sigma T^4$ is the thermal blackbody radiation with σ being the Stephan-Boltzmann constant, $\bar{\mathbb{I}}$ is the identity tensor, and $\bar{\tau}$ is the stress tensor defined as

$$\bar{\tau} = 2\rho\nu \left[\bar{\mathbb{D}} - \frac{1}{3}(\nabla \cdot \mathbf{v})\bar{\mathbb{I}} \right] \quad (2.5)$$

where ν is the kinematic viscosity and \bar{D} is the strain tensor. Moreover, the radiative flux F_{rad} is given by the flux-limited diffusion approximation

$$F_{\text{rad}} = -\frac{c\lambda}{\rho\kappa_R} \nabla \epsilon_{\text{rad}} \quad (2.6)$$

where λ is a flux limiter that takes care of the transition between optically thick and thin regimes. It approaches to $F = 4\sigma T^4/c$ in optically thick regime and approaches $\lambda = 1/3$ in the optically thick regime. Finally, the equation of state used to close the system is

$$P = (\gamma - 1)\epsilon \quad (2.7)$$

where $\gamma = 1.43$ is the adiabatic index and $\epsilon = \rho c_v T$ is the gas internal energy. In each time step, the above equations are solved in sub-steps and the primitive variables in the code, i.e., the gas density, the three components of the velocity, and the internal energy are updated. For a more detailed description of the physical model and numerical methods used in the JUPITER code, see the Ph.D. thesis of J. Szulágyi¹ and the paper by Szulágyi et al. (2016).

2.2 Simulation setup

In this thesis, 7 simulations are run in a parameter space covering planetary mass of 1 Saturn, 1 Jupiter, 5 Jupiter and 10 Jupiter at 50 AU from star, and planetary mass of 1 Jupiter, 5 Jupiter and 10 Jupiter at 30 AU from star. The simulation setup are same as described in Szulágyi et al. (2016). The stellar properties are chosen to be the same as the Sun. The circumstellar disk has a mass of $10^{-2} M_{\text{Sun}}$ and an initial surface density slope of -0.5. The mean molecular weight is 2.3, chosen according to the solar abundances. A constant kinematic viscosity of $10^{-5} a_P \Omega_P$ is used, where a_P is the planet semi-major axis and Ω_P the orbital frequency.

As mentioned before, the JUPITER code has nested mesh grids that use adaptive mesh refinement (AMR) to reach a high resolution at a predefined planet region. In this simulation, four levels of refinements (not including the base layer) are used, each doubling the resolution in all three spatial directions, so that the planet's Hill sphere is well-resolved in the final layer. The grid is in spherical coordinate system. In the base layer, the disk has an opening angle of 7.4 degrees from the midplane in the co-latitude direction spanning 20 cells. In the azimuthal direction it spans over 2π with 680 cells. In the radial direction, the disk extends between 0.4-2.4 times of the planet's semi-major axis (30 or 50 AU) in 215 cells. In reality, gas in circumstellar disks is still present inside the grid inner boundary defined here, but they does not affect the planet's vicinity, and thus are excluded from the simulation to save computation time. For a visualization of the AMR grid layers used in the simulation, see Fig 2.1.

The dust-to-gas ratio is set to a constant 0.01 in the simulation. Although the dust is not explicitly treated in the gas hydrodynamics, their effect is taken into

¹<https://people.phys.ethz.ch/~judits/thesisszulagyi.pdf>

Simulation	a_P (AU)	M_P (M_{jup})
10jup50au	50	10.0
5jup50au	50	5.0
1jup50au	50	1.0
1sat50au	50	0.3
10jup30au	30	10.0
5jup30au	30	5.0
1jup50au	30	1.0

Table 2.1: Parameters of the 7 simulations.

account through the dust opacities. The opacity table used that contain both dust and gas opacities are taken from Bell & Lin (1994). In each cell during calculation, the code uses the density and temperature of that cell to decide what opacity value to use. Above the evaporation temperature of the dust species, opacity is given by the gas opacities.

The set of 7 simulations and the parameters used are summarized in Table 2.1.

2.3 Output conversion pipeline

The JUPITER code output files are in complex structures because of the use of AMR grids. The result of a simulation is saved in separate files: The simulation parameters and grid information including AMR layers are saved in a descriptor file, with the coordinate of cell vertices listed in the order of ϕ (azimuthal), r (radial) and θ (co-latitude). Each output hydrodynamic field is saved in a data file with the value of the cell barycenter listed in an order corresponding to that of the descriptor file.

A pipeline is needed for converting the JUPITER output files to formats that allows visualization with other programs or in the case of this work, for further radiative post-processing using RADMC-3D. An output conversion code DATtoRADMC is mainly developed by Pablo Rutschmann as his semester project. A few functionalities are initially coded by me, which I will briefly introduce here. For a description of how to use the python class DATtoRADMC, see <https://github.com/pablorutschmann/DATtoRADMC>.

The pipeline first calculates the conversion factor for converting the selected hydrodynamic fields into physical units. In JUPITER the fields are computed in code units, where mass is in stellar masses, time is in orbital period of the planet, and length is the orbital separation of the planet, etc, so conversion is dependent on the specific simulation setup. Then, the grid and hydro field data are reordered according to RADMC-3D requirements and written to required input formats. In this step, a few important manipulations are applied to the hydro fields:

1. The simulation is only done on one side of the disk midplane, assuming that the distribution of hydrodynamic fields is symmetric about the midplane. Thus, the output fields are mirrored across the midplane, so that it now extends 40 cells

vertically.

2. An extension of the fields in co-latitude direction into the disk atmosphere is needed if one is to perform radiative transfer calculation on the model. This is because in the near IR, scattering of photons off dust grains has a significant effect on the brightness of circumstellar disks. This process is most important in the circumstellar disk atmosphere where the dust is optically thin. However, the hydro solver tends to fail in regions where the value of hydro field is too low. So, the simulation only models the disk within an opening angle of 7.4 degrees and the atmosphere at higher latitude is excluded. To include the scattering effect of the atmosphere, the output hydro fields are extended by 30 cells on both sides of the vertical direction, so that it now extends 100 cells vertically. For the density field, the extended cells are filled with Gaussian extrapolated values, i.e., for each vertical column of 40 cells of the density field, we fit a 3-parameter Gaussian function of the form

$$\rho(z) = a \cdot \exp\left(-\frac{(z - b)^2}{2c^2}\right) \quad (2.8)$$

where z is the vertical coordinate. The initial guess for the parameters a, b, c are taken to be the maximum density of the column, the vertical coordinate of midplane (2π), and $H/\sqrt{2}$ (H is the scale height of the disk) respectively. In testing of the code, we found that a close initial guess improves the convergence of fitting. We also imposed a condition on the fitting residual of the first and last cell of the column, such that the transition between existing and extrapolated cells is smooth without abrupt density changes. This is done by manually setting a weighting array for the `sigma` argument in the `scipy.optimize.curve_fit` function. The fitted Gaussian parameters are then used to extrapolate the value for the extended cells. For the temperature field, the extension is simply done by copying the value of the first and last cell to fill the extended cells. This ensures that stellar irradiation is taken into account for the disk atmosphere. The density and temperature field of a simulation after mirroring and extension is shown in Fig 2.1.

3. Finally, dust evaporation is taken into account by setting dust density to zero for cells with temperature higher than the sublimation point of the dust species, i.e. 1500K.

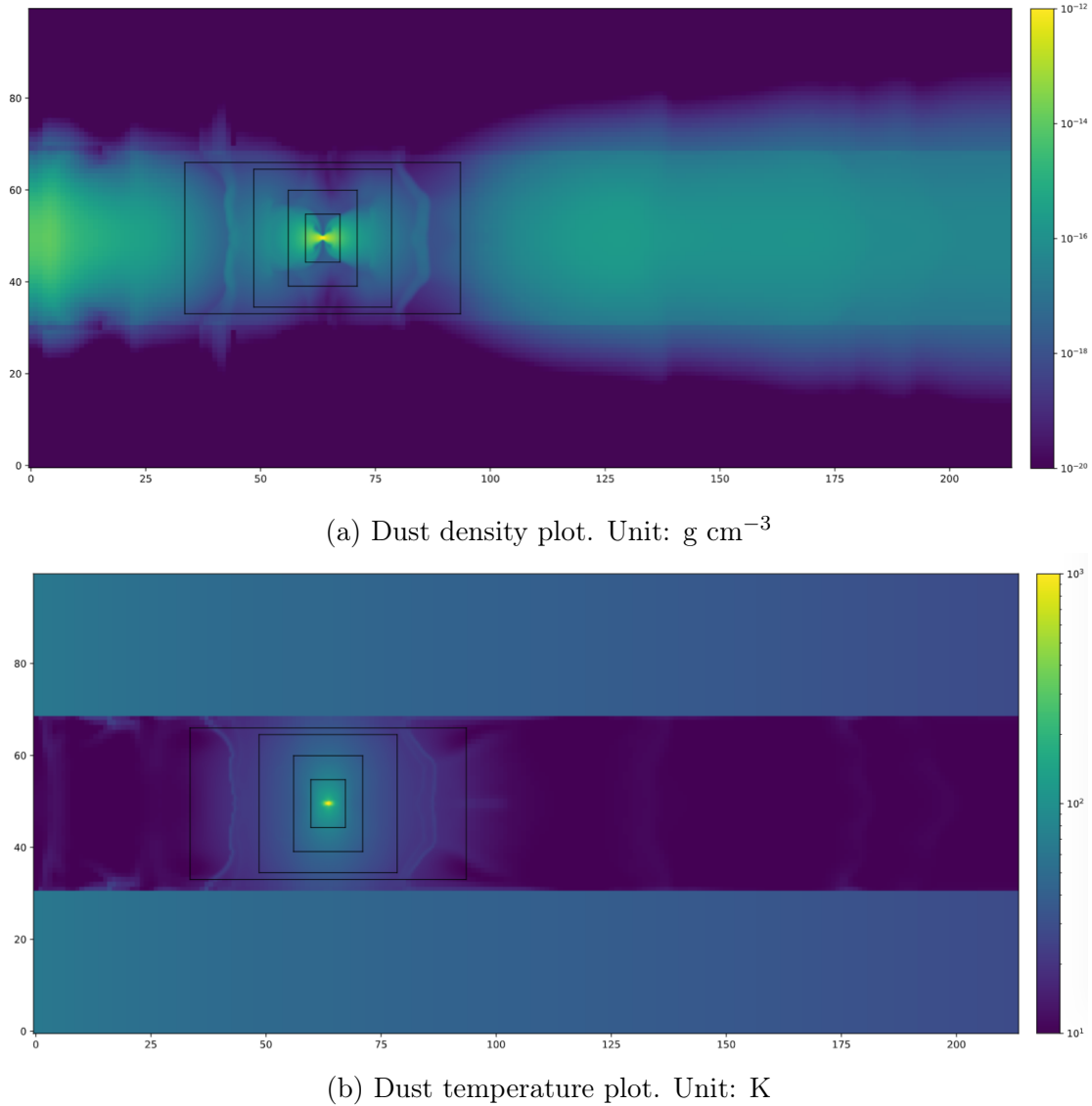


Figure 2.1: Plots showing a meridional slice of the 3D hydrodynamic fields at the planet location, with the boundaries of the 4 AMR layers in co-latitude and radial directions marked as black boxes. The extension of the fields in vertical direction beyond the central 40 cells is also seen in the plots.

Chapter 3

RADMC-3D Radiative Transfer

In JUPITER code, radiative treatments are included, but the use of an average opacity (i.e., the Rossland mean opacity) over the whole spectrum leads to wavelength-independent results. In order to simulate observations of circumstellar disks at multiple wavelengths covered by the instruments of our interest, wavelength-dependent intensity images are needed. Therefore, the JUPITER output needs to go through a radiative post-processing, which can be done by the radiative transfer calculation code RADMC-3D. In this chapter, the steps to run RADMC-3D for the models in this work is described. For the understanding of a few concepts mentioned, some basics of radiative transfer calculation is first introduced.

3.1 Basics of radiative transfer

The radiative transfer problem describes the change of specific intensity I_ν along the ray path ds in the presence of medium, as illustrated in Fig 3.1. The interaction between light and the medium leads to either absorption, emission or scattering.

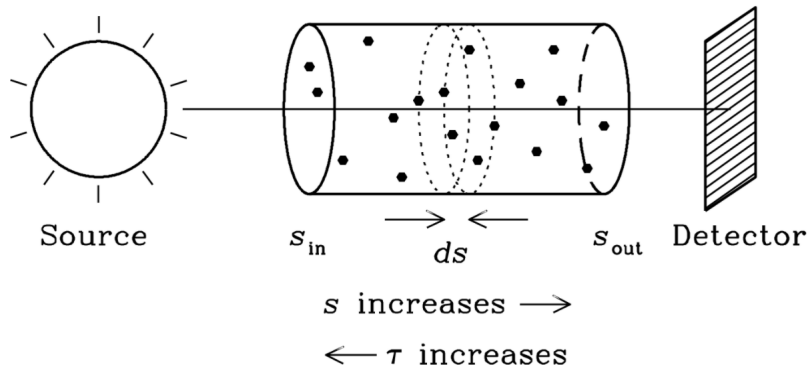


Figure 3.1: Radiative transfer between a source and a detector. Taken from <https://www.cv.nrao.edu/~sransom/web/Ch2.html#F7>

The loss of intensity due to absorption is (absorption is proportional to intensity)

$$dI_\nu = -\alpha_\nu I_\nu ds \quad (3.1)$$

where $\alpha_\nu = \kappa_\nu \rho$ is the absorption coefficient. ρ is the density distribution of the medium species, and κ_ν its opacity (in cm^{-1}). Integrating along ds gives

$$\begin{aligned} I_\nu(s) &= I_\nu(s_0) \exp\left(-\int_{s_0}^s \kappa_\nu \rho ds\right) \\ &= I_\nu^o e^{-\tau_\nu} \end{aligned} \quad (3.2)$$

where the dimensionless quantity

$$\tau_\nu(s_0, s) = \int_{s_0}^s \kappa_\nu \rho ds \quad (3.3)$$

is defined as the optical depth. We call the medium optically thick if $\tau > 1$ and optically thin if $\tau < 1$.

If the medium is not only absorbing light but also emitting, such as a hot gas, an additional term describing emission is included,

$$\frac{dI_\nu}{ds} = j_\nu - \alpha_\nu I_\nu \quad (3.4)$$

where j_ν is the emission coefficient, or emissivity.

Kirchhoff's law tells us that in thermodynamic equilibrium (TE), the absorption and emission coefficient α_ν and j_ν are not independent. Instead, they are related by the Planck function $B_\nu(T)$:

$$j_\nu = \alpha_\nu B_\nu(T) \quad (\text{Kirchhoff's law}) \quad (3.5)$$

A formal solution to the differential equation Eq 3.4 is then

$$I_\nu(s) = I_\nu(s_0) e^{-\tau_\nu(s_0, s)} + \int_{s_0}^s B_\nu(T(s')) \alpha_\nu(s') e^{-\tau_\nu(s', s)} ds' \quad (3.6)$$

In wavelengths where the emission from the medium is small but scattering is significant, the effect of scattering should also be included to the differential equation with a loss term and a gain term:

$$\begin{aligned} \frac{dI_\nu}{ds} &= j_\nu^{\text{therm}} + j_\nu^{\text{scat}} - (\alpha_\nu^{\text{abs}} + \alpha_\nu^{\text{scat}}) I_\nu \\ \text{where } \alpha_\nu^{\text{abs}} &= \rho \kappa_\nu^{\text{abs}} \\ \alpha_\nu^{\text{scat}} &= \rho \kappa_\nu^{\text{scat}} \\ j_\nu^{\text{therm}} &= \alpha_\nu^{\text{abs}} B_\nu(T) \end{aligned} \quad (3.7)$$

where α_ν^{abs} and α_ν^{scat} are the absorption and scattering extinction coefficients, κ_ν^{abs} and κ_ν^{scat} are the absorption and scattering opacity. This is the **radiative transfer equation** that will be solved by RADMC-3D. In practice, the scattering source function j_ν^{scat} depends on how realistic one wants to model scattering, which we will see in RADMC-3D calculation.

RADMC-3D¹ is a software package for cell-based 3D astrophysical radiative transfer calculation developed by C. P. Dullemond et al. The main task of RADMC-3D is calculating what a image or spectral energy distribution (SED) look like given a dust and/or gas density distribution in 3-D space. Normally, it does so in two steps: First, a thermal Monte Carlo simulation is run with the command `mctherm` to calculate the dust temperature. Then, the image or SED is made by ray-tracing with command `image` or `sed`. If scattering is included, a scattering Monte Carlo is run to determine the scattering emissivity j_ν^{scat} before making the ray-tracing image.

For the thermal Monte Carlo run, the total luminosity of the light source is divided to `nphot` photon packages. After emitted by the source one-by-one, they travel through the density distribution, get absorbed by dust, be re-emitted in another direction and wavelength, or get scattered off dust grains and change directions. Each time a photon package enters a cell, it changes its energy and temperature. After all packages travelled through and escaped from the outer edge of the model, the temperature distribution at each cell is the final result.

The scattering Monte Carlo follows the same manner, but the number of scattering photon packages is controlled by a separate parameter, `nphot_scat`. The higher this number, the less streaky noise patterns would appear in the scattering image. In calculating the scattering emissivity j_ν^{scat} , RADMC-3D has five modes of treating the scattering source function with different levels of realism, from isotropic scattering to anisotropic scattering with full polarization. For a detailed description on how RADMC-3D treats scattering, see the official manual².

For SED calculation, the scattering photon package number is controlled by yet another parameter, `nphot_spec`, but it has the same meaning as `nphot_scat`. Producing SED with scattering is usually time-consuming since it involves creating a intensity image (including the scattering Monte Carlo run) and integrate over the image for each wavelength point. Because of the integrating operation, the SED is less sensitive to noise and `nphot_spec` can usually be taken to be 2-3 orders of magnitude smaller than `nphot_scat` to save computation time, while still producing accurate results. Even if the result SED still contains noisy data points, they can be smoothed out with some technique, see tips section below.

3.3 Running RADMC-3D

3.3.1 Model setup

For dust continuum radiative transfer calculation in RADMC-3D, many input files in required formats are needed to set up the computation model. The first is grid information, which is transformed from JUPITER descriptor file using the conversion

¹https://www.ita.uni-heidelberg.de/~dullemond/software/RADMC-3D/manual_radmc3d/index.html

²https://www.ita.uni-heidelberg.de/~dullemond/software/radmc-3d/manual_radmc3d/dustradtrans.html#five-modes-of-treating-scattering

pipeline DATtoRADMC mentioned in last chapter. RADMC-3D accepts three formats of grid styles: regular grid, Oct-tree-style AMR and layer-style AMR, and the JUPITER grid corresponds to the last type. Here the required order of coordinates is in r , θ , ϕ .

Two hydrodynamic fields are required for radiative transfer calculation: the dust density field and dust temperature field. The dust density field is generated from gas density with the DATtoRADMC pipeline, assuming a constant dust-to-gas ratio of 0.01, which is consistent with the hydrodynamic simulation setup. This serves as a good assumption as long as the dust particles are strongly coupled to the gas, which is the case if they are in size on the order of microns.

The dust temperature field can be generated in two ways: 1. By default, this file should be created by the thermal Monte Carlo step within RADMC-3D before making ray-tracing images. While testing this method it is found that dust temperature is not well modelled by the thermal Monte Carlo at the circumplanetary disk region, where we are particularly interest in. As mentioned before, the planet's vicinity are heated to high temperature due to accretion processes and the shock front from vertical influx on the CPD surface. These processes improves the observability of the CPD, thus should be taken into account in our modelling. However, the thermal Monte Carlo method in RADMC-3D does not include these heating processes, therefore result in a much lower temperature at the circumplanetary region. This could lead to a unrealistic mock observation of CPDs. To improve the modelling of dust temperature, another method is adopted: 2. We take the hydrodynamic simulation calculated gas temperature field and assume that $T_{\text{gas}} = T_{\text{dust}}$, i.e. dust and gas are in thermal equilibrium. Although this treatment is not perfect as well, it accounts for the key heating processes in the circumplanetary region and provides a much more realistic result. For a detailed discussion on these two methods and comparison images of dust temperature generated, see Szulágyi & Garufi (2021).

For dust transfer, opacity files are required as input. The dust species is taken to be 70% silicates, 30% carbon in 0.1 - 1000 micron grain sizes with -3.5 power law distribution. For a realistic treatment of scattering, we choose to use anisotropic scattering using tabulated phase function. For this we set `scattering_mode=3` in RADMC-3D, and this requires that we provide a table listing not only the wavelength-dependent absorption and scattering opacities, $\kappa_{\nu}^{\text{abs}}$ and $\kappa_{\nu}^{\text{scat}}$, but also the scattering matrix elements Z_{ij} for determining the scattering phase functions. These are calculated with Mie theory considering the BHMIE code from Bohren & Huffman (1984).

Other inputs includes a file that contain all information about the light source, i.e. the star. Here, we place the star at image center and use the solar mass and radius, as in the hydrodynamic simulation. We take advantage of RADMC-3D's functionality to treat the star as a finite sphere. For spectrum of the star we simply use a blackbody spectrum at 5780 K. The discrete wavelength points for the continuum radiative transfer calculations are listed in another file, which are from 1 μm to 10 cm in 500 points. If not specified otherwise, the SED will also be calculated in these wavelength points.

Finally, some other controlling options are specified in the `radmc3d.inp` file. The following setting is used in our calculation:

```
nphot_scat = 10000000
istar_sphere = 1
tgas_eq_tdust = 0
scattering_mode_max = 3
iseed = -27437
mc_scat_maxtauabs = 5.d0
```

RADMC-3D provides a python package `radmc3dPy` for reading and analyzing the input and output files of RADMC-3D. However, the python tool currently does not support layer-style AMR grids, thus I developed an own script `radmcutils.py` base on functions in the original package to manipulate and visualize input files layer-style grids. The script supports reading and writing input files, extending the density and temperature fields if needed (as described in Ch.2), and imposing dust evaporation if not already included.

3.3.2 Running from command line

With the input files ready, RADMC-3D can be easily run by calling the executable `radmc3d` followed by the desired commands in command line. In our case, the calculation needs to be run on multiple models repeatedly, so a bash script is made to handle the iterations. The pipeline for a single run for creating an intensity image reads:

```
radmc3d image npix ${n} sizeau ${a} incl ${i} lambda ${l} fluxcons
cp image.out npix${n}lam${l}inc${i}.out
python tofits.py npix${n}lam${l}inc${i}.out
rm npix${n}lam${l}inc${i}.out
```

where `n`, `a`, `i`, `l` are the variables to loop over. The command `fluxcons` ensures flux conservation during ray-tracing. `tofits.py` wraps the `writeFits` function in `radmc3dPy` package to save the output to fits format for further use. The output flux values are scaled to 1 pc distance by RADMC-3D default. While writing to fits, we re-scaled the fluxes to a distance of 100 pc.

3.3.3 Tips and tricks

Accelerating RADMC-3D runs

When making a large amount of scattering ray-tracing image or SED, it can take several hours to run, even days. Thus, it can be very helpful to use parallel cores for computing. The `setthreads` command in RADMC-3D supports Open-MP parallelized Monte Carlo to speed up the computation. To use this option simply add `setthreads n` in the end of the command to run RADMC-3D, where `n` is the desired number of core to use. However, this functionality only speeds up the Monte Carlo step, which means other steps such as reading/writing files and ray-tracing are still excuted in a single core. In the case of SED or cube image runs where `nphot` is relatively small, it is the ray-tracing step that take the most computation time. Thus,

the built-in `setthreads` parallel computing does not save much time in this case. If multiple SEDs or cube images are to be run, it is much more efficient to run each of them in parallel, than running them in series while using `setthreads`. An example bash script to do so is shown here, where I define a bash function first and then use the operator & to put the task in background:

```
sed_star(){
cd $1
radmc3d sed sizeau 250 fluxcons
cp spectrum.out sed_entire_sys.out
cd ..
}

for dir in 10jup50au 5jup50au 1jup50au 1sat50au
do
    sed_star ${dir} &
done
```

Dealing with scattering photon noise

For circumstellar disks with massive embedded planet, e.g. in the $10 M_{\text{jup}}$ and $5 M_{\text{jup}}$ case, the high temperature shock front above the CPD region causes spurious individual photon trajectories to show up, making the image at CPD region look noisy, as shown in Fig 3.2 left. To get rid of these noisy photon streaks, we perform repeated RADMC-3D runs for each $10 M_{\text{jup}}$ and $5 M_{\text{jup}}$ cases with varied seed numbers and average them up. Since these noise streaks are orders of magnitude brighter than its back ground, taking the mean can't remove them efficiently. To reduce the number of repeated runs, I take the median instead of mean of the seed-varied images, and test indicates that 5 runs per image are already enough to remove the bright photon noises. The bash command to change seed number is:

```
sed 's/oldseed/newseed/g' radmc3d.inp > idf; mv idf radmc3d.inp
```

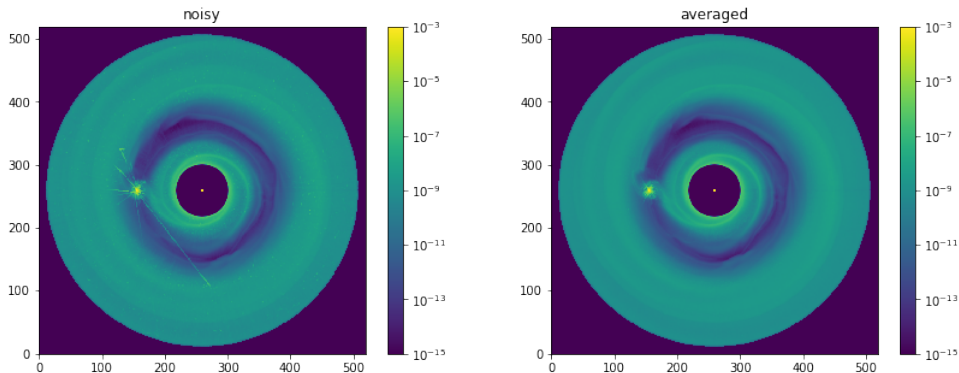


Figure 3.2: *left*: noisy streaks show up in CPD region. *right*: averaged image.

Still, this significantly increases the time for calculating each image, thus setting

parallel threads as mentioned above become crucial in this case.

Dealing with noisy spectrum

A "small" `nphot_spec` can lead to spectrum with noisy spikes. They can be smoothed out with some techniques while plotting. What I did is: 1. Remove a data point n and replace it with the average of data points $n-1$ and $n+1$ if data point n is larger than 1.5 times of point $n-1$ or $n+1$. 2. Apply an 1D Gaussian filter to smooth out the curve. After the two steps, the noise spikes are removed, like shown in Fig 3.3 right.

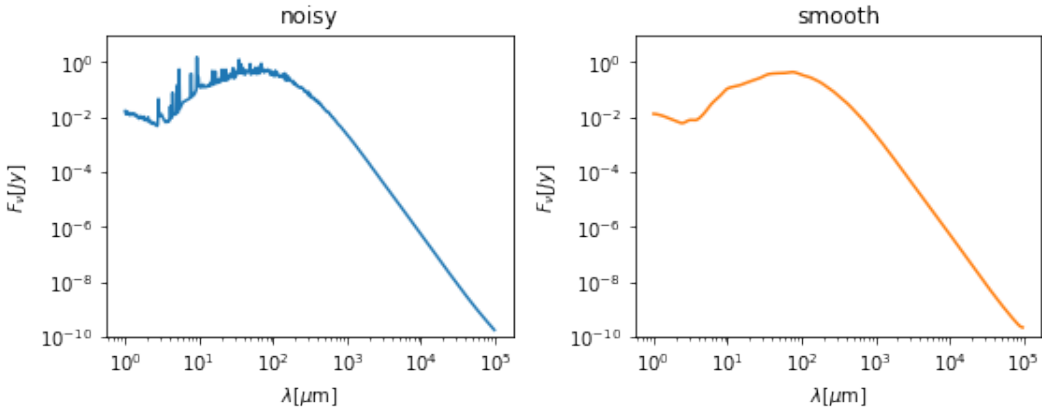


Figure 3.3: Photon noise on a spectrum and noise removed.

Chapter 4

Simulating Telescope Images

4.1 Overview of near future telescope and instruments

4.1.1 James Webb Space Telescope

The James Webb Space Telescope (JWST), scheduled to be launched in November 2021, is planned to become the successor of the Hubble Space Telescope as NASA’s largest space observatory. It is planned to be deployed at the Sun-Earth L2 Lagrange point and orbit the Sun together with Earth. With its 6.5m primary mirror composed of 18 hexagonal segments, it will provide imaging capability from long visible light to near-mid infrared wavelengths.

Of the four instruments aboard JWST, three of them are imagers which are investigated in this work. The Near Infrared Camera (NIRCam) features imaging in a short wavelength channel ($0.6\text{-}2.3\ \mu\text{m}$) and a long wavelength channel ($2.4\text{-}5.0\ \mu\text{m}$) with high sensitivity. The Mid-Infrared Instrument (MIRI) covers from $5\text{-}28\ \mu\text{m}$, and both instrument comes with a coronagraphy mode to suppress starlight for high-contrast imaging of planets. NIRISS (Near Infrared Imager and Slitless Spectrograph) features high-contrast interferometric imaging and imaging between 0.6 and $5.0\ \mu\text{m}$. JWST will be able to image planet forming disks in a wavelength range never explored before. The $0.06''$ pixel size of NIRCam/NIRISS and $0.11''$ for MIRI will be able to resolve the $0.3''\text{-}0.5''$ angular separation for planets at 30-50 AU from its star.

The specific properties of these three JWST instruments are listed in Table 4.1.

Public software tools have been developed by the Space Telescope Science Institute (STScI) and other teams to simulate data produced by the JWST instruments. These include `WebbPSF` for point spread function (PSF) simulations for all JWST instruments, `Mirage` for NIRCAM and NIRISS simulation, and `MIRISim` for MIRI, etc. The usage of the later two packages in this work are described in the following sections in detail.

4.1.2 ELT

The ELT, short for Extremely Large Telescope, is currently under construction in Cerro Armazones, Chile by ESO and expects to see its first light in late 2020s. With its 39 m diameter, it will become the world's largest optical/infrared telescope. It will be able to push astronomical discoveries with the unprecedented spatial and spectral resolution it delivers.

For the imaging of forming planets around other stars, two of the several instruments under design will be used, the Multi-Adaptive Optics Imaging Camera for Deep Observations (MICADO) and the Mid-infrared ELT Imager and Spectrograph (METIS). They will provide high-contrast imaging capability in near and mid infrared respectively with the aid of the adaptive optics system on ELT. The zoomed field-of-view mode of MICADO with a pixel scale of 1.5 mas/pixel will provide the sharpest resolution among all current and planned instruments. Other important instrument specifications are listed in Table 4.1.

The simulators for MICADO and METIS are actively being developed. For the imaging mode of MICADO, the current version of `SimCADO` package already provides the essential functionalities to cover the science case of this work. `SimMETIS`, a package adapted from `SimCADO`, supports the simulation of METIS L/M and N band imaging. The usage of the two simulators will be covered in section 4.2.

4.1.3 Giant Magellanic Telescope

The Giant Magellanic Telescope, GMT in short, is the next-generation extremely large ground telescope from the U.S. side, located in Las Campanas, Chile. Its seven 8.4 m diameter primary segments together form an effective primary aperture of around 25 m and give a total collecting area of 368 square meters. The currently planned first-light instruments includes four spectrographs. Among them, the Integral-Field Spectrograph (GMTIFS) incorporates an imaging channel with adaptive optics system which allows high-contrast imaging in the JHK band, and this is the only instrument of interest on GMT in this work.

For simulating the performance of GMTIFS, a simulator tool has been developed by Australian National University, the leading institute of the instrument, but it is not yet publicly available online (see Sharp et al. [2016]¹). Reference data files such as the instrument PSFs and detector dark currents are also not published online. For this reason, the simulated observation by GMTIFS in this work will be done by convolving the RADMC3D images with self-simulated GMT PSFs followed by noise addition. The detailed steps will be covered in section 4.2.

Table 4.1 lists the important specifications of the instruments from the three telescopes used in this work. The image sizes in pixels for 50 & 30 AU case are calculated by $n_{pix} = \frac{\text{image_angular_size}}{\text{instrument_pixel_scale}}$ and are also listed in the last column. To match the pixel scale for each instrument, RADMC3D images with different pixel sizes are custom-made for each instrument.

¹http://www.astro.iag.usp.br/~eaa2018/Talks/SaoPauloLecture2_180228.pdf

	Instrument	Wavelength coverage (μm)	Field-of-view	Pixel scale ("/pixel)	Image npix 50 AU	Image npix 30 AU
JWST (6.5m)	NIRCam	0.6 - 2.3	$2 \times 132'' \times 132''$ (44" and 5" gaps)	0.031	84	48
		2.4 - 5.0	$2 \times 129'' \times 129''$ (48" gap)	0.063	41	23
	NIRISS	0.8 - 5.0	$133'' \times 133''$	0.065	40	23
	MIRI	5 - 28	$74'' \times 113''$	0.11	23	13
ELT (39m)	MICADO	0.8 - 2.45	$50.5'' \times 50.5''$	0.004	not used	not used
			$18'' \times 18''$	0.0015	1733	1000
	METIS	3 - 5	$10.5'' \times 10.5''$	0.005	520	300
		7.5 - 13	$13.5'' \times 13.5''$	0.007	371	214
GMT (25m)	GMTIFS	0.9 - 2.5	$20.4'' \times 20.4''$	0.005	520	300

Table 4.1: Instrument specifications. Figures are taken from: JWST: <https://jwst-docs.stsci.edu/>; ELT: <https://elt.eso.org/>; GMT: <https://www.gmto.org/resources/near-ir-ifu-and-adaptive-optics-imager-gmtifs/>

Based on the wavelength coverage of the above instruments and the spectral energy distribution young planet systems, several bands are chosen to be studied in this work. The photometric bands of interest and corresponding instrument filters are summarized in Table 4.2.

4.2 Telescope simulators in detail

4.2.1 Mirage

Mirage, short for Multi-Instrument Ramp Generator, is a python package that creates simulated data for a variety of NIRCam and NIRISS observing modes. In real observations, the high-contrast imaging of circumstellar disks requires coronagraphy mode, however, the **Mirage** package does not support coronagraphy simulation currently. In this work, the short- and long-wavelength imaging mode for NIRCam, and imaging mode for NIRISS will be used.

The working principle of **Mirage** is illustrated first. The workflow of **Mirage** can be summarized into three stages, which are shown in the figure below.

Bands	NIRCam	NIRISS	MIRI	MICADO	METIS	GMTIFS
J	F115W 1.15 ± 0.11	F115W 1.15 ± 0.12	/	J 1.25 ± 0.1	/	hJ 1.23 ± 0.12
H	F150W 1.50 ± 0.16	F150W 1.50 ± 0.17	/	H 1.64 ± 0.15	/	hH 1.64 ± 0.16
K	F200W 1.98 ± 0.23	F200W 1.98 ± 0.23	/	K_s 2.14 ± 0.17	/	hK 2.27 ± 0.23
L	F356W 3.59 ± 0.46	F356W $3.59 \text{ \AA} \pm 0.46$	/	/	L 3.79 ± 0.31	/
M	F444W 4.43 ± 0.56	F444W 4.43 ± 0.56	/	/	M_p 4.88 ± 0.31	/
N	/	/	F1000W 10.0 ± 1.0	/	N_2 11.8 ± 1.1	/
Q	/	/	F1500W 15.0 ± 1.5 F2100W 21.0 ± 2.5	/	/	/

Table 4.2: Photometric bands of interest and relevant instrument filter names. The central wavelength and width (in μm) are also presented. The filter specifications are taken from same sources as table 4.1.

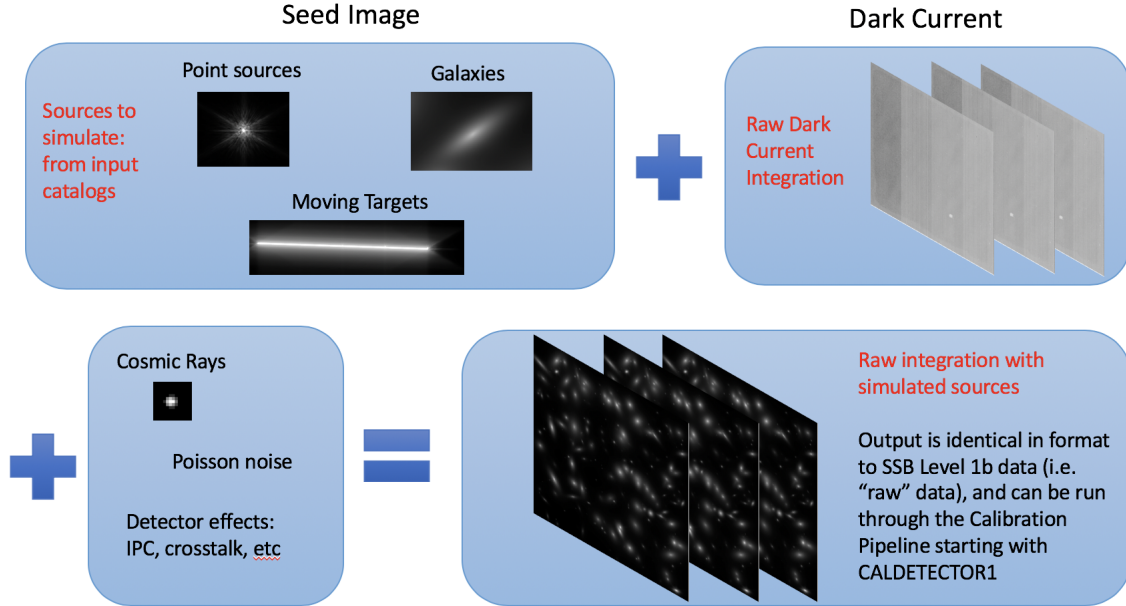


Figure 4.1: Flowchart showing the three stages of **Mirage** simulator. Taken from https://mirage-data-simulator.readthedocs.io/en/latest/three_steps.html

In the first stage, a noiseless count rate image is created from the input source, called the "seed image". The input source, specified by a source catalog file, is

read in, cropped and placed at the specified position of the detector plane, and convolved with the instrument PSF. The seed image contains only signals from the astronomical scene as seen through the instrument. In the second stage, dark current preparation, dark current ramp files from the reference files library are manipulated to match the number of frames, integrations, and readout pattern requested by the user. Then, this dark current exposure can be linearized and cropped to the detector subarray size, so that they are ready to be added. In the final stage, the simulated observation is generated. The seed image is translated from a count rate image into a series of integrations (frames) according to the specified readout patterns. These frames are combined to form a seed exposure. The total exposure time is thus determined by N_{int} , N_{frame} , and readout pattern. Other effects such as cosmic rays and Poisson noise are added to the seed exposure. Finally, the seed exposure and dark current exposure are added frame by frame to form the final observation exposure, which is saved as a fits file with identical format of real JWST output data. The three stages are performed by the `catalog_seed_image.py`, `dark_prep.py` and `obs_generator.py` modules respectively, which are all wrapped in the class function `ImgSim.create()` in the module `imaging_simulator.py`.

Next, I briefly summarize the steps to run `Mirage` for this work. All codes mentioned below can be found in the author's GitHub repository². The `Mirage` package can be installed following the instruction of the official document³. This creates a conda environment `mirage` inside which all following steps will be run. Besides the installation of the package itself, the set of reference files needs to be separately downloaded using the downloader script in the package. These includes the libraries of dark current ramps, cosmic rays and PSFs, which in total takes tens of GB of disk space. Before using the package, the environment variables which specifies the path to `Mirage` data and Calibration References Data System (CRDS) must be set. These are included in the first few lines of the python script I made to wrap the usage of `Mirage` simulator, `nircam_sim.py`.

To run a simulation, all user-input parameters are provided through a `yaml` parameter file. This file can be generated using functions in the `yaml_generator.py` module. The first part of the `yaml` file contains observation settings such as instrument filter to use and the pointing of telescope. These information are best provided by the Astronomer's Proposal Tool (APT)⁴. In the APT GUI, target information and observation settings including filters, readout patterns, number of groups and integrations can be chosen. The setting is then exported to a `.xml` file and a `.pointing` file, which are to be input to the `yaml` generator. The second part of the `yaml` file contains all information of the astronomical source. Generally, sources are listed in a source catalog file(`source_catalog_file.cat`) from which the `yaml` generator will read from. In the case of this work, the source is a fits image of a extended object and the path to the fits file is listed in the source catalog file. A few other parameters such as cosmic ray and background noise level are set through

²<https://github.com/alphalyncis/msthesis>

³<https://mirage-data-simulator.readthedocs.io/en/latest/>

⁴<https://www.stsci.edu/scientific-community/software/astronomers-proposal-too>

python. All the info above are fed into the yaml generator, and a `Mirage` run can be called with the generated yaml file. For the first time running a simulation for a specific detector module, a series of CRDS files will be downloaded from the server, which may take some time or cause error if data server is temporarily unavailable.

In order to repeat the above procedure for every wavelength, disk model and inclination, and changing simulation parameters when necessary, a pipeline is developed as follows:

1. Pairs of `.xml` and `.pointing` files are created using APT tool for each filter-detect combination of interest, and placed in separate sim data directories.
2. A bash script is written to loop over every disk model and inclination, each having a fits image to be input to the sim wrapper `nircam_sim.py`.
3. In each iteration, the input fits image is first convert to unit of ADU/s by the self-written routine `fits_to_adu.py` (See description in Tips section). The result fits image is saved to a sim data directory.
4. Next, run `nircam_sim.py` on the ADU image to generate the final exposure image. This wrapper script takes the input filename from command line and reads the wavelength info from it. Then, it updates `source_catalog_file.cat` with this filename and sets the other parameters accordingly (See table 4.3). Then, `yaml` file is generated, simulation is run and output image is cropped and saved to corresponding directories.

The pipeline for NIRISS follows exact same steps, except that the `.xml` and `.pointing` files are created with different instrument-filter selection in APT tool, and the input images are in sizes that matches NIRISS pixel scale. A separate python wrapper, `niriss_sim.py`, is made for NIRISS.

To mimic the effect of coronagraphy despite the lack of coronagraphy simulation mode in the existing package, the brightness of the central stellar pixel is masked to 1% of original value before inputting into the simulators. This method will also be adopted to every instrument in the following sections.

The filters-detector combination and other key simulation parameters used are summarized in Table 4.3.

Tips for using `Mirage`

1. `Mirage` requires that the input fits image have the unit of ADU/s, whereas the fits image output from RADMC3D has the unit of Jy. Thus a unit conversion must be done before running the simulator. In principle, the conversion factor Jy2ADU for a filter with pivot wavelength λ and width $\Delta\lambda$ is calculated as follows:

$$F_\lambda[\text{ADU/s}] = F_\lambda[\text{Jy}] \cdot \underbrace{\frac{1[\text{J} \text{ m}^{-2}\text{s}^{-1}\mu\text{m}]}{1[\text{Jy}]}}_{\text{Jy2ADU}} \cdot \pi \left(\frac{D}{2}\right)^2 [\text{m}^2] \cdot \Delta\lambda[\mu\text{m}] \cdot QE \cdot \frac{1}{G} \quad (4.1)$$

Instrument	NIRCam		NIRISS			
Filter	F115/150/200W	F356/444W	F115/150/200W	F356/444W		
Detector module	A1		A5			
Readout pattern	SHALLOW4		NIS			
$N_{\text{integration}}$	1		1			
N_{group}	10		10			
Exposure time total	526.1 s		429.5 s			
Cosmic ray level	SUNMAX					
Background level	medium					

Table 4.3: Key simulation parameters for NIRCam and NIRISS

where D is the diameter of primary mirror, QE is the quantum efficiency of the instrument and G is sensor gain. In `Mirage` package, a zeropoint table which contains the flux to count rate conversion factor (`photfnu`, in $\text{erg s}^{-1} \text{cm}^{-2} \text{Hz}^{-1}$) for each filter-detector combination is already given (`NIRCam_zeropoints.list` and `NIRISS_zeropoints.list`), so I directly take the corresponding values in these tables to calculate conversion factor as $\text{Jy2ADU} = 10^{-23} \times \text{photfnu}$.

2. Different filters may require different detector module. NIRCam short channel imaging can be only performed by module A1-A4/B1-B4 and long channel imaging can only be performed by module A5 and B5. The different detector module for NIRCam locate on different positions on the NIRCam focal plane, so the pointing information in `source_catalog_file.cat` has to be adjusted accordingly to make seed image fall inside the detector region. The coordinate of seed image center can be checked with a few lines of code inside the `mirage.seed_image.catalog_seed_image` module, which are adapted to a function `get_center_pos()` in the python wrapper script. Before cropping the final detector image, the center for cropping is determined using this function.

3. It is a known limitation of `Mirage` that the PSFs from the current library are several hundred pixels on a side and the wings are cut off, so the truncated PSF edges will be visible in the image if the sources are bright. The brightness normalization of PSFs also causes the brightness that should be in the wing to be in the truncated PSF instead, which makes the brightness of source more concentrated in the PSF center than it should be. This effect will be seen in the images from `Mirage` in result section.

4.2.2 MIRISim

MIRISim is a python package developed by the MIRI European Consortium for simulating realistic instrumental effects through MIRI. A detailed description of how MIRI works can be found in the official documentation⁵. The workflow between

⁵<https://wiki.miricle.org/pub/Public/MIRISimPublicRelease2dot4/MIRISim.pdf>

the components of MIRISim is shown in Fig 4.2

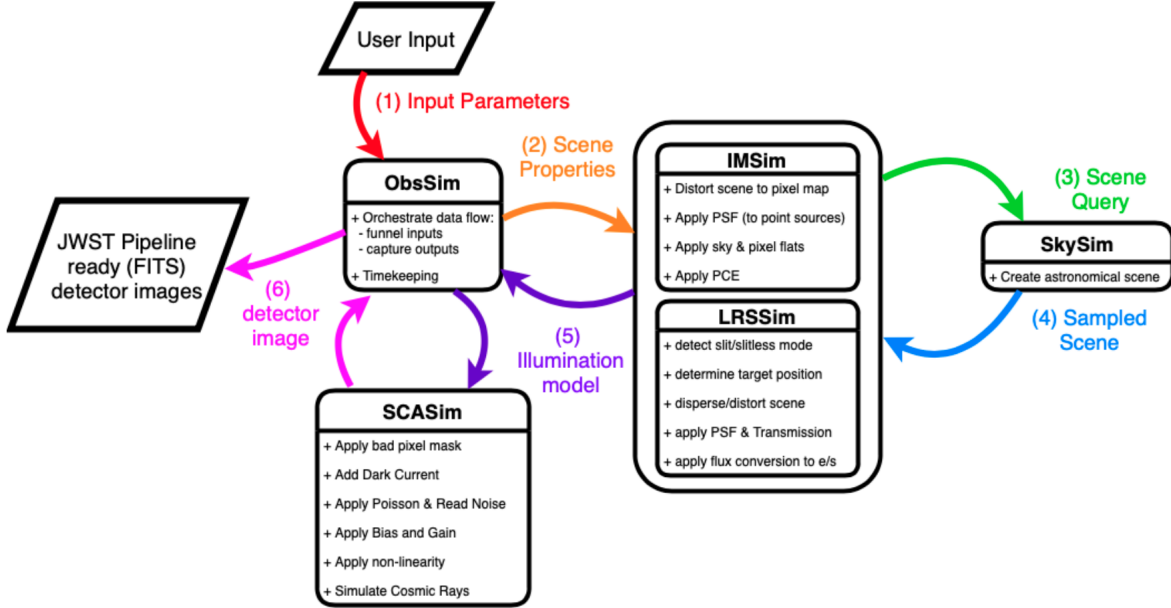


Figure 4.2: Flowchart showing the three stages of Mirage simulator. Taken from MIRISim documentation <https://wiki.miricle.org/pub/Public/MIRISimPublicRelease2dot4/MIRISim.pdf>

To simulate a MIRI detector image, four of these components are involved: 1. **SkySim** creates a sky scene composed of multiple sources to be observed by reading in a user supplied fits file or generating from pre-defined target types. Here the fits file needs to be a 3D image cube with an extra spectral dimension, since MIRISim needs to know the wavelength binning of the data to conserve flux correctly over the filter band. The output of **SkySim** is passed to other components as a **SceneConfig** class object and also can be saved as a scene config file, **scene.ini**. 2. **ObsSim** collects observation parameters requested by the user such as the MIRI filter, readout pattern and detector array to be used, the number of integration and exposure, and the telescope pointing. The setting for **ObsSim** is passed as a **SimConfig** class object and saved to a simulation config file **simulation.ini**. 3. The scene and simulation config are fed to **ImSim** where an illumination model is created by adding effect through the optics such as transmission, distortion, dispersion and PSF. The illumination model is output as a fits file in unit of electron/s, which will tell a specified detector how it should be illuminated provided the input source. Finally, **SCASim** (SCA short for Sensor Chip Assembly) adds all the detector effects (including Poisson noise, read noise, cosmic rays, dark current, quantum efficiency, sensor gain, detector non-linearity, etc.) set by user and builds up ramps with specified number of groups, integration and exposure to create the final detector image.

The pipeline for MIRI simulation is as follows:

1. Image cubes with 5 wavelength bins are made by RADMC3D. This step can be a bit time-consuming. When writing the RADMC3D output to fits file, the flux unit is converted from $\text{erg s}^{-1} \text{ cm}^{-2} \text{ Hz}^{-1} \text{ sr}^{-1}$ to Jy/arcsec^2 , and the fits header also needs to be edited to make it recognizable by MIRISim.
2. A wrapper script `miri_sim.py` takes a command line input filename, reads the wavelength to be simulated from it and configure the scene and observation. The `SimConfig` is created from default. With these three config inputs, MIRISim is run.
3. The output detector image is a 4D cube with (integrations, frames, x, y), which effectively contains hundreds of layers of 2D images. To save disk space, the image cube is cropped with respect to subarray center and only the last frame in each integration is saved. The layers of integrations will be averaged in later step to plot a single detector image.

Simulation parameters for MIRI is summarized in Table 4.4.

Background	level = 'low', gradient = 5, pa = 45
Filters	F1000W, F1500W, F2000W
Detector subarray	SUB256
Readout mode	FAST
N_{integration}	20
N_{frame}	50
Exposure time total	299.52 s

Table 4.4: Key simulation parameters for MIRI

Tips for using MIRISim

1. Avoid heavy downsampling: If the input fits file has too many pixels, e.g. has a much higher resolution than MIRI's pixel scale, the simulation can become very slow, since it has to downsample spectral columns of $x \times y$ pixels. This can be avoided by inputting fits images with pixel scales similar to that of MIRI.
2. Problem of saturation: If the source is too bright, it can saturate the detector pixels in a relatively small number of frames/integrations. According to STScI document⁶, one can avoid saturation by using a detector subarray instead of the full array, e.g. using SUB256 instead of FULL. The effect of adopting a subarray is shown in Fig 4.3.

⁶<https://jwst-docs.stsci.edu/mid-infrared-instrument/miri-observing-strategies/miri-cross-mode-recommended-strategies#MIRICross-ModeRecommendedStrategies-SaturationHowshouldIdealwithsaturation?>

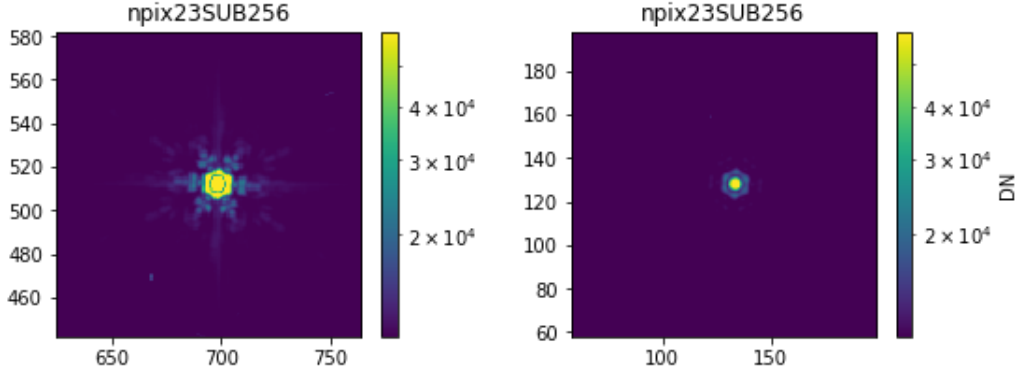


Figure 4.3: MIRI simulation for the same point source using FULL detector array(left), and SUB256 detector subarray(right). There are 13 saturated pixels in the left image.

4.2.3 SimCADO and SimMETIS

The `SimCADO` python package is developed by the MICADO consortium for simulating the effects of MICADO optical elements and detectors on the incoming photons. Since `SimMETIS` is a branch of `SimCADO` and the inner workings are exactly the same, I will only introduce the former and point out the difference when necessary.

The work flow of `SimCADO` is illustrated in Fig 4.4.

The key object in the simulation is `Source`. It can be created from source types in the library, or in this case, given by user input. Instead of requiring a 3D cube with a spectral dimension, `SimCADO` saves disk space by requiring only a 2D spatial image and a spectrum associated with the image. The `OpticalTrain` object contains information of the complete optical path a photon travels before converted to an electron, from the atmosphere, telescope to the instrument. When running a simulation, `Source.apply_optical_train()` is called, which applies the effects designated by the `OpticalTrain` on the image. The `Detector` object contain `Chips` that reads out the signal and adds detector noise onto the image. Only one image at the end of the entire exposure time is read out. Due to the lack of real noise data from testing like JWST, the workflow of `SimCADO` is simpler than the JWST simulators. The package is also much lighter and easier to use. The user configurations are all passed by the `UserCommand` object. It can be either specified through a `.config` file, or set in python scripts. Those simulation parameters not set by the user will come from the default config file.

The python routine developed for using `SimCADO` follows similar steps as before. A few important simulation parameters are defined in the beginning of the wrapper script `micado_sim.py` or read from the input fits file name, and the rest configurations simply adopt the default values. Then, input fits image and spectrum are read and converted to create the source. Finally, simulation is run and the result is cropped and saved. Some points for caution are included in the tips section.

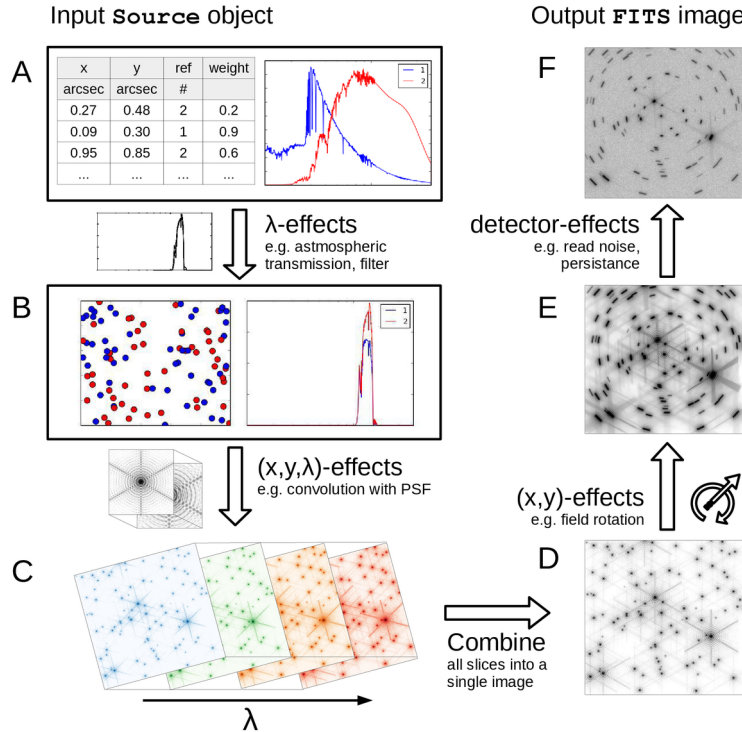


Figure 4.4: The steps an input Source object goes through in an optical train. Taken from [Leschinski et al. \(2016\)](#).

Tips for using SimCADO

1. After importing the fits image and spectrum and before creating a `Source` object using the `source_from_image()` method, the flux unit of the spectrum needs to be converted to photon/(m² s bin) to be read in. This is done by computing the conversion factor f_λ , the number of ph/(m² s um) that correspond to 1 Jy at λ_{ref} , and the converted flux is $\text{flux} [\text{ph}/(\text{m}^2 \text{ s bin})] = \text{spec} [\text{Jy}] \times f_\lambda [\text{ph}/(\text{m}^2 \text{ s } \mu\text{m})/\text{Jy}] \times \text{d}\lambda [\mu\text{m}/\text{bin}]$, where `spec` is the original spectrum value in Jy.
2. The spectrum provided should cover at least the full bandwidth of the filter being used. An incomplete spectrum will cause flux conservation to fail.
3. When using `source_from_image()` method, the `oversample` parameter needs to be set if the input image scale does not exactly match the pixel scale of MICADO, which is usually the case. This helps `SimCADO` create at least 1 light source per pixel to avoid extended objects becoming a grid of point sources.

The routine for `SimMETIS` is similar, except that the user commands are read from two example config files for L/M and N band imaging which are already provided in `SimMETIS` package data. Only a few filter-specific parameters such as filter name and pixel scale are overwritten in the script.

The key parameters used in `SimCADO` and `SimMETIS` simulations are summarized in Table 4.5.

	MICADO	METIS
Imager mode	zoom	small_FOV = True
Detector layout	centre	/
OBS_NDIT	1	1
OBS_DIT	3600 s	7200 s

Table 4.5: Key simulation parameters for MICADO and METIS

4.2.4 GMT simulation routine

Due to lack of public simulation tools, the simulation of GMT mock images are done by a self written python routine. This includes generating a mock PSF for the GMT aperture, convolving the image with the PSF and adding noise. These steps are described in details in this section.

Creating the GMT primary aperture. Since the PSF is the Fourier transform of the aperture function, the geometry of GMT’s segmented aperture should first be modelled. The GMT PSF is effectively a product of the PSF of a 8 m diameter pupil with the interference patterns of the seven mirror segments [Conan et al. (2012)]. The python package `poppy` (Physical Optics Propagation in PYthon) developed by STScI provides functions that support constructing aperture models with different geometries and calculating PSF from them. The GMT aperture can be constructed by 7 circular pupils with a central obscuration. This can be modeled by the `MultiCircularAperture` optical element class⁷. The constructed GMT pupil image is shown in Fig 4.5, together with designed dimensions.

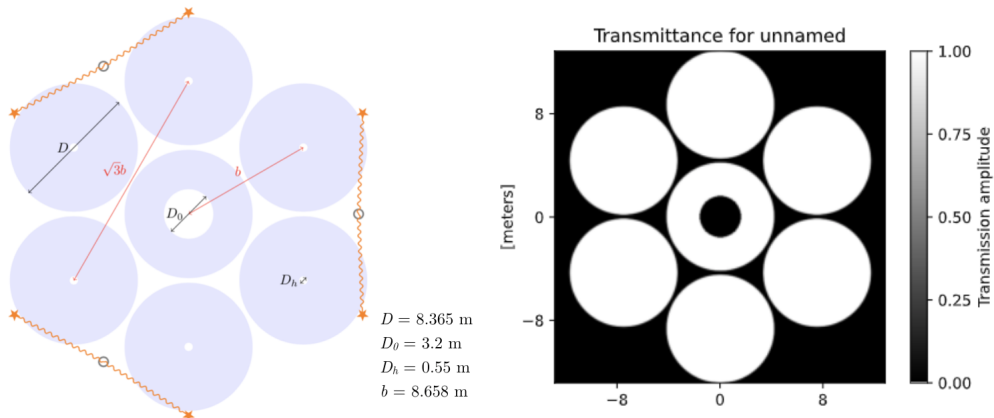


Figure 4.5: *left:* The GMT pupil parameters, image and values taken from [Conan et al. (2012)]. *right:* Pupil image constructed by `poppy`.

Calculating GMT PSF. An `OpticalSystem` instance is created from the mod-

⁷The `MultiCircularAperture` class is only in the newest development version of `poppy`. To use this class, `poppy` needs to be installed via cloning the Git repository from <https://github.com/spacetelescope/poppy> and installing inside the directory, instead of just `$ pip install poppy`.

elated pupil and PSF is calculated easily by its `.calc_psf()` method. An example output PSF is shown below:

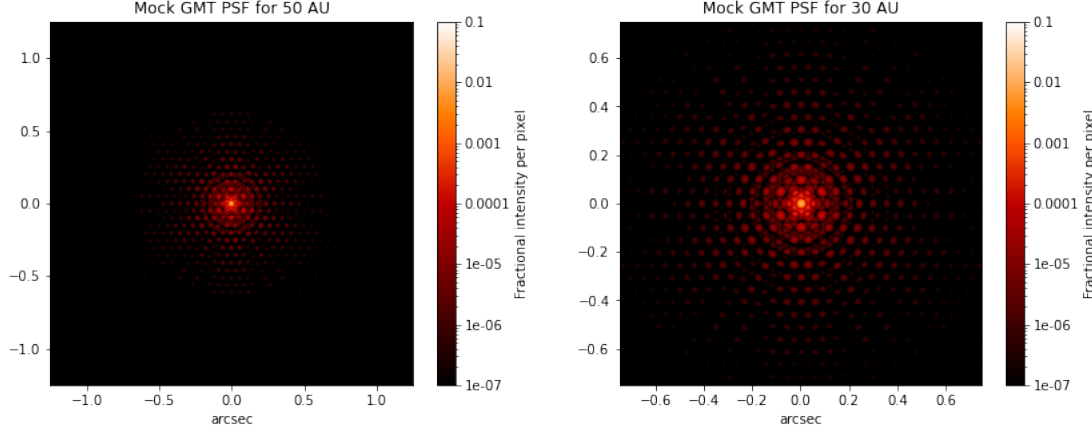


Figure 4.6: Mock GMT PSF with 2.5 and 1.5 arcsec FOV, which corresponds to the image angular size of 50 AU and 30 AU systems.

Convolving PSF with image. The image imported from fits file is converted to ADU/s using the same method as described for `Mirage` (Eq 4.1), multiplied by exposure time, and then convolving with the PSF. Coronagraphy is also treated by masking the central stellar pixel to 1% before convolution. Here the convolution is done by `scipy.signal.fftconvolve()`. The convolved image is shown in figure below.

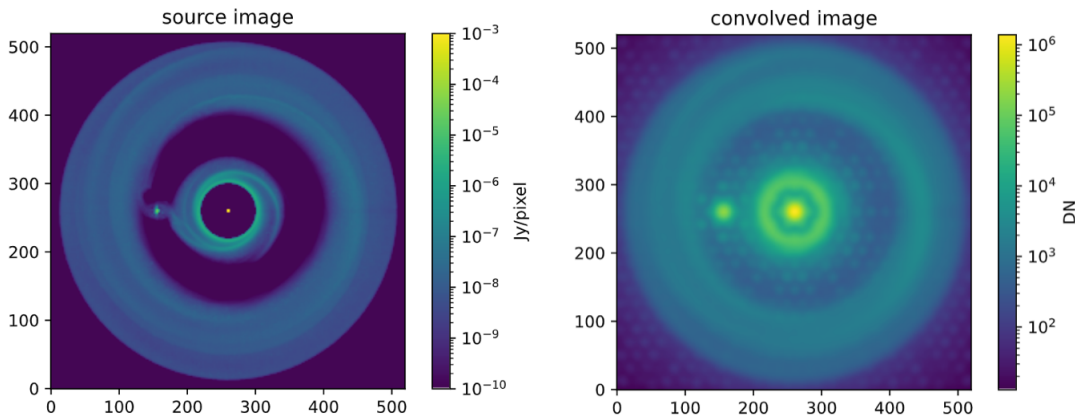


Figure 4.7: *left:* The input RADMC3D image. *right:* Convolved image.

Simulate atmospheric seeing. A Gaussian filter is further applied on the PSF-convolved image to mimic the blurring effect of atmospheric seeing on the image. Although this can be corrected by the AO system of the telescope to some extent, the residuals still pose a limitation from obtaining diffraction-limited images. Therefore, a Gaussian FWHM larger than the diffraction-limited PSF FWHM is used in this step.

Adding noise. Finally, two kinds of noise are added to the image. The first one is photon shot noise, which originates from the random event of photon detection. The process follows Poisson distribution, with the λ parameter corresponding to the mean number of photon detection event, which is estimated from our photon count image. With N photons detected, the noise (standard deviation) is \sqrt{N} . This is modelled by `noise_phot = np.random.poisson(lam=conv_image)`. The second noise type is random white noise, which does not depend on the brightness distribution of the source. Noise originated from the sky background and from the detector electronics can all be sorted into this type. Since the source of these noise are intricate and information about the instrument noise levels are not enough to model them separately, I simply use a empirical noise level that gives a SNR=5. (i.e. setting `noise_det = np.random.poisson(lam=np.ones((x,y))*conv_image.max()/5)`)

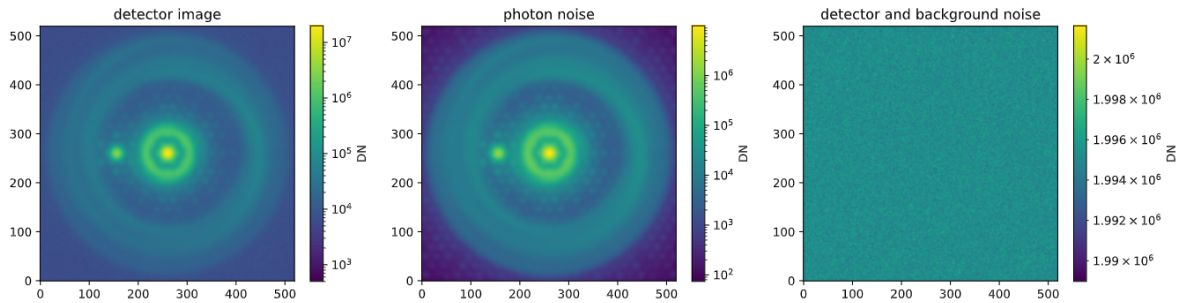


Figure 4.8: Noise-included final image and the two noise layer added.

Finally, a pipeline like the ones mentioned before is made for looping over each model and the final detector images are saved.

Chapter 5

Results

5.1 Synthetic images

Synthetic images are made in three inclinations, face-on (0°), 30° and 60° , for each instrument. The output images are in unit of Data Numbers (DN), i.e. the number of accumulated electrons in each pixel of the CCD detectors. Background noise is subtracted from the images by `img_sub = img - np.ones((x,y))*img.min()` and log scale is applied to allow better visualization of the imaged structures of disks. The central star is masked with a circular obscuration, except for cases where the PSF cores of the planet extend across the stellar position. For MIRI and METIS, the simulated images come in large variation in flux level for different filters or planetary masses, so the colorbars are scaled to each image by taking the median of that image as the lower limit. The result for each instrument is shown in tables in section 5.3, where each row shows the different planet mass cases and each column shows the filters investigated for that instrument.

5.2 Predicted magnitudes

Besides the simulated images, the flux in Jansky and in magnitude of the detected young planet are obtained through aperture photometry on these images and reported in tables.

The flux of each image is first converted from DN to physical units according to the specification of each instrument: For NIRCam and NIRISS, the same zeropoints table used in converting fluxes to ADU are used to convert the value back to Jy. For other instruments, due to the lack of existing zeropoints table, the conversion is done with dividing by the factor Jy2ADU as described in the `Mirage` section (Eq. 4.1), where $\Delta\lambda$ is taken as filter width, D is diameter of telescope effective primary mirror, QE and gain are read from simulated image header. The values used are listed in Table 5.1.

To obtain the planet brightness, an aperture is defined on the CPD with diameter equal to 2-3 times the FWHM of the instrument PSF, this way encircling 50% - 70% of the PSF energy but not touching the PSF core of the central star. The PSF

FWHM used for each instrument is also shown in Table 5.1.

Table 5.1: Instrument specifications used in flux conversion and instrument PSF sizes used in estimating aperture sizes.

instrument		phofnu (erg s ⁻¹ cm ⁻² Hz ⁻¹)	PSF FWHM		
			(pixels)		
NIRCam	F115W	6.819e-31	1.298 ¹		
	F150W	5.470e-31	1.628		
	F200W	4.610e-31	2.14		
	F356W	4.087e-31	1.830		
	F444W	4.110e-31	2.302		
NIRISS	F115W	2.773e-31	0.627 ²		
	F150W	3.124e-31	0.770		
	F200W	2.880e-31	0.991		
	F356W	2.670e-31	1.699		
	F444W	2.949e-31	2.089		
	$\Delta\lambda$ (μm)	QE	gain	D(m)	
MIRI	F1000W	2.0			2.888 ³
	F1500W	3.0	1.0	5.5	4.354
	F2100W	5.0			5.989
MICADO	J	0.195	0.88		4.00 ⁴
	H	0.29	0.90	1.0	5.33
	Ks	0.35	0.85		7.33
METIS	L	0.6	0.86		3.81 ⁵
	Mp	0.5	0.71	1.0	4.76
	N2	2.95	0.80		8.84
GMTIFS	hJ	0.25			2.4 ⁶
	hH	0.33	0.9	2	25.4
	hK	0.47			3.2
					4.2

¹<https://jwst-docs.stsci.edu/near-infrared-camera/nircam-predicted-performance/nircam-point-spread-functions>

²<https://jwst-docs.stsci.edu/near-infrared-imager-and-slitless-spectrograph/niriss-predicted-performance/niriss-point-spread-functions>

³<https://jwst-docs.stsci.edu/mid-infrared-instrument/miri-predicted-performance/miri-point-spread-functions>

⁴Davies & Genzel (2010)

⁵Brandl et al. (2021)

⁶McGregor et al. (2012)

Two fluxes are reported for each image: The first is the total flux of CPD, denoted as **CPD** in tables columns, which is calculated by summing the total flux over the aperture on CPD, and subtracted by the sum of an aperture of same size

on the background. Background subtraction is needed since the images obtained from the simulators are uncalibrated, which means the background level can be several times higher than the actual astronomical signal, so including them would give unrealistic object magnitudes. For the second CPD flux value, a same sized aperture is defined at the same separation but 180° away from the planet, from which obtain the anti-CPD flux. The CPD flux is subtracted by the anti-CPD flux to remove the circumstellar disk contribution in the background, as well as any stellar PSF extended to the distance of CPD, so that the flux left is only contributed by the CPD. These values are given under column name **CPD only** in the later tables. The Signal-to-Noise ratio (SNR) of the CPD detections are given by the ratio between CPD flux (without subtracting anti-CPD) and anti-CPD flux. Negative CPD-only fluxes and SNR values smaller than one are removed from the table since they indicate that there is no detection. The way SNR is calculated in our method is different from the usual definition of SNR, which is the signal with respect to the general background noise. This is because CPD is part of the CSD and CPD detection actually means detecting its signal on top of the CSD background it is embedded in. This makes CPD detection more difficult than the usual object vs background noise detection.

Finally, the fluxes are also converted to apparent magnitudes at 100 pc. The zero magnitude fluxes used for conversion are: $F_0 = 1587$ Jy for J band, 1074 Jy for H band, 653 Jy for Ks band, 253 Jy for L band, 150 Jy for M band, 34.9 for N band, 18 and 8 for F1500W and F2100W in Q band⁷.

The fluxes in Jy and magnitude as well as the SNR values for each instrument at 0° inclination are summarized in tables following the corresponding simulated images in the next section.

5.3 Results for each instrument

5.3.1 JWST/NIRCam

Fig 5.1, 5.2 and 5.3 showed that a forming planet at 30 AU can be observed in all 5 NIRCam bands simulated, if the planet has 5 or 10 Jupiter masses and the disk is in a small inclination. For 50 AU, only 10-Jupiter mass planets can be seen in all bands, and a 5-Jupiter mass planet starts to show up from $3 \mu\text{m}$. For all images, the disk structure can be imaged. For 5- and 10- Jupiter mass planets, a clear gap is carved by the forming planet. For 1-Jupiter and Saturn mass planets, the gap is shallow or almost not visible. The planet brightness goes up with longer wavelengths. Above $3 \mu\text{m}$, the flux of high mass planets dominates the images (as seen in Fig 5.1b and 5.2b) and the bright PSF hides the background CSD. Fig 5.3 shows that even in 60° inclination, the high mass planets can still be observed for wavelength larger than $2 \mu\text{m}$. Comparing 50 AU observations to 30 AU, the latter results in a higher CPD brightness in all cases. For some images with bright point

⁷<https://www.gemini.edu/observing/resources/magnitudes-and-fluxes/conversions-between-magnitudes-and-flux>

sources (e.g. $10 M_{jup}$ F356W in Fig 5.1 and 5.2), the PSF edge is visible. This is a known limitation of the `Mirage` simulator, as discussed in 4.2.1.

From Table 5.2, it can be found that a SNR value of 1.93 (corresponding to the case of $5 jup30au$ F115W) can already lead to a visually observable CPD bright spot on the image. For the next smaller SNR value of 1.38 ($5 jup50au$ F150W), the CPD cannot be visually seen on the corresponding image. Thus, for NIRCam, any SNR value > 1.93 should clearly be considered as a CPD detection. With this criterion, no planet with mass less than $5 M_{jup}$ is detected. For bright signals that are dominate on the image, the corresponding SNR value is on the order $\sim 10^2$.

5.3.2 JWST/NIRISS

The results from NIRISS as seen in Fig 5.4, 5.5 and 5.6 are similar to those from NIRCam, except that the detection at F115W and F150W of $5 jup30au$ case is questionable. There is no clear visually distinguishable signal, and the SNR value from Table 5.3 is 1.32, below the detection limit we have found for NIRCam. More sophisticated stellar PSF subtraction technique are needed to confirm the detection in this case. The next larger SNR is 2.69 for the case $10 jup50au$ F115W and the CPD is seen on the image, so we can safely say that $SNR > 2.69$ is considered as detection for NIRISS. No planet less than $5 M_{jup}$ is detected either. In general, the obtained magnitudes in Table 5.3 are close to the ones obtained from NIRCam. The SNR values are also on the same order of magnitude. This is expected, as the two instruments share the same simulator. In short wavelengths ($< 2 \mu m$), NIRCam has a better spatial resolution than NIRISS, so it is preferred in the imaging of CPD. The higher resolution could be the reason that the $5 jup30au$ case at F115W and F150W are better detected by NIRCam than NIRISS.

5.3.3 JWST/MIRI

In the mid-infrared, Fig 5.7, 5.8 and 5.9 shows that MIRI can observe 5 and 10 Jupiter mass planets in all 3 studied filters. The circumstellar disk is faint in these wavelengths and does not appear in the images. For these cases, the planet PSF is dominant in the image. For the lower planet mass cases, flux is concentrated in the image center, but the inner ring of the disk and the star can not be resolved, and the system shows up as a continuum of flux. The fact that the width of the bright area stays the same but the height decreases with increasing inclination indicates that this is indeed the disk that is imaged. In $15 \mu m$ and $21 \mu m$, the planet-star system of size 30 AU or 50 AU are barely resolved. It shall be noted that among all instruments, the signal from 1-Jupiter mass planet is only observable in MIRI F1500W and F2100W filters for 30 AU cases (see Fig 5.7b, 5.8b and 5.9b). These are the longest wavelengths covered by the instrument in this study. Below these wavelengths, the 1-Jupiter mass planet does not even show up in the RADMC3D intensity images, thus they are not possible to be detected by the simulated images. However, in wavelengths longer than $15 \mu m$, the resolution is limited by the λ/D

Rayleigh criterion and the planet can only show up as a bright region on the left of the image, but not a clear point source.

In the case of MIRI, the SNR values reported in Table 5.4 shall be interpreted with caution, since the aperture defined from its PSF FWHM is close to or in some cases (F2100W for 50 AU, F1500W and F2100W for 30 AU) even larger than half of the image, which means the defined CPD and anti-CPD regions are close to or even overlap each other. The calculated SNR value is then lower, since there are still contribution of CPD flux in the anti-CPD region, and those contribution gets subtracted or divided. Therefore the CPD-only and SNR values in Table 5.4 are not comparable with the other instruments. They are also not comparable within themselves if not coming from the same filter and separation, since the above-mentioned effect increases with larger PSF size on the image. Thus, we see from Table 5.4 that e.g. for 1jup50au F1000W case, the SNR is 1.41, which is higher than SNR = 1.33 for 1jup30au F2100W, but in the latter image a clear brightness asymmetry can be seen, whereas no clear asymmetry can be seen from the image of former case. Looking at all SNR values in Table 5.4 and their corresponding images, it can be concluded that all cases with $\text{SNR} > 1.78$ are obviously detected, and smaller SNR needs to be inspected case by case to determine if there is detection of CPD. There is no single criterion like the other instruments, due to the limitation of our method for SNR calculation.

5.3.4 ELT/MICADO

Among all the instruments studied, MICADO gives the highest spatial resolution and allows more substructures of the disk to be observed, as seen in Fig 5.10, 5.11 and 5.12. In the short wavelengths covered by MICADO, only 10-Jupiter mass planets in all bands and 5-Jupiter mass planets in Ks band are bright enough to be detected. Even if a planet is buried in surrounding optically thick dust, the spiral features caused by gas accreting onto the planet can still be observable in some cases (e.g. see last row of Fig 5.10b). To reach this level of resolution, high level of AO correction is certainly required.

The SNR values reported in Table 5.5 are also more robust due to the high resolution. The CPD and anti-CPD aperture are much smaller relative to the image than the JWST instruments, so they only contain signal from a small region enclosing the CPD/anti-CPD. It can be seen from Table 5.5 that there is a clear distinction between whether the CPD is detected or not. For cases with $\text{SNR} > 6$ there is evidently a detection and for the non-detection cases the SNRs are well below 2. It is worth noting that for cases where no CPD is visually seen but the gas spirals around CPD can be seen, e.g. the 1jup30au case in all filters, the SNR values are larger than 1. This suggests that SNR between 1-2 can indicate observed substructures in the disk that might be caused by an embedded planet, even though the planet itself is not observed.

5.3.5 ELT/METIS

Like the images from MIRI which are also in mid IR, Fig 5.13, 5.14 and 5.15 from METIS also show that planet with mass above 5 Jupiter can be detected in the 3 bands of consideration. The METIS simulated images are subject to high background noise, so the circumstellar disks are more or less buried in the background. Band N with longest wavelength of $\sim 10 \mu\text{m}$ is still not enough for the 1-Jupiter mass planets to show up.

Comparing the L and M band fluxes in Table 5.6 to those observed by NIRCam/NIRISS (F356W and F444W), METIS in general gives a lower detected CPD flux (e.g. 2-3 mags fainter for 30 AU cases, 5-7 mags fainter for 50 AU cases). The SNR values from Tables 5.6 are high for detected cases since the background CSD is faint in this wavelength range. A visual inspection shows that any SNR value > 8 indicates an evident detection. The two values between 1-2 are likely due to noise (1sat50au in N2 band and 1jup30au in N2 band). For the case 1jup30au in L band, the SNR = 2.38 could be caused by the spiral feature induced by the planet in the disk, as can be seen in Fig 5.13b (lower left corner).

5.3.6 GMT/GMTIFS

The observed disk structure by the self-simulated GMTIFS shown in Fig 5.16, 5.17 and 5.18 are similar to that produced by the NIRCam and MICADO simulators, with a bright inner ring, a fainter outer ring and a gap in between carved by the embedded planet. The scenario for CPD detection is also similar to previous cases, where only high mass planets can be observed. The gap opened by a 1-Jupiter mass planet is more clearly seen by GMT than in the NIRCam images.

Checking the SNR values from Table 5.7 with images, one can conclude that a SNR > 1.94 (corresponding to the case 5jup30au in hJ band) leads to a evident CPD detection. Comparing the CPD fluxes from Table 5.7 to previous instruments at same wavelengths, the GMT J, H, K band fluxes for $10 M_{jup}$ 30 AU detections are close to those given by NIRCam (variation around 1 mags), but lower by 1-3 magnitudes than the fluxes given by MICADO. The $10 M_{jup}$ 50 AU fluxes are lower by 2-4 mags than NIRCam, and lower by 6-8 mags than MICADO.

5.4 Discussion

Most of the synthetic observations shows a similar structure, where the disk has a bright inner ring and dim outer ring. Between the two rings a gap is opened by the forming planet, and for the cases where the gap is deep, the CPD is detected as a bright spot. In most cases the 5- and 10-Jupiter mass planets can be detected. There are two reasons contributing to the observability of these massive planets. First, only planet massive enough can open a deep gap in the CSD, which makes the CPD surroundings optically thin. Planets embedded in CSDs are subject to high extinction due to the optically thick environment, which severely decrease their observability. (e.g. see Sanchis et al. [2020]) Second, the accretion shock front formed

from the vertical inflow onto the surface of CPDs is strong and hot. The more massive planets causes a higher inflow velocity which then creates a hotter shock front, and contributes to the observability of CPD (Szulágyi & Garufi, 2021). Planets at 30 AU are brighter than the 50 AU cases, since the CPD gets cooler as it is further away from the star (Szulágyi et al., 2019).

Around $10 \mu\text{m}$, CPD has the highest contrast from CSD. For smaller wavelengths, scattered stellar light contributes to the brightness of CSD, and for longer wavelength the thermal emission of CSD increases. In J, H band, only 10-Jupiter mass planets from at 30 AU can be detected. For shorter wavelengths, polarized scattered light are more suitable for CPD observations. For planetary mass smaller than $5 M_{jup}$, wavelength longer than $15 \mu\text{m}$ is needed. The currently planned ground-based telescopes which can provide enough spatial resolution in this wavelength does not have instruments covering this wavelength range.

The SNR value for determining whether there is a detection or not is different for each instrument. In general, a $\text{SNR} > 2$ already indicate a detection. The non-detection of less massive planets in simulated observations could also be due to the limitations and uncertainties in our study methods. The dust is not separately treated in the simulation but assumed with a fixed gas-to-dust ratio of 0.01. The hydrodynamic simulation is also without proper treatment for the evolution of the planet mass and radius. This setting will largely affect the accretion luminosity of the CPD. Moreover, many physics are not covered in the hydrodynamic simulation, e.g. hydrogen dissociation and ionization, magnetic fields and self-gravity. Other assumptions during the processing steps such as the choice of opacity tables and flux conversion factors also introduces error to the final result.

Figure 5.1: Simulated NIRCam observations in 0° inclination at 100 pc. The columns represent the 5 filters simulated, and the rows represent models with different planetary masses. The planet is always at 9 o'clock direction on the images. The central star is masked with a circle. The color scale is unit of \log_{10} DN.

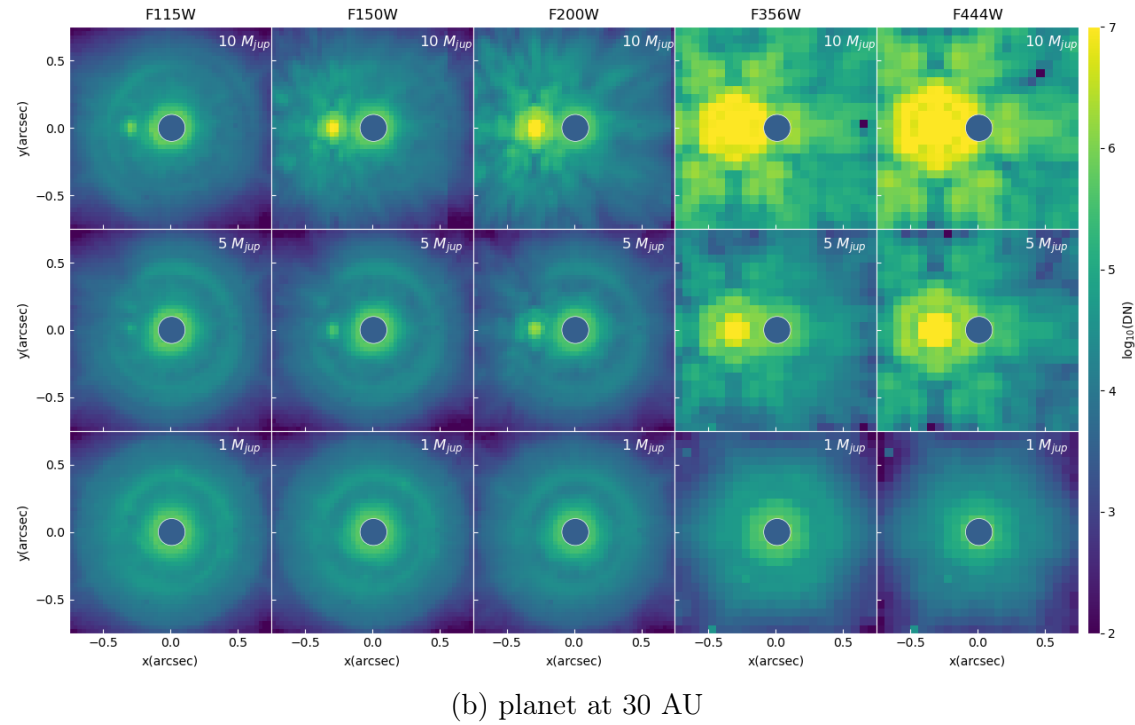
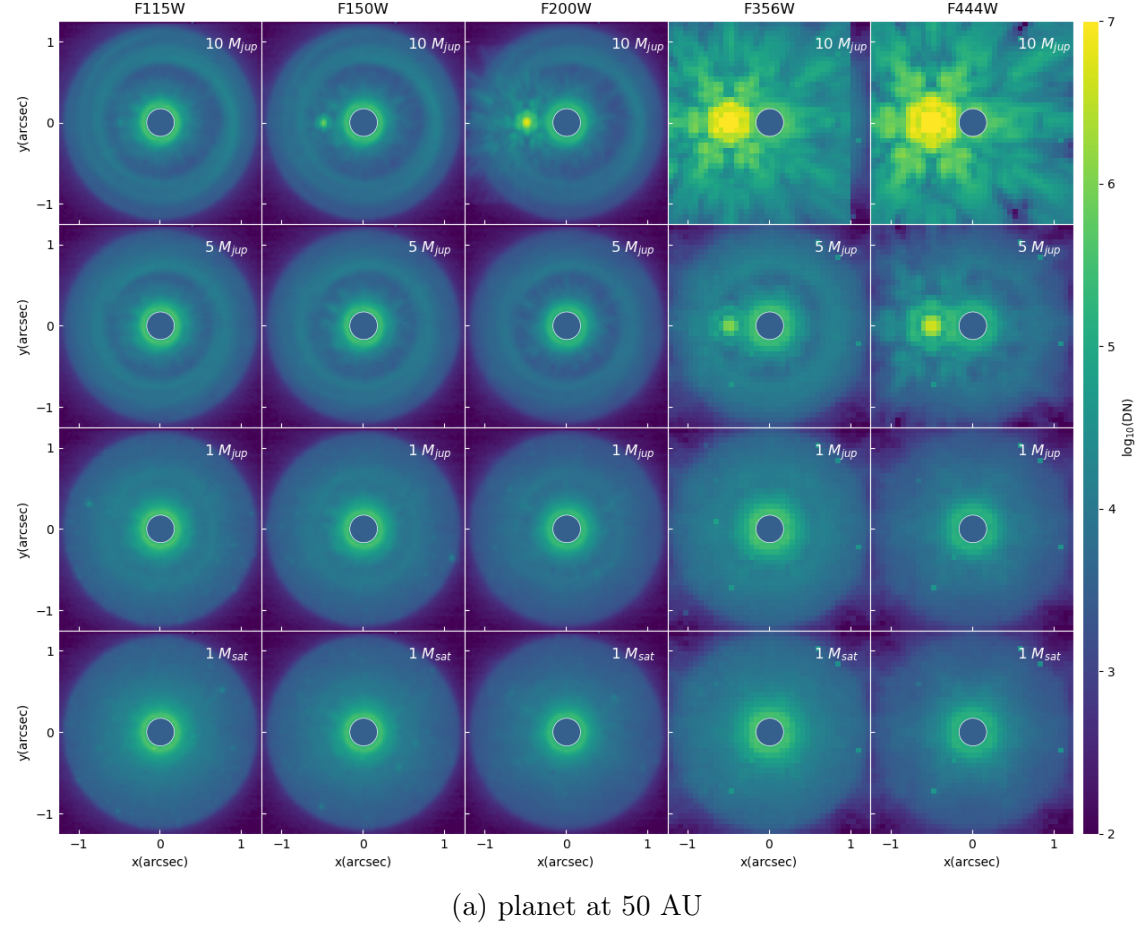


Figure 5.2: Simulated NIRCam observations, same as Fig 5.1 but in 30° inclination.

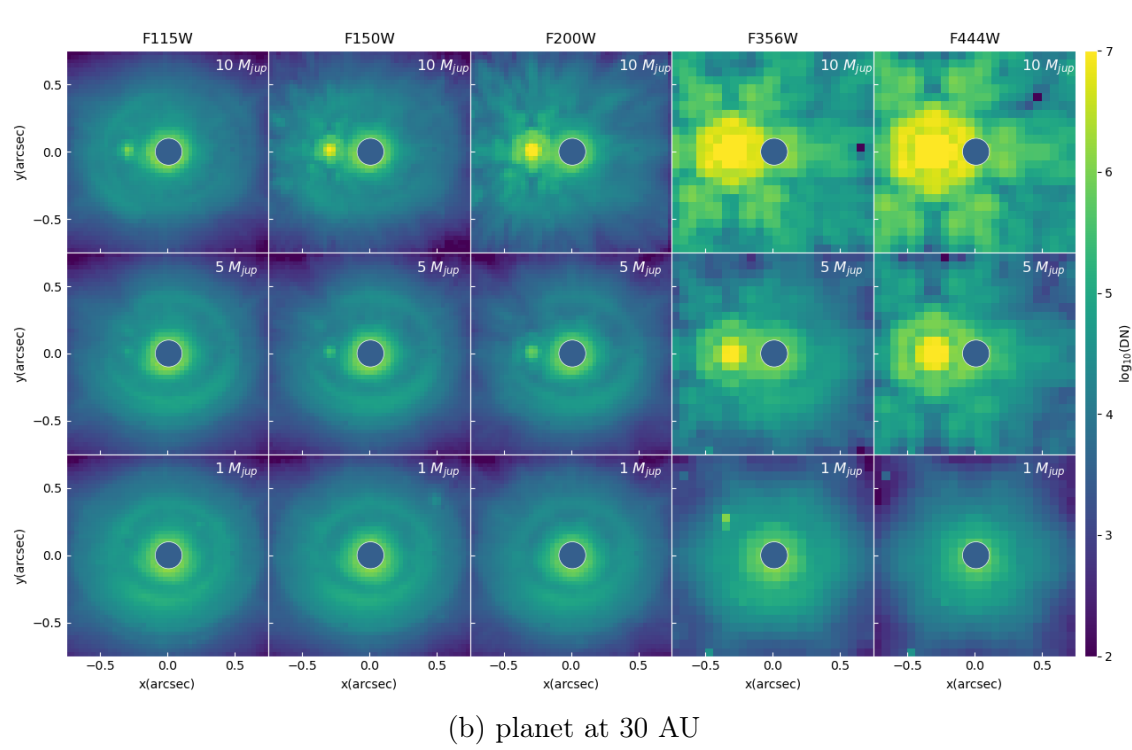
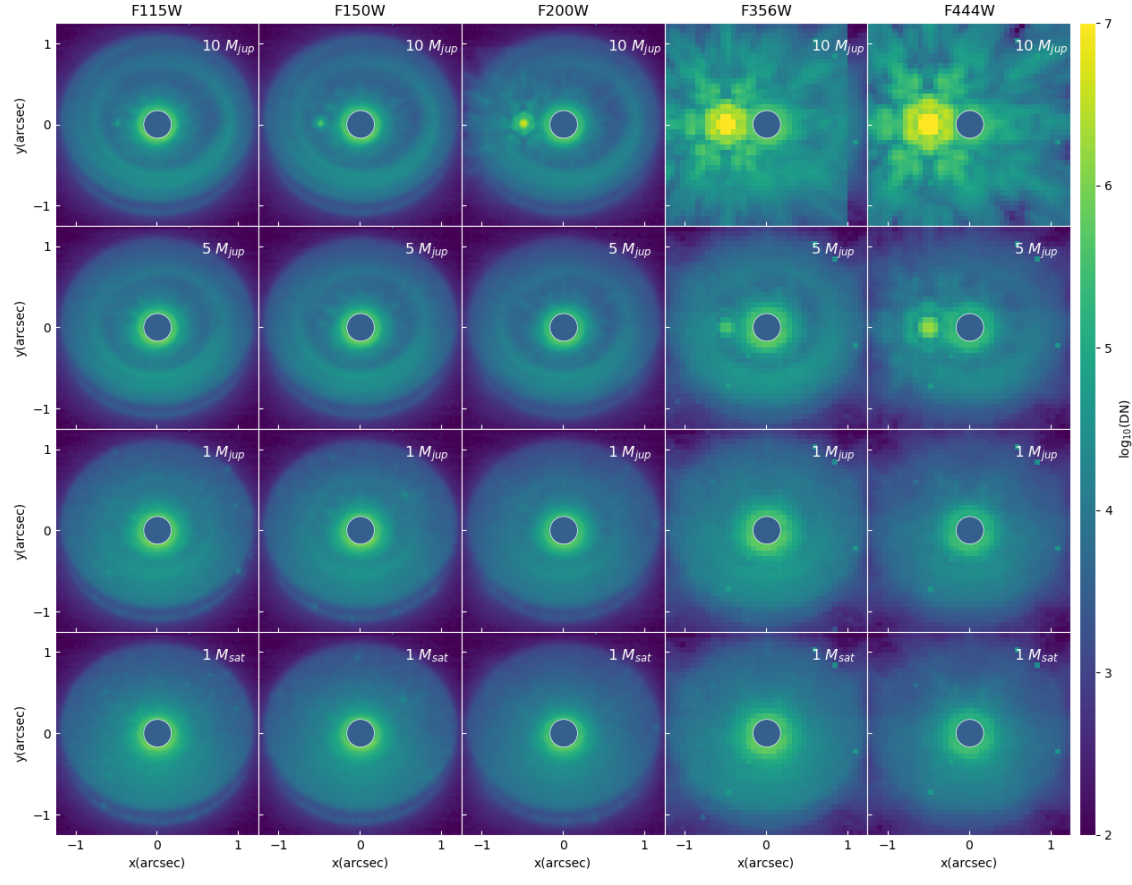


Figure 5.3: Simulated NIRCam observations, same as Fig 5.1 but in 60° inclination.

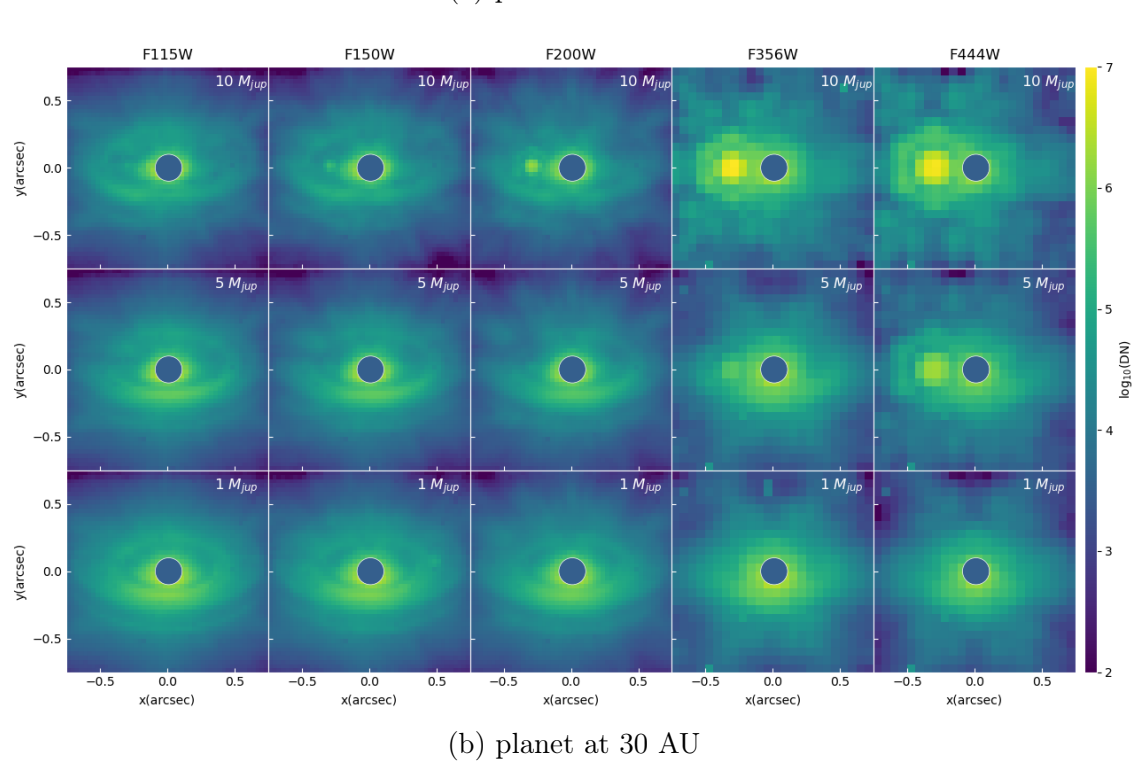
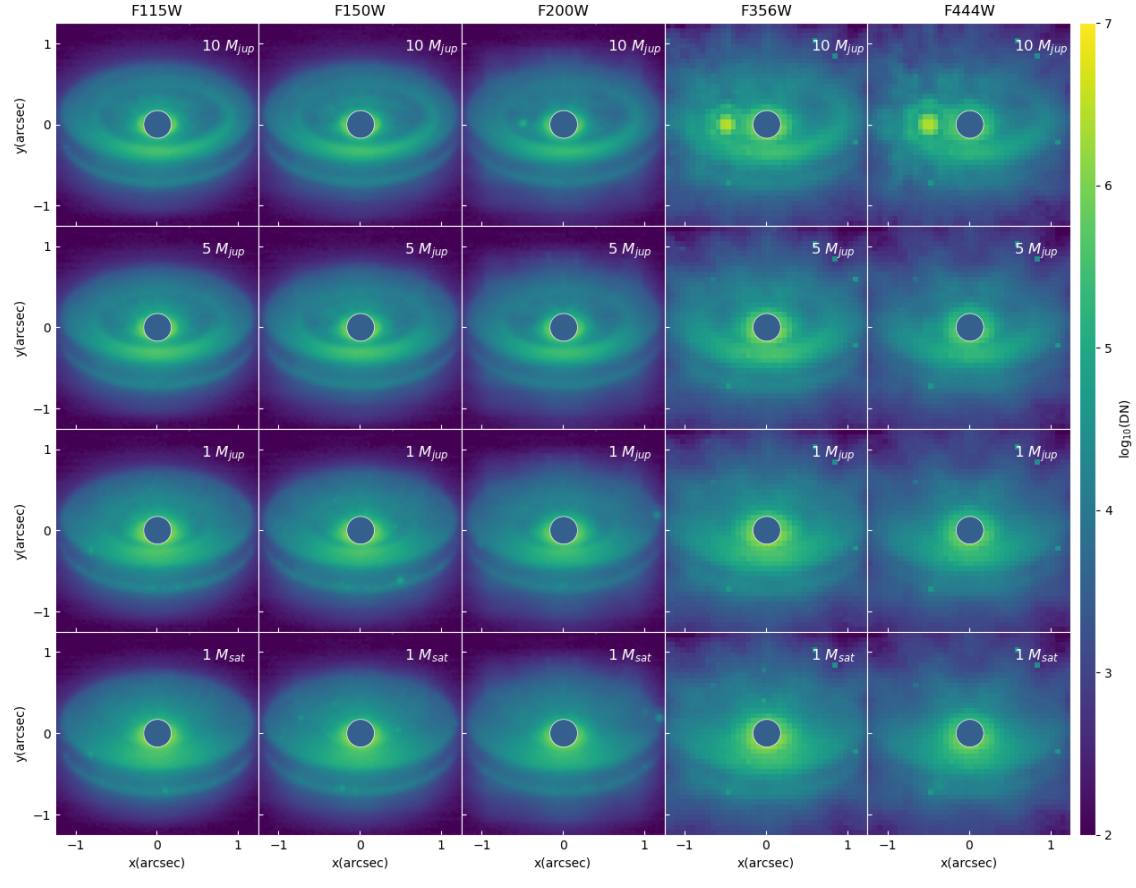


Table 5.2: Circumplanetary disk fluxes and magnitudes at 100 pc as imaged by JWST/NIRCam. Columns named **CPD** reports the CPD flux subtracted by background noise, whereas **CPD only** reports CPD flux minus the flux of the CSD 180° across the planet, i.e. the anti-CPD flux. SNR_{CPD} values are given by the ratio between CPD flux (without subtraction by anti-CPD) and anti-CPD flux.

model	filter	CPD (Jy)	CPD only (Jy)	CPD (mag)	CPD only (mag)	SNR_{CPD}
10jup50au	F115W	1.33e-05	8.26e-06	20.19	20.71	2.65
	F150W	3.68e-04	3.61e-04	16.16	16.18	55.28
	F200W	3.85e-03	3.84e-03	13.07	13.08	417.72
	F356W	5.87e-02	5.86e-02	9.09	9.09	646.11
	F444W	9.84e-02	9.82e-02	7.96	7.96	488.85
5jup50au	F115W	6.76e-06	1.32e-06	20.93	22.70	1.24
	F150W	9.79e-06	2.69e-06	20.10	21.50	1.38
	F200W	9.46e-06	1.25e-07	19.60	24.30	1.01
	F356W	4.78e-04	4.57e-04	14.31	14.36	22.31
	F444W	2.31e-03	2.30e-03	12.03	12.04	144.34
1jup50au	F115W	9.35e-06	1.25e-06	20.57	22.76	1.15
	F150W	1.43e-05	2.65e-06	19.69	21.52	1.23
	F200W	1.48e-05	/	19.11	/	/
	F356W	2.86e-05	/	17.37	/	/
	F444W	1.64e-05	/	17.40	/	/
1sat50au	F115W	1.21e-05	1.17e-06	20.29	22.83	1.11
	F150W	1.81e-05	2.62e-06	19.43	21.53	1.17
	F200W	1.97e-05	4.32e-07	18.80	22.95	1.02
	F356W	3.42e-05	/	17.17	/	/
	F444W	1.91e-05	/	17.24	/	/
10jup30au	F115W	3.77e-04	3.58e-04	16.56	16.62	19.68
	F150W	7.49e-03	7.45e-03	12.89	12.90	218.62
	F200W	2.03e-02	2.03e-02	11.27	11.27	324.61
	F356W	1.11e-01	1.11e-01	8.39	8.40	184.31
	F444W	1.63e-01	1.62e-01	7.41	7.42	141.33
5jup30au	F115W	4.20e-05	2.03e-05	18.94	19.73	1.93
	F150W	1.97e-04	1.67e-04	16.84	17.02	6.49
	F200W	9.47e-04	9.00e-04	14.60	14.65	20.28
	F356W	9.73e-03	9.61e-03	11.04	11.05	81.42
	F444W	2.23e-02	2.21e-02	9.57	9.58	113.25
1jup30au	F115W	2.99e-05	9.06e-07	19.31	23.11	1.03
	F150W	3.96e-05	/	18.58	/	/
	F200W	4.38e-05	/	17.93	/	/
	F356W	8.15e-05	/	16.23	/	/
	F444W	5.24e-05	/	16.14	/	/

Figure 5.4: Simulated NIRISS observations in 0° inclination at 100 pc. The columns represent the 5 filters simulated, and the rows represent models with different planetary masses. The planet is always at 9 o'clock direction on the images. The central star is masked with a circle. The color scale is unit of \log_{10} DN.

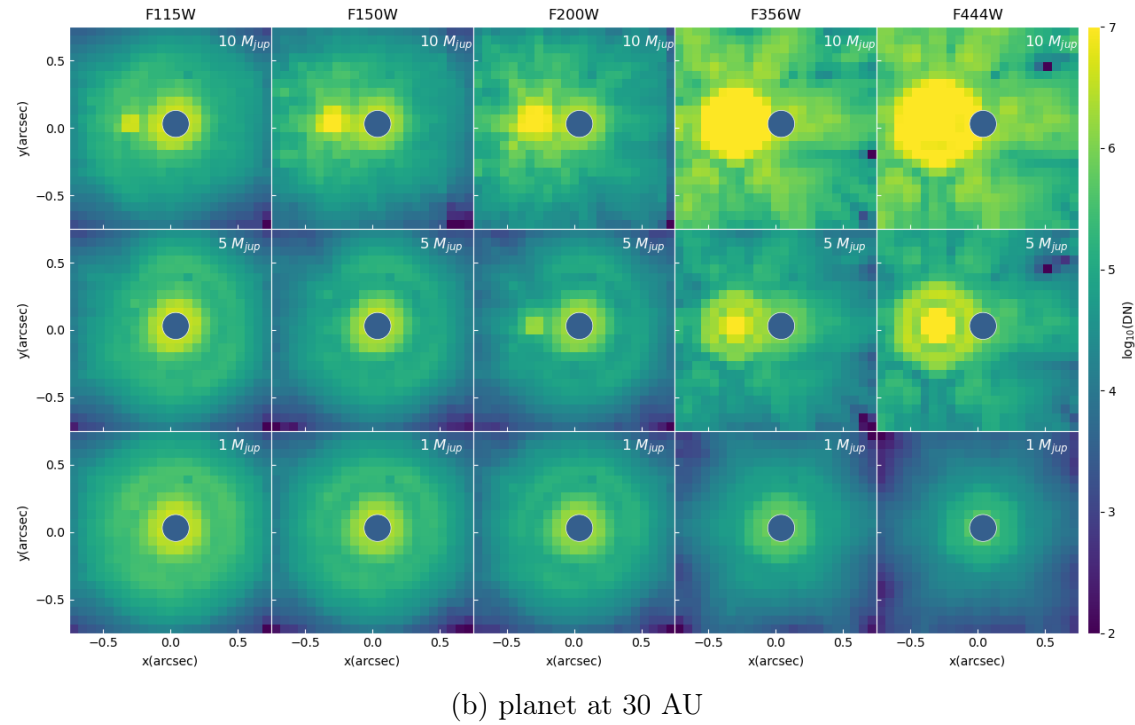
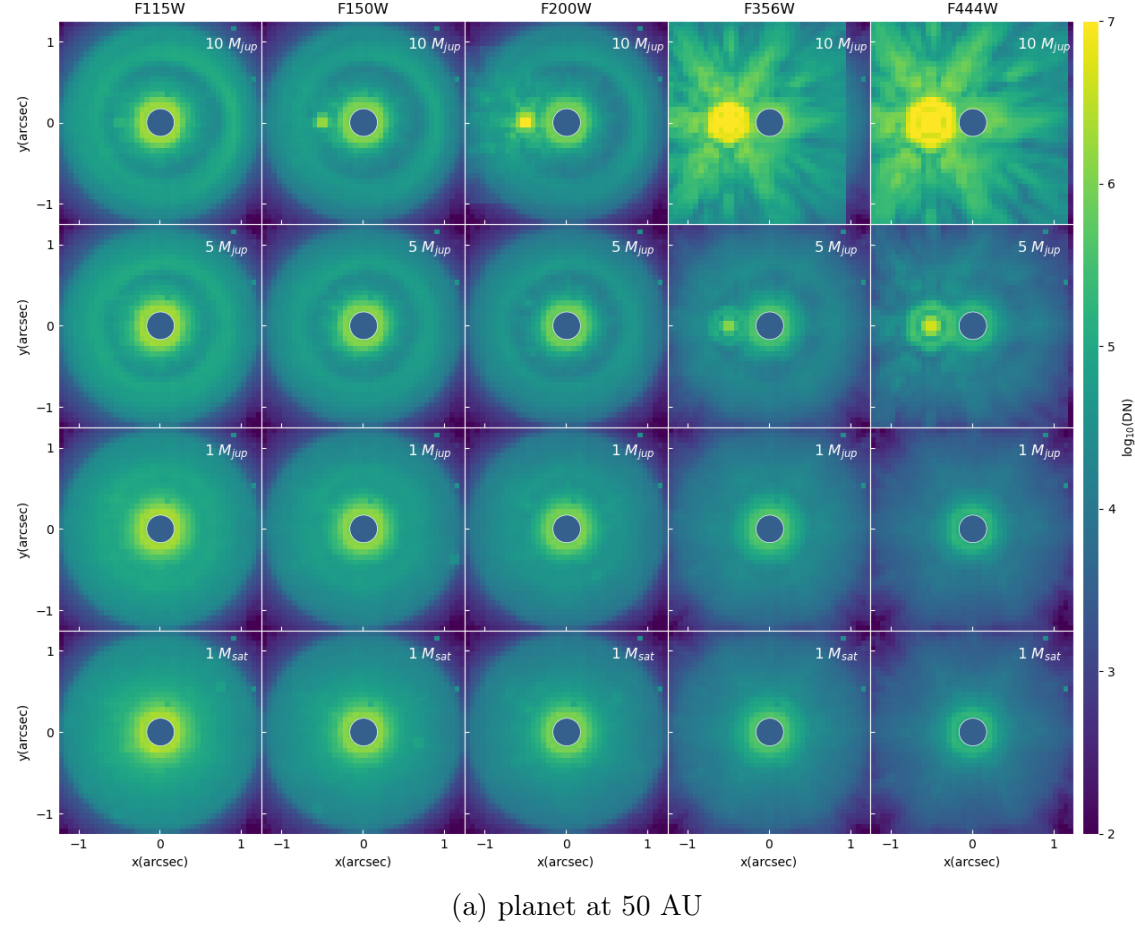


Figure 5.5: Simulated NIRISS observations, same as Fig 5.4 but in 30° inclination.

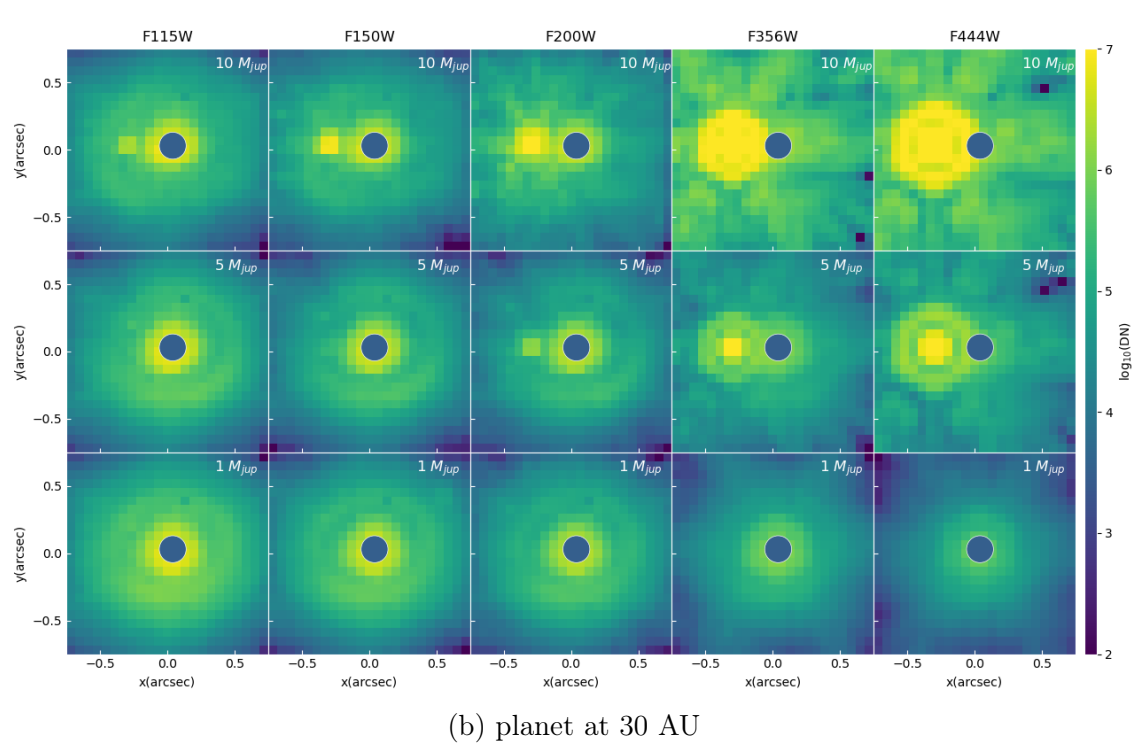
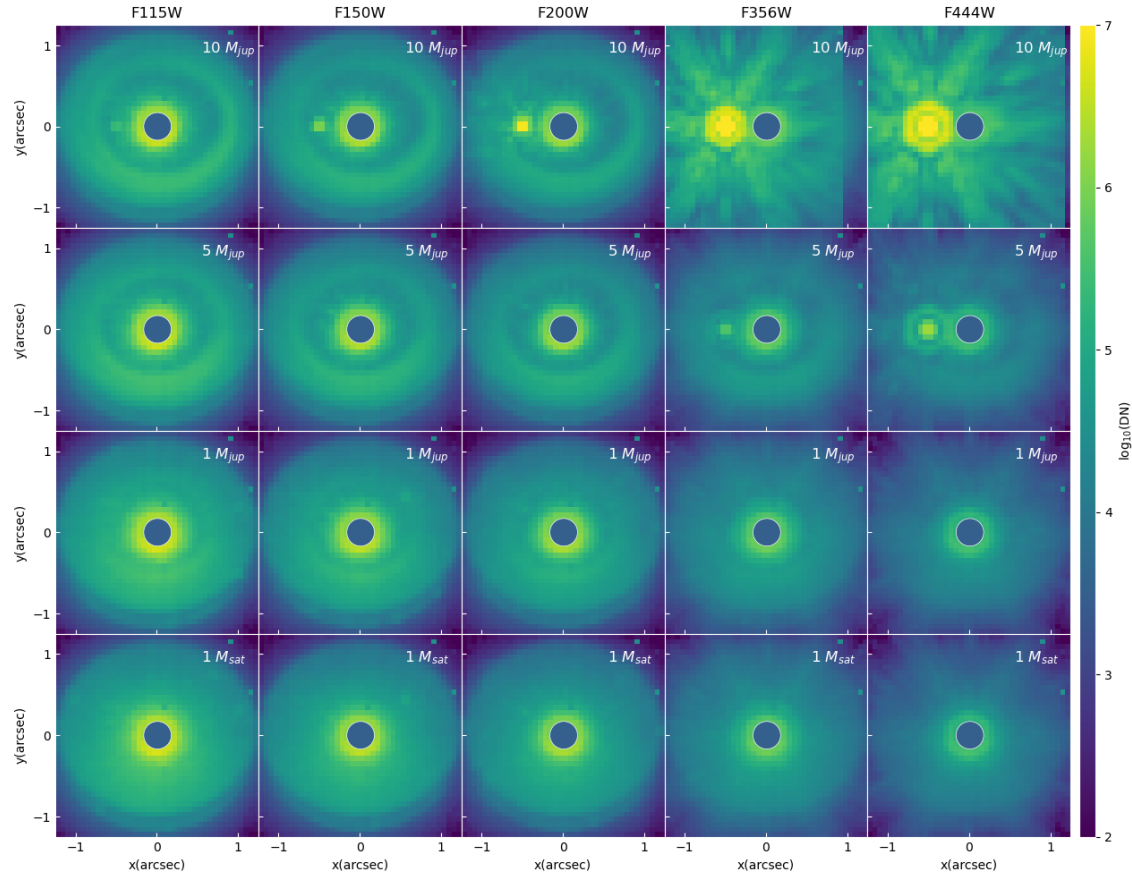
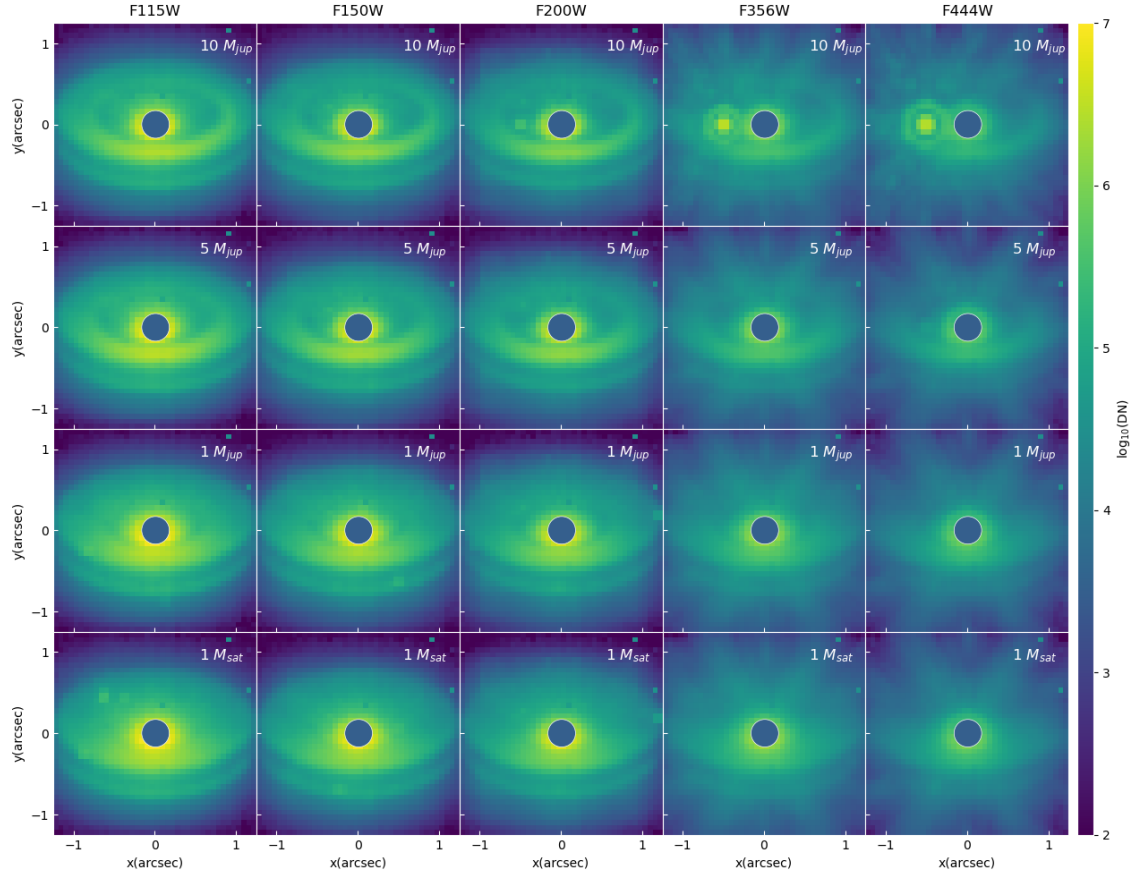
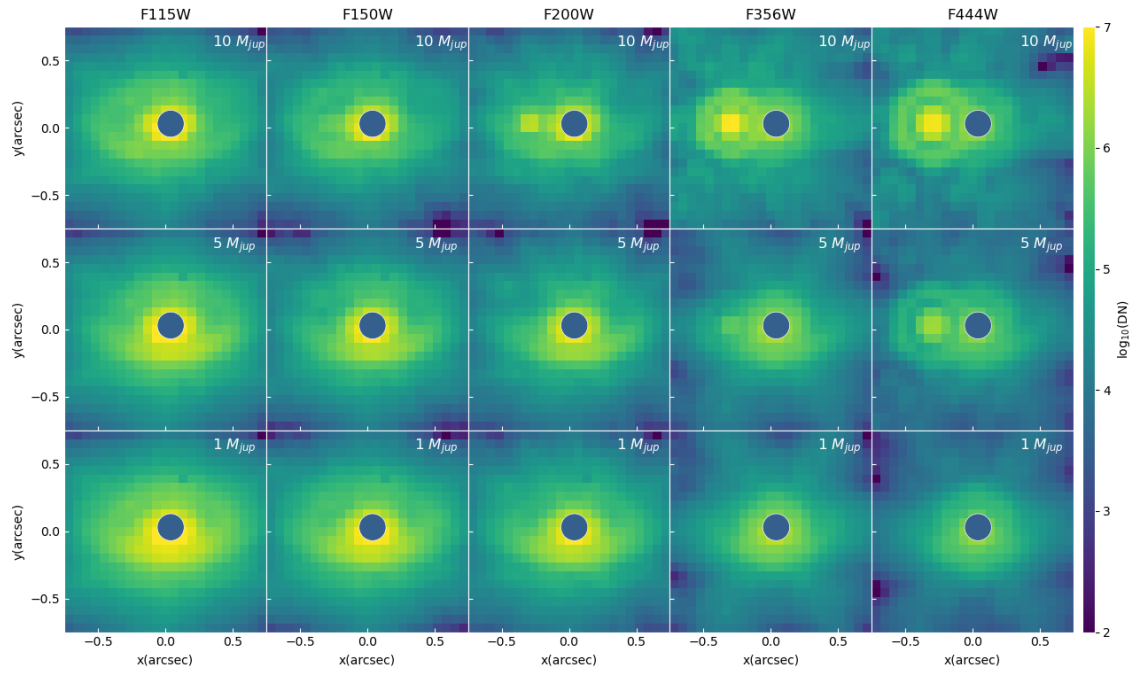


Figure 5.6: Simulated NIRISS observations, same as Fig 5.4 but in 60° inclination.



(a) planet at 50 AU

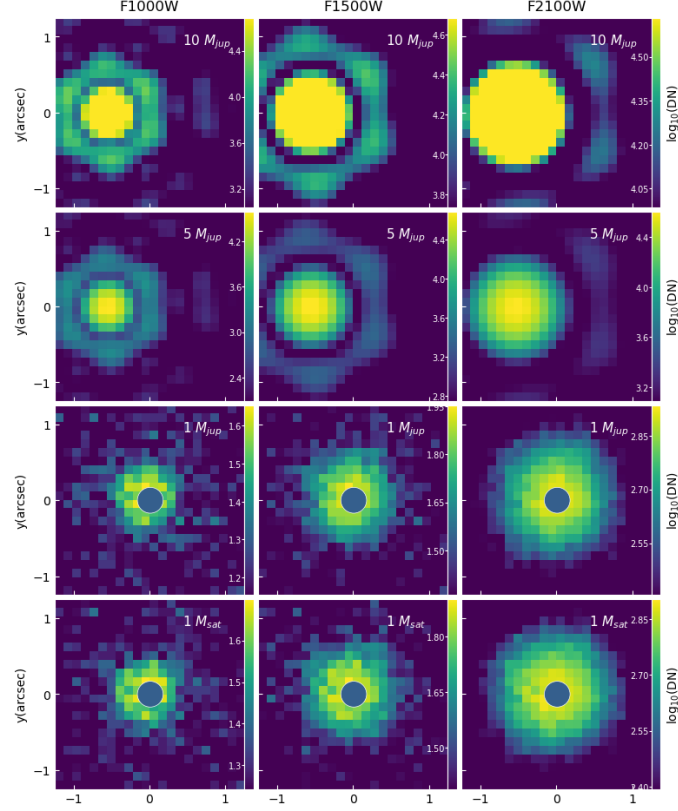


(b) planet at 30 AU

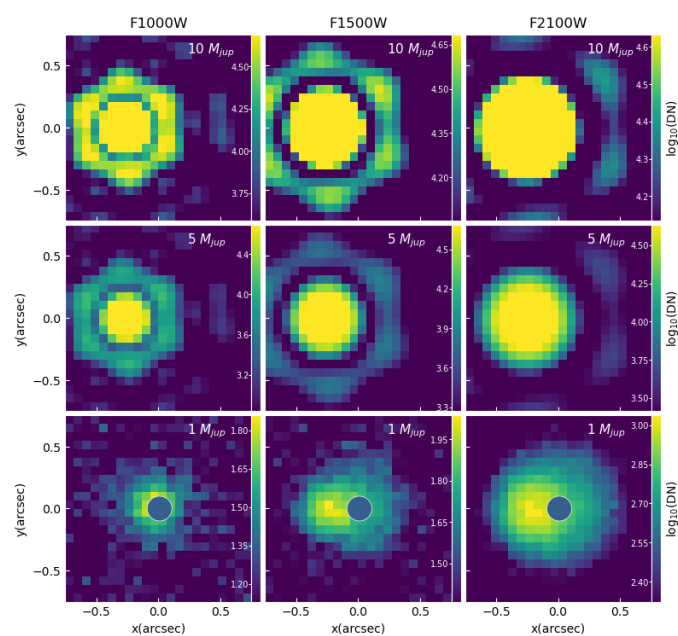
Table 5.3: Circumplanetary disk fluxes and magnitudes at 100 pc as imaged by JWST/NIRISS. Columns named **CPD** reports the CPD flux subtracted by background noise, whereas **CPD only** reports CPD flux minus the flux of the CSD 180° across the planet, i.e. the anti-CPD flux. SNR_{CPD} values are given by the ratio between CPD flux (without subtraction by anti-CPD) and anti-CPD flux.

model	filter	CPD (Jy)	CPD only (Jy)	CPD (mag)	CPD only (mag)	SNR_{CPD}
10jup50au	F115W	3.92e-05	2.47e-05	19.02	19.52	2.69
	F150W	4.57e-04	4.47e-04	15.93	15.95	47.16
	F200W	4.03e-03	4.02e-03	13.02	13.03	614.12
	F356W	5.22e-02	5.20e-02	9.21	9.22	278.52
	F444W	8.68e-02	8.65e-02	8.09	8.10	239.13
5jup50au	F115W	2.15e-05	5.24e-06	19.67	21.20	1.32
	F150W	1.41e-05	3.44e-06	19.70	21.23	1.32
	F200W	8.69e-06	1.58e-06	19.69	21.54	1.22
	F356W	4.33e-04	4.08e-04	14.42	14.48	17.25
	F444W	2.05e-03	2.03e-03	12.16	12.17	94.59
1jup50au	F115W	3.18e-05	5.42e-06	19.25	21.17	1.21
	F150W	2.21e-05	4.03e-06	19.21	21.07	1.22
	F200W	1.34e-05	/	19.22	/	/
	F356W	3.64e-05	1.17e-06	17.11	20.84	1.03
	F444W	2.03e-05	1.04e-06	17.17	20.39	1.05
1sat50au	F115W	4.12e-05	4.88e-06	18.97	21.28	1.13
	F150W	2.79e-05	4.32e-06	18.96	20.99	1.18
	F200W	1.79e-05	2.30e-06	18.91	21.13	1.15
	F356W	4.21e-05	1.23e-06	16.95	20.78	1.03
	F444W	2.30e-05	9.45e-07	17.04	20.50	1.04
10jup30au	F115W	5.47e-04	5.20e-04	16.16	16.21	20.49
	F150W	8.56e-03	8.52e-03	12.75	12.75	221.39
	F200W	1.95e-02	1.95e-02	11.31	11.31	545.38
	F356W	8.46e-02	8.38e-02	8.69	8.70	101.77
	F444W	1.35e-01	1.34e-01	7.61	7.62	112.83
5jup30au	F115W	2.83e-05	/	19.37	/	/
	F150W	3.85e-05	2.38e-06	18.61	21.64	1.07
	F200W	4.33e-04	4.09e-04	15.45	15.51	17.86
	F356W	7.43e-03	7.29e-03	11.33	11.35	54.63
	F444W	1.85e-02	1.83e-02	9.77	9.78	88.09
1jup30au	F115W	4.90e-05	6.08e-06	18.78	21.04	1.14
	F150W	5.63e-05	/	18.20	/	/
	F200W	3.55e-05	/	18.16	/	/
	F356W	8.85e-05	2.56e-06	16.14	19.99	1.03
	F444W	6.75e-05	6.80e-07	15.87	20.86	1.01

Figure 5.7: Simulated MIRI observations in 0° inclination at 100 pc. The columns represent the 3 filters simulated, and the rows represent models with different planetary masses. The planet is always at 9 o'clock direction on the images. For the 10 and $5 M_{Jup}$ planets, the hexagonal PSF is strong enough to extend to the image center where the star locates. For other cases, the location of central star is masked with a circle. The color scale is unit of \log_{10} DN.



(a) planet at 50 AU



(b) planet at 30 AU

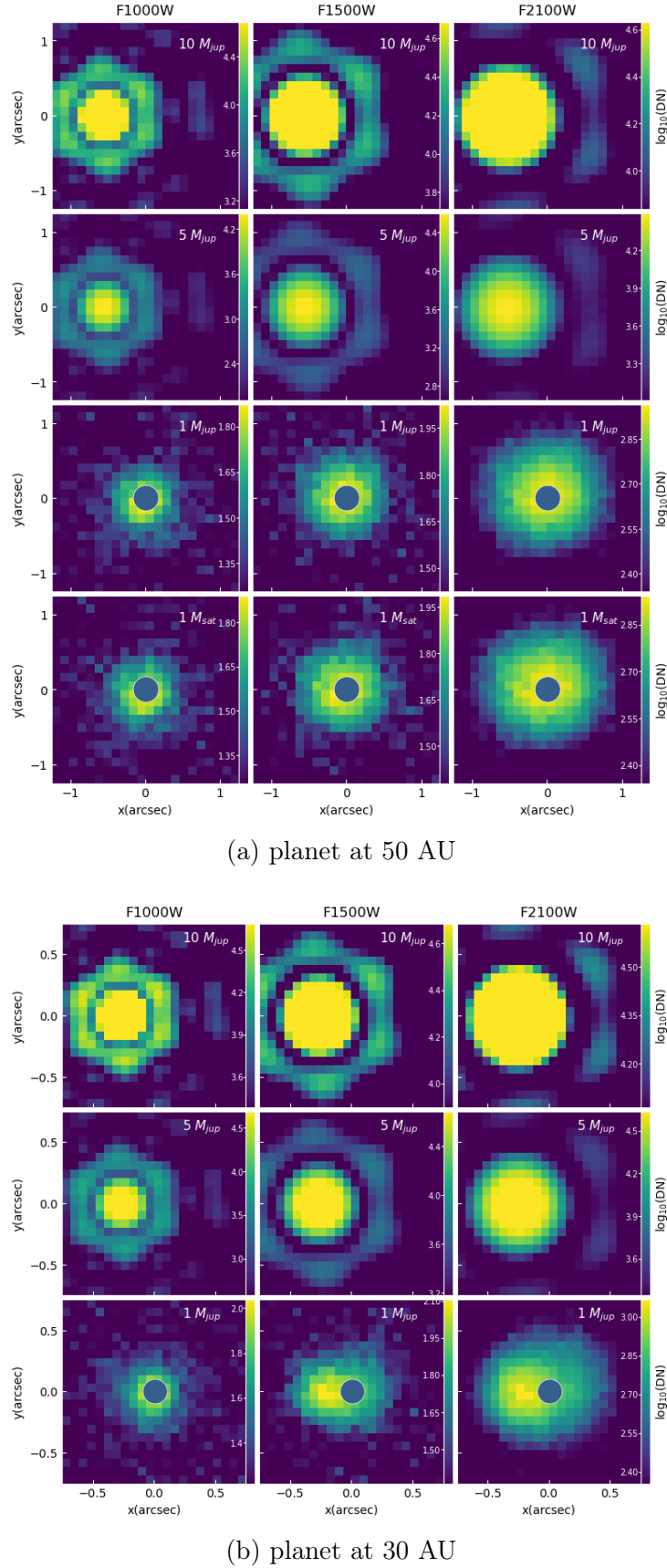
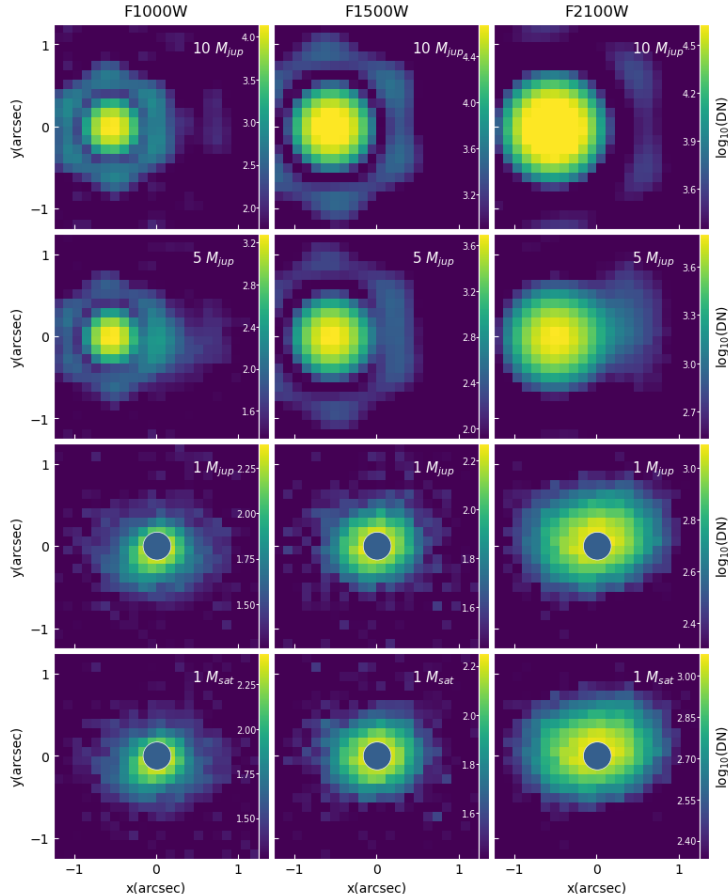
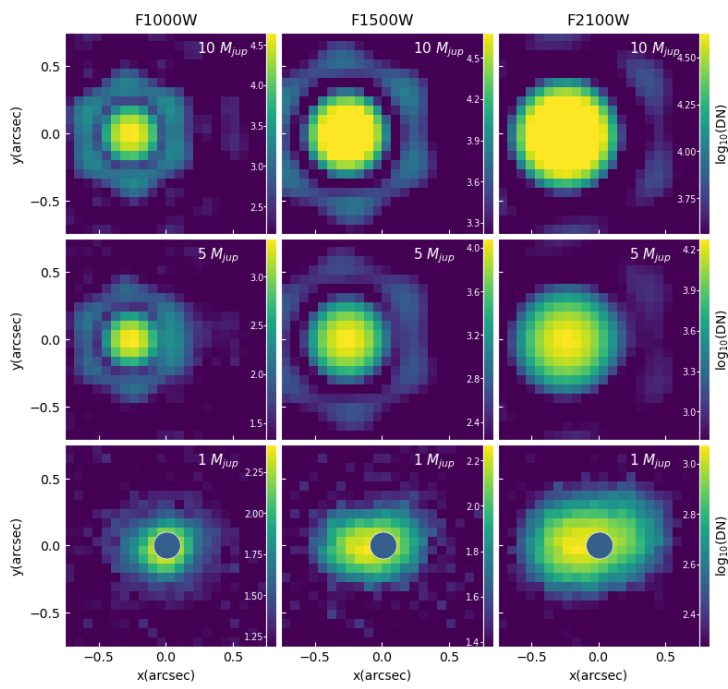
Figure 5.8: Simulated MIRI observations, same as Fig 5.7 but in 30° inclination.

Figure 5.9: Simulated MIRI observations, same as Fig 5.7 but in 60° inclination.



(a) planet at 50 AU



(b) planet at 30 AU

Table 5.4: Circumplanetary disk fluxes and magnitudes at 100 pc as imaged by JWST/MIRI. Columns named **CPD** reports the CPD flux subtracted by background noise, whereas **CPD only** reports CPD flux minus the flux of the CSD 180° across the planet, i.e. the anti-CPD flux. SNR_{CPD} values are given by the ratio between CPD flux (without subtraction by anti-CPD) and anti-CPD flux.

model	filter	CPD (Jy)	CPD only (Jy)	CPD (mag)	CPD only (mag)	SNR_{CPD}
10jup50au	F1000W	2.33e-04	2.25e-04	12.94	12.98	30.13
	F1500W	5.45e-04	4.41e-04	11.30	11.53	5.24
	F2100W	7.55e-04	4.40e-04	10.06	10.65	2.40
5jup50au	F1000W	8.21e-05	8.13e-05	14.07	14.08	99.76
	F1500W	2.27e-04	2.17e-04	12.25	12.30	21.66
	F2100W	2.85e-04	2.25e-04	11.12	11.38	4.77
1jup50au	F1000W	7.03e-08	2.05e-08	21.74	23.08	1.41
	F1500W	4.30e-07	6.18e-08	19.06	21.16	1.17
	F2100W	8.52e-06	2.46e-07	14.93	18.78	1.03
1sat50au	F1000W	7.73e-08	2.19e-08	21.64	23.01	1.39
	F1500W	3.93e-07	5.06e-08	19.15	21.38	1.15
	F2100W	8.63e-06	4.89e-07	14.92	18.03	1.06
10jup30au	F1000W	2.59e-04	2.27e-04	12.82	12.97	8.05
	F1500W	5.68e-04	3.57e-04	11.25	11.76	2.69
	F2100W	8.04e-04	3.54e-04	9.99	10.89	1.78
5jup30au	F1000W	1.98e-04	1.92e-04	13.12	13.15	33.71
	F1500W	4.06e-04	3.70e-04	11.62	11.72	11.20
	F2100W	5.03e-04	3.22e-04	10.50	10.99	2.78
1jup30au	F1000W	7.47e-08	2.59e-08	21.67	22.82	1.53
	F1500W	5.12e-07	2.29e-07	18.87	19.74	1.81
	F2100W	1.02e-05	2.54e-06	14.74	16.24	1.33

Figure 5.10: Simulated MICADO observations in 0° inclination at 100 pc. The columns represent the 3 filters simulated, and the rows represent models with different planetary masses. The planet is always at 9 o'clock direction on the images. The central star is masked with a circle. The color scale is unit of \log_{10} DN.

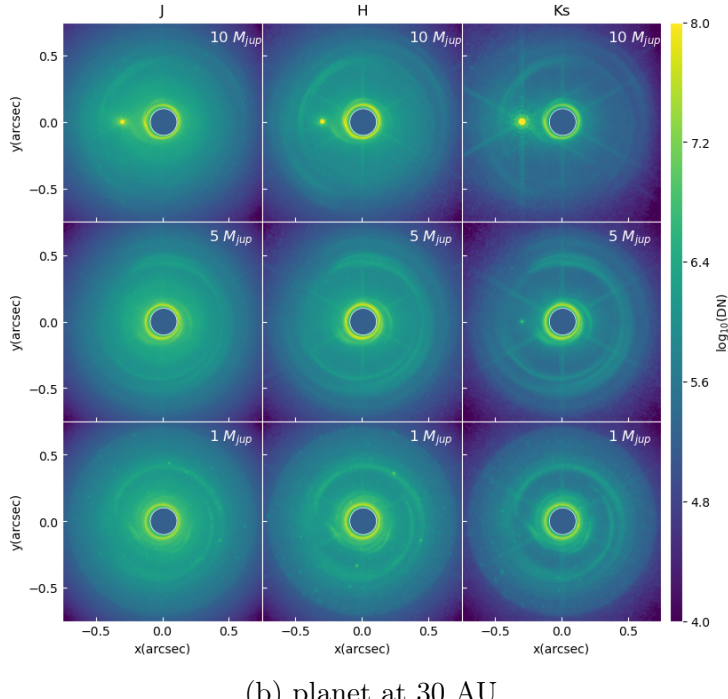
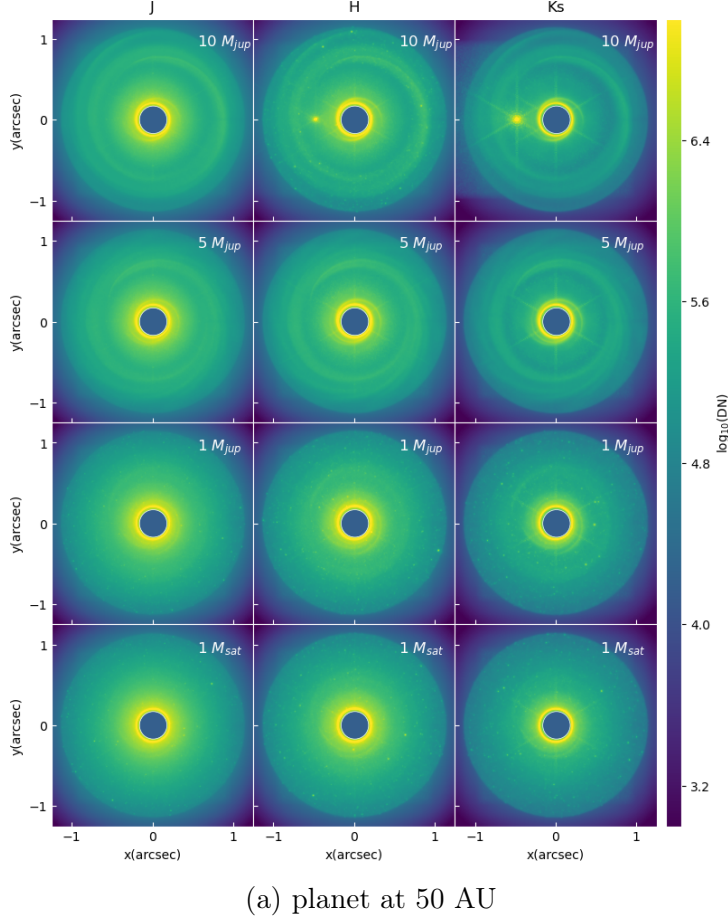
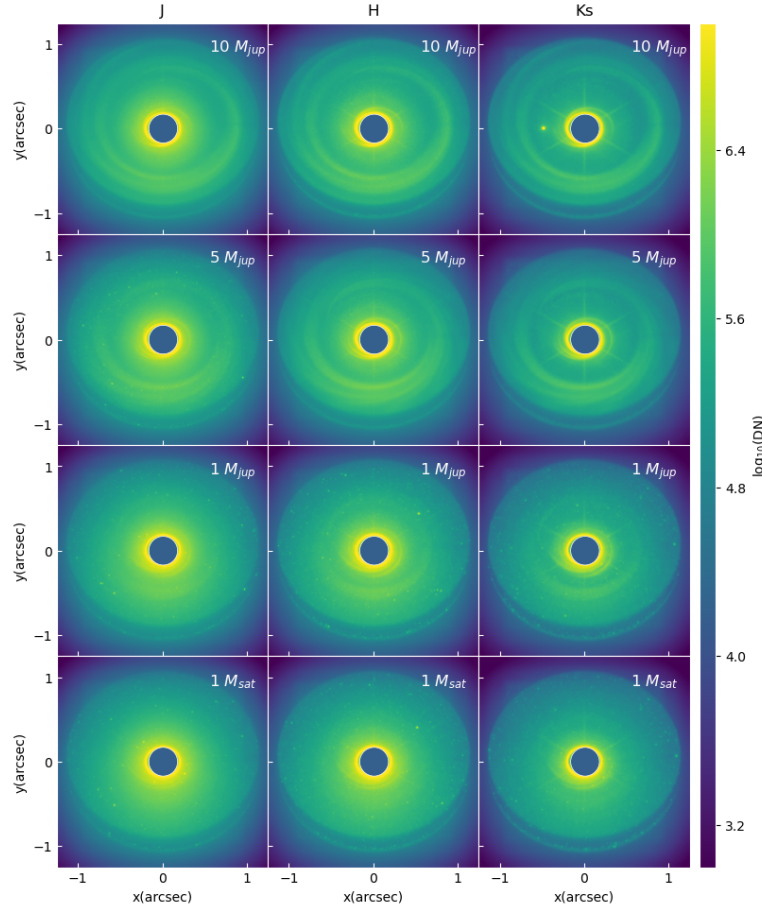
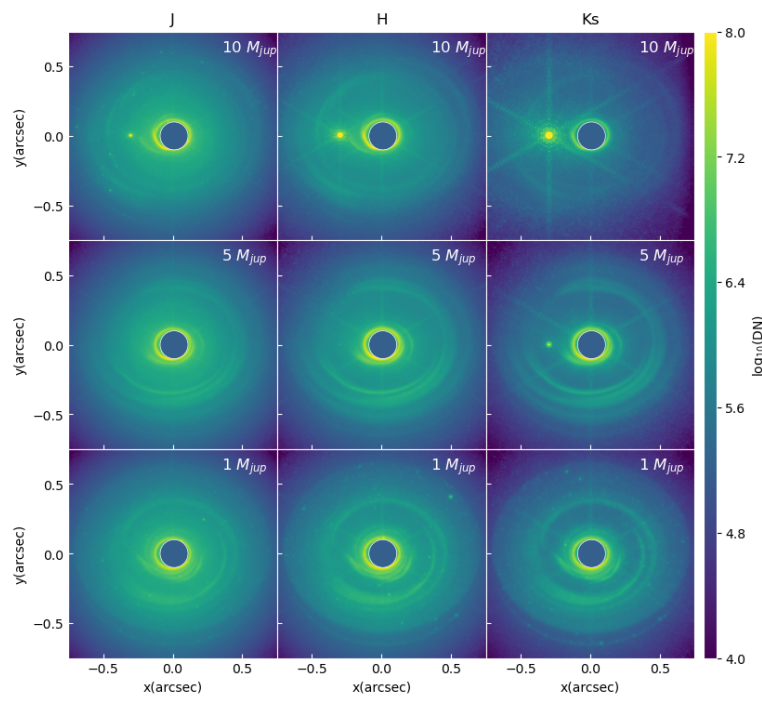


Figure 5.11: Simulated MICADO observations, same as Fig 5.10 but in 30° inclination.



(a) planet at 50 AU



(b) planet at 30 AU

Figure 5.12: Simulated MICADO observations, same as Fig 5.10 but in 60° inclination.

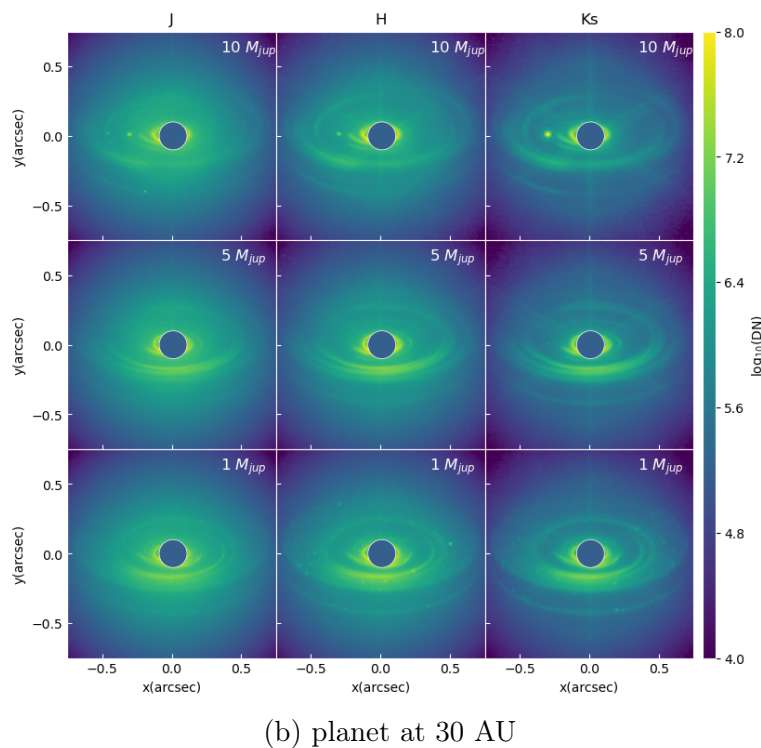
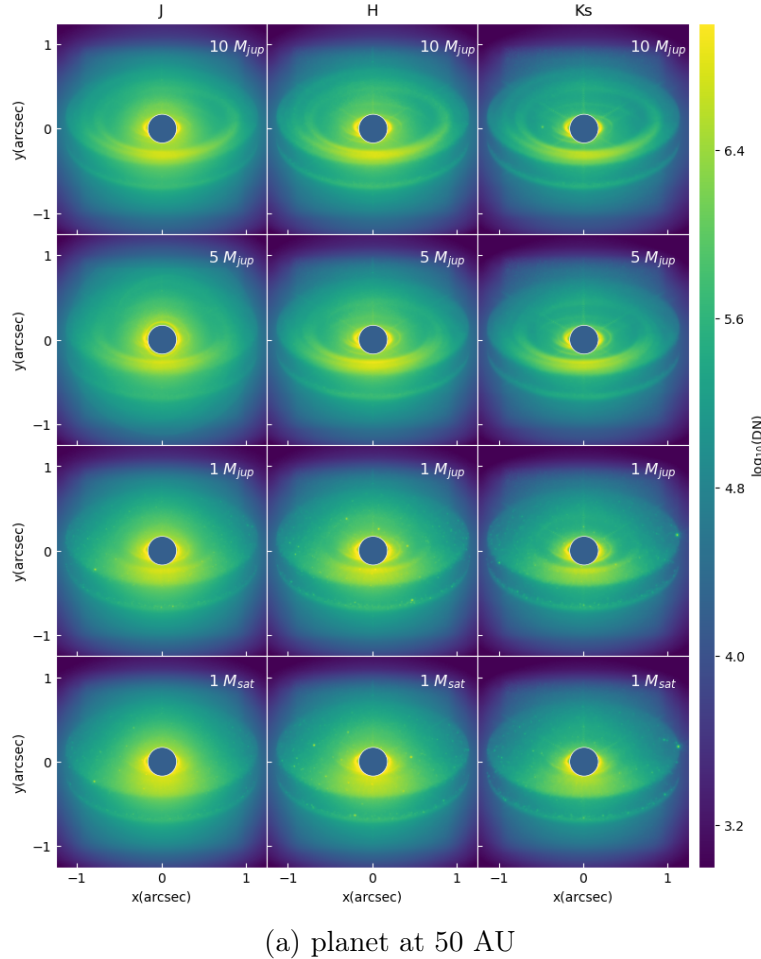


Table 5.5: Circumplanetary disk fluxes and magnitudes at 100 pc as imaged by ELT/MICADO. Columns named **CPD** reports the CPD flux subtracted by background noise, whereas **CPD only** reports CPD flux minus the flux of the CSD 180° across the planet, i.e. the anti-CPD flux. SNR_{CPD} values are given by the ratio between CPD flux (without subtraction) and anti-CPD flux.

model	filter	CPD (Jy)	CPD only (Jy)	CPD (mag)	CPD only (mag)	SNR_{CPD}
10jup50au	J	1.09e-05	4.41e-07	20.41	23.89	1.04
	H	3.32e-03	3.31e-03	13.77	13.78	304.30
	Ks	1.79e-02	1.79e-02	11.40	11.40	1881.39
5jup50au	J	1.10e-05	1.43e-07	20.40	25.11	1.01
	H	1.19e-05	1.58e-08	19.89	27.08	/
	Ks	1.33e-05	1.68e-07	19.23	23.97	1.01
1jup50au	J	1.20e-05	/	20.31	/	/
	H	1.33e-05	/	19.77	/	/
	Ks	1.51e-05	/	19.09	/	/
1sat50au	J	1.28e-05	/	20.23	/	/
	H	1.52e-05	/	19.62	/	/
	Ks	1.76e-05	2.32e-07	18.92	23.63	1.01
10jup30au	J	7.69e-03	7.66e-03	13.29	13.29	279.55
	H	4.95e-03	4.92e-03	13.34	13.35	181.85
	Ks	2.69e-02	2.69e-02	10.96	10.96	1697.78
5jup30au	J	3.13e-05	/	19.26	/	/
	H	2.96e-05	/	18.90	/	/
	Ks	1.63e-04	1.37e-04	16.51	16.69	6.29
1jup30au	J	3.45e-05	1.84e-06	19.16	22.34	1.06
	H	3.51e-05	4.79e-06	18.71	20.88	1.16
	Ks	3.49e-05	7.55e-06	18.18	19.84	1.28

Figure 5.13: Simulated METIS observations in 0° inclination at 100 pc. The columns represent the 3 filters simulated, and the rows represent models with different planetary masses. The planet is always at 9 o'clock direction on the images. The central star is masked with a circle. The color scale is unit of \log_{10} DN.

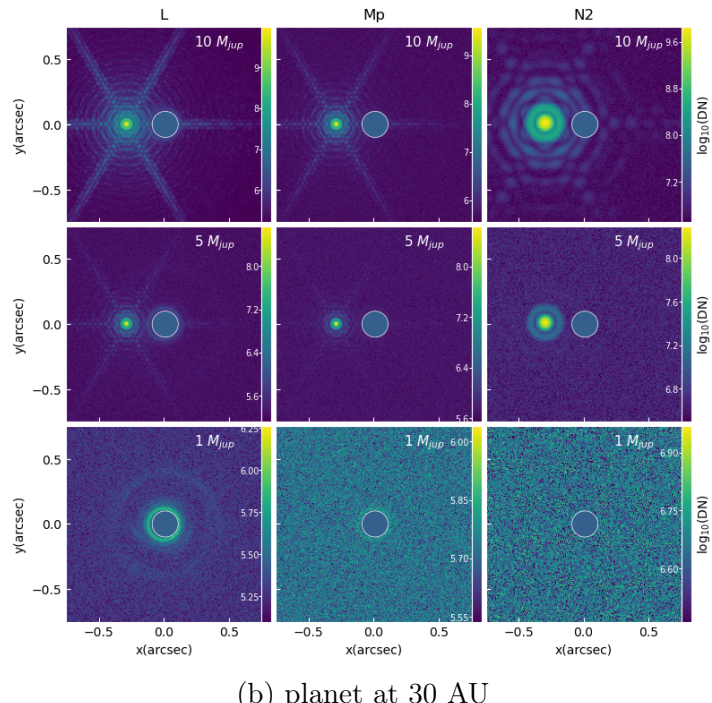
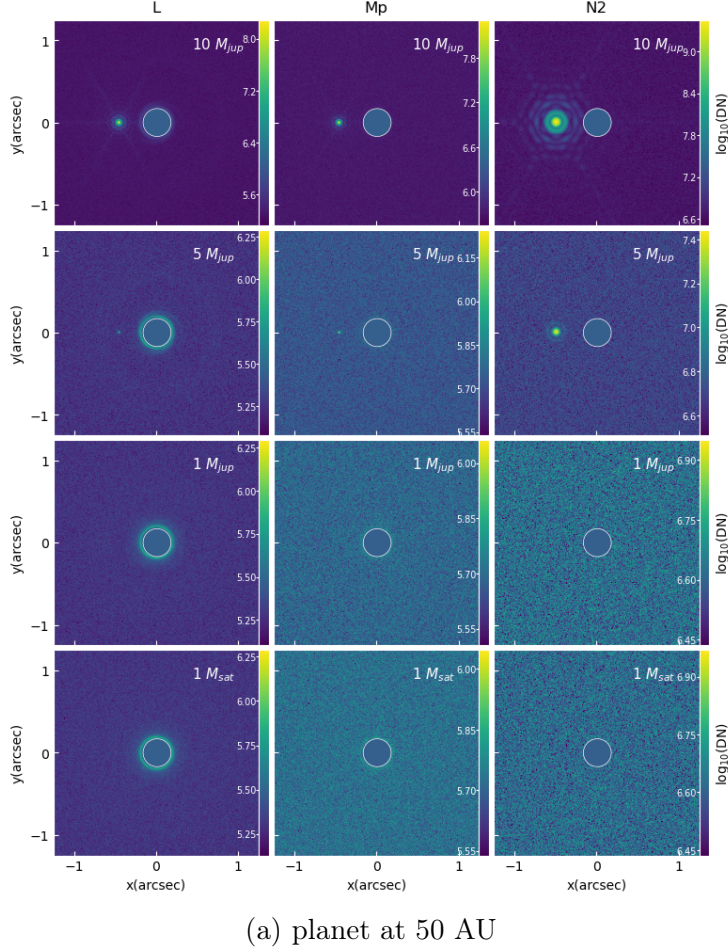
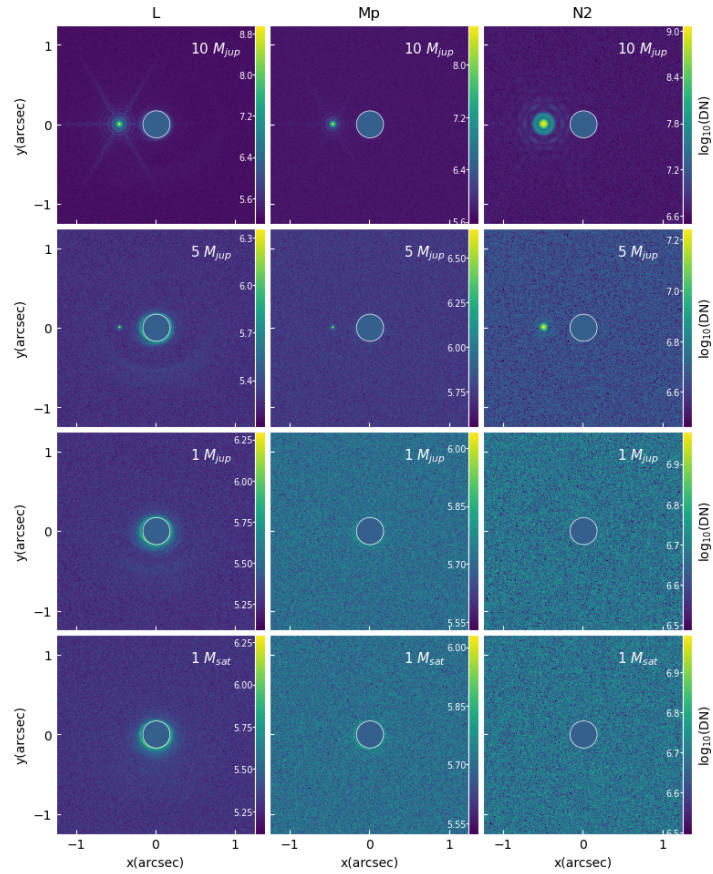
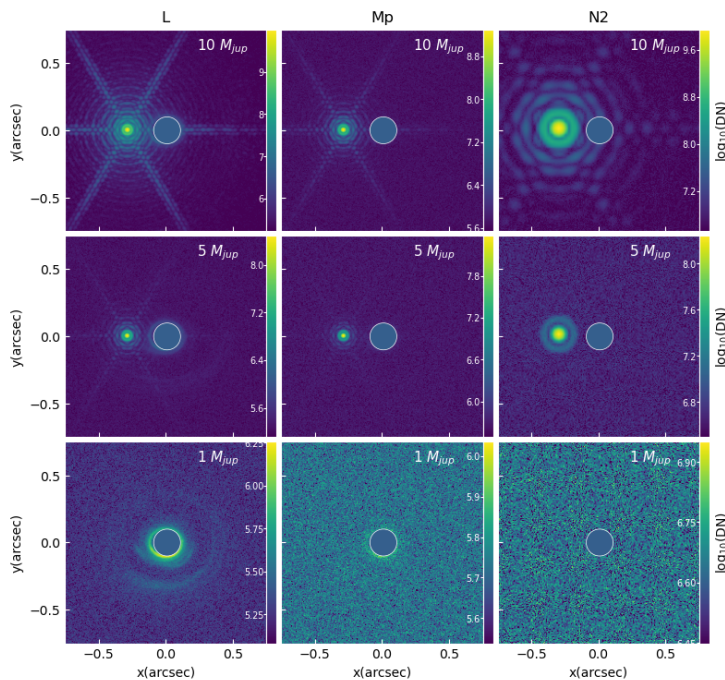


Figure 5.14: Simulated METIS observations, same as Fig 5.13 but in 30° inclination.

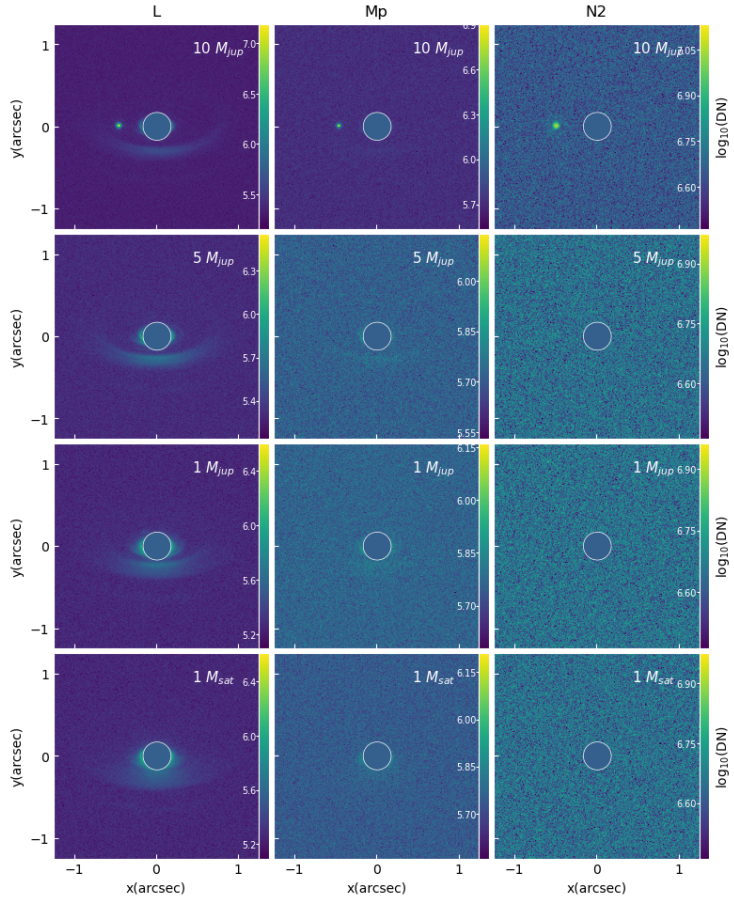


(a) planet at 50 AU

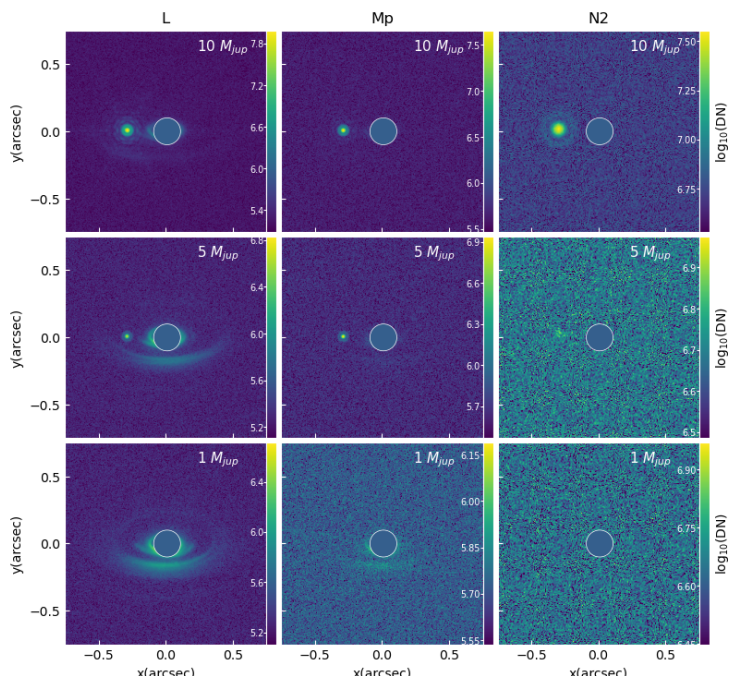


(b) planet at 30 AU

Figure 5.15: Simulated METIS observations, same as Fig 5.13 but in 60° inclination.



(a) planet at 50 AU



(b) planet at 30 AU

Table 5.6: Circumplanetary disk fluxes and magnitudes at 100 pc as imaged by ELT/METIS. Columns named **CPD** reports the CPD flux subtracted by background noise, whereas **CPD only** reports CPD flux minus the flux of the CSD 180° across the planet, i.e. the anti-CPD flux. SNR_{CPD} values are given by the ratio between CPD flux (without subtraction) and anti-CPD flux.

model	filter	CPD (Jy)	CPD only (Jy)	CPD (mag)	CPD only (mag)	SNR_{CPD}
10jup50au	L	2.65e-04	2.65e-04	14.95	14.95	1251.44
	Mp	5.32e-04	5.31e-04	13.63	13.63	466.04
	N2	1.01e-02	1.01e-02	8.85	8.85	4448.16
5jup50au	L	7.09e-07	7.93e-07	21.38	21.26	8.46
	Mp	2.73e-06	2.50e-06	19.35	19.44	11.78
	N2	8.30e-05	7.74e-05	14.06	14.14	14.83
1jup50au	L	2.22e-07	/	22.64	/	/
	Mp	/	/	/	/	/
	N2	/	/	/	/	/
1sat50au	L	1.62e-07	/	22.98	/	/
	Mp	/	/	/	/	/
	N2	8.31e-06	1.30e-06	16.56	18.57	1.19
10jup30au	L	1.26e-02	1.26e-02	10.76	10.76	2700.95
	Mp	9.89e-03	9.88e-03	10.45	10.45	2335.46
	N2	2.58e-02	2.58e-02	7.83	7.83	804.55
5jup30au	L	6.89e-04	6.89e-04	13.91	13.91	2130.91
	Mp	1.08e-03	1.08e-03	12.86	12.86	885.18
	N2	6.72e-04	6.77e-04	11.79	11.78	124.08
1jup30au	L	1.27e-07	7.35e-08	23.25	23.84	2.38
	Mp	/	/	/	/	/
	N2	6.88e-06	1.58e-06	16.76	18.36	1.30

Figure 5.16: Simulated GMTIFS observations in 0° inclination at 100 pc. The columns represent the 3 filters simulated, and the rows represent models with different planetary masses. The planet is always at 9 o'clock direction on the images. The central star is masked with a circle. The color scale is unit of \log_{10} DN.

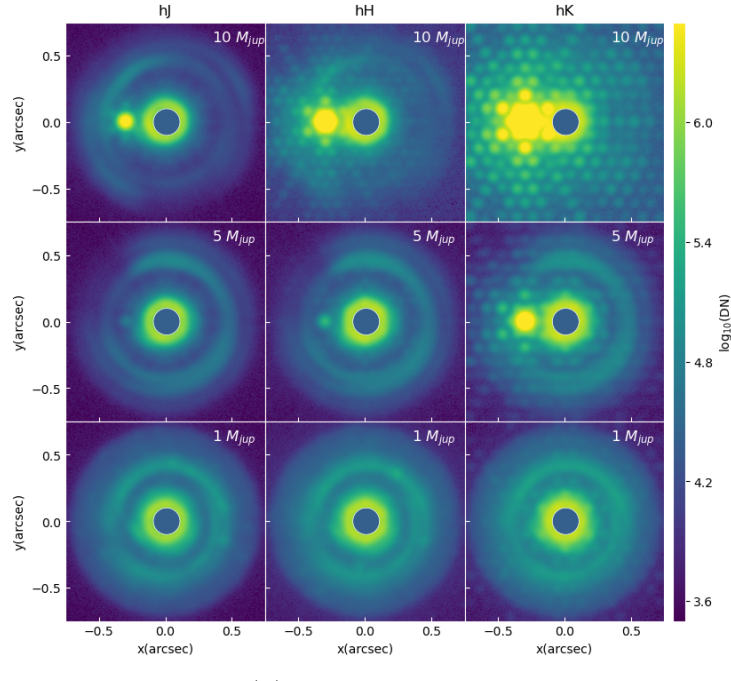
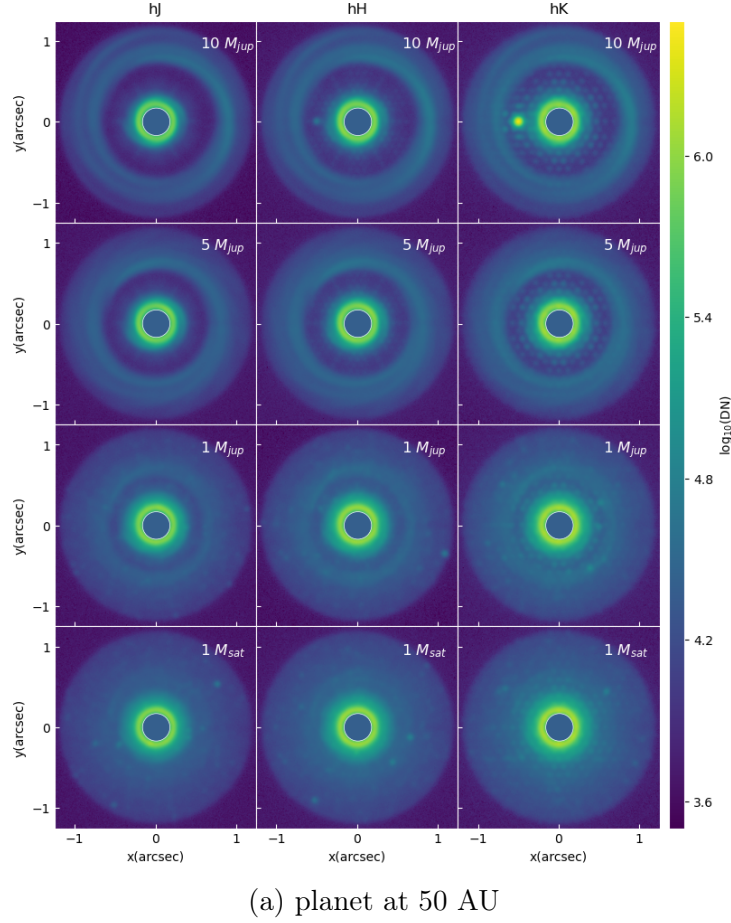


Figure 5.17: Simulated GMTIFS observations, same as Fig 5.16 but in 30° inclination.

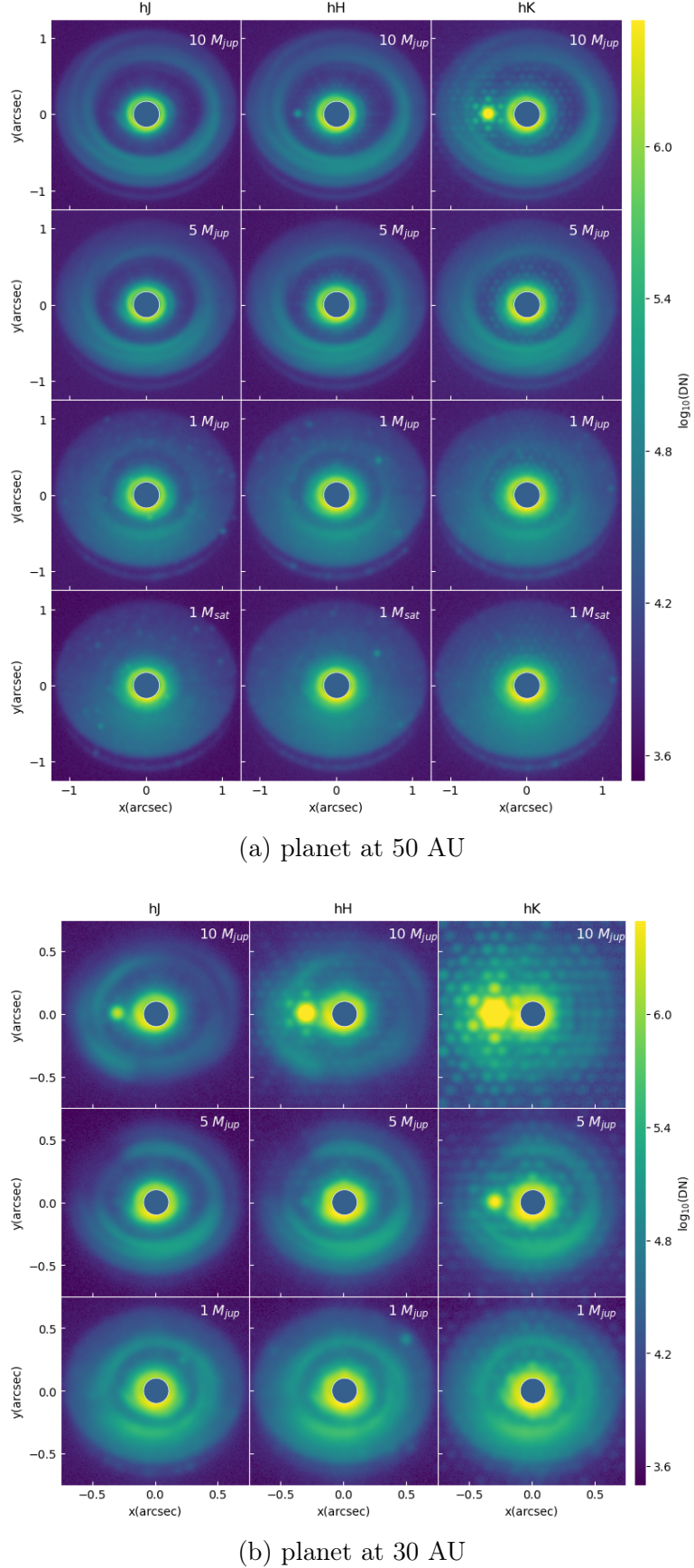
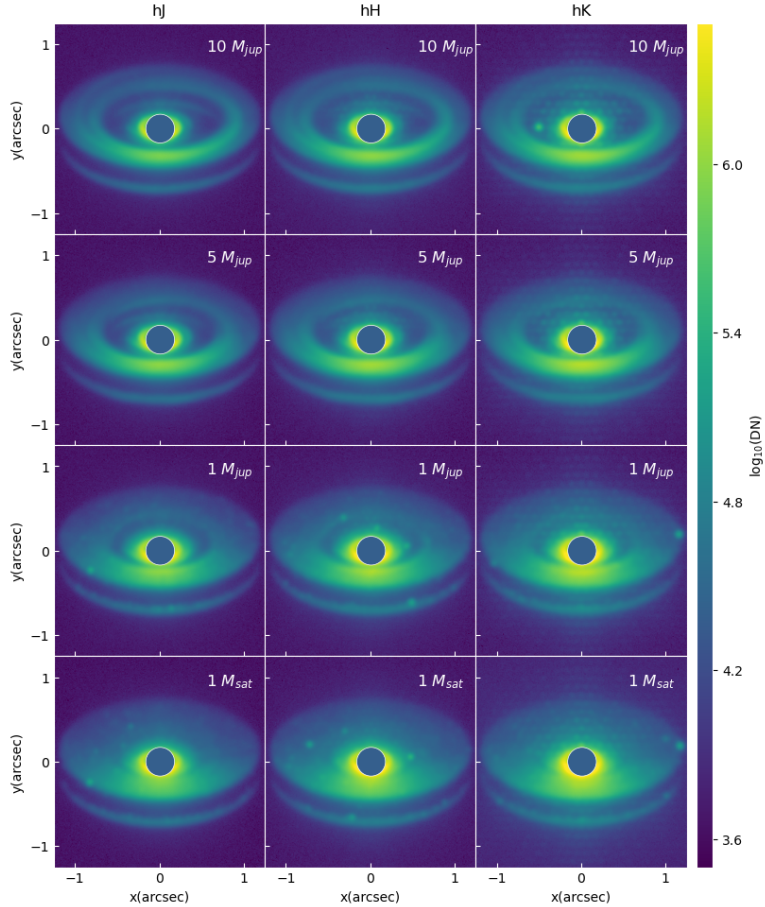
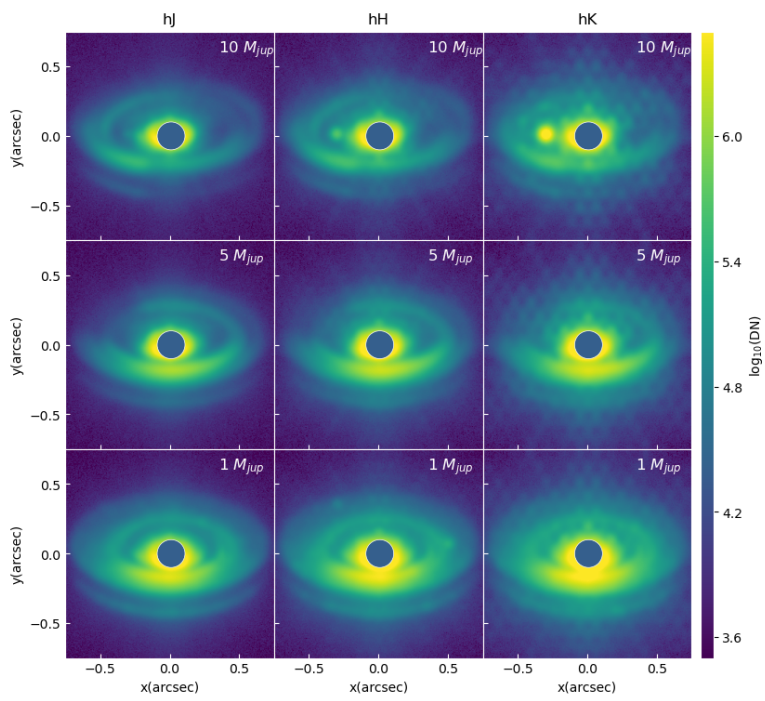


Figure 5.18: Simulated GMTIFS observations, same as Fig 5.16 but in 60° inclination.



(a) planet at 50 AU



(b) planet at 30 AU

Table 5.7: Circumplanetary disk fluxes and magnitudes at 100 pc as imaged by GMTIFS. Columns named **CPD** reports the CPD flux subtracted by background noise, whereas **CPD only** reports CPD flux minus the flux of the CSD 180° across the planet, i.e. the anti-CPD flux. SNR_{CPD} values are given by the ratio between CPD flux (without subtraction by anti-CPD) and anti-CPD flux.

model	filter	CPD (Jy)	CPD only (Jy)	CPD (mag)	CPD only (mag)	SNR_{CPD}
10jup50au	hJ	1.61e-07	2.83e-08	24.99	26.87	1.21
	hH	1.32e-06	1.02e-06	22.28	22.56	4.40
	hK	1.04e-04	1.04e-04	16.99	17.00	158.31
5jup50au	hJ	1.47e-07	3.97e-09	25.08	29.00	1.03
	hH	3.53e-07	/	23.71	/	/
	hK	6.80e-07	/	22.46	/	/
1jup50au	hJ	3.00e-07	/	24.31	/	/
	hH	6.93e-07	/	22.98	/	/
	hK	1.33e-06	/	21.73	/	/
1sat50au	hJ	4.69e-07	/	23.82	/	/
	hH	1.04e-06	/	22.54	/	/
	hK	2.02e-06	2.18e-08	21.27	26.19	1.01
10jup30au	hJ	1.53e-04	1.53e-04	17.54	17.54	323.96
	hH	2.26e-03	2.26e-03	14.19	14.19	1702.31
	hK	1.46e-02	1.46e-02	11.63	11.63	3184.99
5jup30au	hJ	1.13e-06	5.49e-07	22.87	23.65	1.94
	hH	9.95e-06	8.69e-06	20.08	20.23	7.92
	hK	9.52e-04	9.50e-04	14.59	14.59	361.75
1jup30au	hJ	1.39e-06	3.22e-07	22.64	24.23	1.30
	hH	2.80e-06	6.67e-07	21.46	23.02	1.31
	hK	4.69e-06	6.79e-07	20.36	22.46	1.17

Chapter 6

Conclusion

In this thesis, the observability of forming planets is studied with five instruments on near-future telescopes. We used the results from JUPITER hydrodynamic simulations followed by radiative post-processing as the input to the telescope simulators, and created synthetic observed images from each instrument in a wide range of wavelengths from near-IR to mid-IR. From these simulated images, we calculated the predicted flux and magnitudes of the observed circumplanetary disk with embedded planet.

We found that planets with high planetary mass ($> 5 M_{jup}$) are observable by all instruments in most filters, even some cases with 60° inclination. The planet signal increases with longer wavelength and closer separation from its star. NIRCam and NIRISS are able to detect $10 M_{jup}$ planets in all of their filters with face-on geometry, and detect $5 M_{jup}$ planets above $3 \mu\text{m}$. For wavelengths $< 2 \mu\text{m}$, NIRCam has an advantage over NIRISS due to its higher spatial resolution. MIRI can detect 10- and 5- Jupiter mass planets in all its filters, and even able to detect signal from 1-Jupiter mass planets beyond $15 \mu\text{m}$. However, MIRI observation are limited by its resolution, which makes it unable to resolve the planet from the star clearly. On the other hand, METIS benefits from its ground-based large mirror and is able to resolve 30/50 AU planets in mid IR. Like MIRI, it can also detect 10- and 5- Jupiter mass planets in all its filters, but it does not have channels longer than $15 \mu\text{m}$, making it unable to image 1 Jupiter mass planets, for which longer wavelengths are required. MICADO, METIS and GMTIFS offers a high resolution that allows disk features such as accretion spirals onto the planet to be resolved. These features can indicate the existence of an embedded planet even if it is buried inside optically thick dusts. MICADO and GMTIFS both images in 0.9-2.5 μm . For planet at 50 AU, they both can only detect $10 M_{jup}$ planets in H and K band. For 30 AU separation, MICADO can detect $10 M_{jup}$ planets in all bands and $5 M_{jup}$ planet only in K band, while GMTIFS can detect 10 and $5 M_{jup}$ planets in all bands.

Comparing the result from all bands, we conclude that for the near-IR instruments, the best observability of forming planets is achieved towards longer wavelengths, which are F356W and F444W for NIRCam & NIRISS, and K band for MICADO and GMTIFS. The visibility of forming planet is particularly poor in J band. For these short wavelengths, polarized scattered light imaging is needed for

CPD observation. Among all the near-IR instruments, NIRCam covers the widest wavelength range and enables most detections with its high sensitivity, while yielding good resolution. In the mid IR, METIS will provide high resolution imaging that allows resolved CPD detection around $10\ \mu\text{m}$, and MIRI will bring unique chances to image planet forming disks in $15\text{-}25\ \mu\text{m}$, where the contrast of lower-mass giant planets is better.

Calculated fluxes for the same planetary mass in same wavelength varies for different instrument. While the difference between NIRCam and NIRISS is small, the discrepancy can be 1-3 mags for planets at 30 AU and up to 7-8 mags for planets at 50 AU. The difference can be caused by instrument properties themselves, and also by the different inner working of the instrument simulators and flux conversion errors. The SNR value as a criterion for detection also depends on the instrument. In general, we found that a $\text{SNR} > 2$ already indicate a detection, and SNR values between 1-2 require careful inspection on the image to confirm the detection. The SNR value required for detection is lower than the usual object vs background noise detection due to the particularity of the science problem, which is to detect the CPD signal on top of the background CSD.

Further works are expected to be continued from this thesis. To distinguish between the flux from CPD region and from the planet only, cut-outs of the hydrodynamic fields will be performed. Different cut-out settings will enable the contribution of CSD, CPD and planet to be studied separately, and draw conclusions on the effect of extinction by the CSD and CPD. SEDs are also to be made with the full system and different cut-outs. The continuation of this thesis is expected to result in a published paper.

Acknowledgement

I would like to thank my supervisor Prof. Judit Szulágyi for offering me the opportunity to work on this thesis in her group. I would like to thank her for always being so responsible and supportive during our time working together. I learned a lot from her timely and detailed explanations on my questions. Her motivation and great passion for astronomy have deeply inspired me.

I would also like to thank Pablo Rutschmann, who worked on the JUPITER to RADMC3D conversion pipeline in collaboration with me. Without his codes, this thesis could not have been completed.

I would like to thank the Department of Physics at ETH Zürich, the Institute of Particle Physics and Astrophysics and especially the IT services group for their support during my thesis and my master study in general.

Last but not least, I would like to thank my parents, Mrs. Wu and Mr. Chen for their continuous support. I would like to thank my friend K. W., who gave me endless emotional support during the hard times and made Zurich feel like home.

Bibliography

- Andrews, S. M., Huang, J., Pérez, L. M., Isella, A., Dullemond, C. P., Kurtovic, N. T., Guzmán, V. V., Carpenter, J. M., Wilner, D. J., Zhang, S., Zhu, Z., Birnstiel, T., Bai, X.-N., Benisty, M., Hughes, A. M., Åberg, K. I., & Ricci, L. (2018). The disk substructures at high angular resolution project (DSHARP). i. motivation, sample, calibration, and overview. *The Astrophysical Journal*, *869*(2), L41.
URL <https://doi.org/10.3847/2041-8213/aaf741>
- Ansdell, M., Williams, J. P., Manara, C. F., Miotello, A., Facchini, S., van der Marel, N., Testi, L., & van Dishoeck, E. F. (2017). An ALMA Survey of Protoplanetary Disks in the σ Orionis Cluster. , *153*(5), 240.
- Ayliffe, B. A., & Bate, M. R. (2009). Gas accretion on to planetary cores: three-dimensional self-gravitating radiation hydrodynamical calculations. , *393*(1), 49–64.
- Ayliffe, B. A., & Bate, M. R. (2012). The growth and hydrodynamic collapse of a protoplanet envelope. , *427*(3), 2597–2612.
- Bell, K. R., & Lin, D. N. C. (1994). Using FU Orionis Outbursts to Constrain Self-regulated Protostellar Disk Models. , *427*, 987.
- Benisty, M., Bae, J., Facchini, S., Kepler, M., Teague, R., Isella, A., Kurtovic, N. T., Pérez, L. M., Sierra, A., Andrews, S. M., Carpenter, J., Czekala, I., Dominik, C., Henning, T., Menard, F., Pinilla, P., & Zurlo, A. (2021). A circumplanetary disk around PDS70c. *The Astrophysical Journal Letters*, *916*(1), L2.
URL <https://doi.org/10.3847/2041-8213/ac0f83>
- Bitsch, B., Crida, A., Morbidelli, A., Kley, W., & Dobbs-Dixon, I. (2013). Stellar irradiated discs and implications on migration of embedded planets - i. equilibrium discs. *A&A*, *549*, A124.
URL <https://doi.org/10.1051/0004-6361/201220159>
- Bohren, C. F., & Huffman, D. R. (1984). Book-Review - Absorption and Scattering of Light by Small Particles. , *307*, 575.
- Boss, A. P. (1997). Giant planet formation by gravitational instability. *Science*, *276*, 1836–1839.

- Brandl, B., Bettonvil, F., van Boekel, R., Glauser, A., Quanz, S., Absil, O., Amorim, A., Feldt, M., Glasse, A., Güdel, M., Ho, P., Labadie, L., Meyer, M., Pantin, E., van Winckel, H., & METIS Consortium (2021). METIS: The Mid-infrared ELT Imager and Spectrograph. *The Messenger*, 182, 22–26.
- Conan, R., Bennet, F., Bouchez, A. H., van Dam, M. A., Espeland, B., Gardhouse, W., D'Orgeville, C., Parcell, S., Piatrou, P., Price, I., Rigaut, F., Tranco, G., & Uhlendorf, K. (2012). The Giant Magellan Telescope laser tomography adaptive optics system. In B. L. Ellerbroek, E. Marchetti, & J.-P. Véran (Eds.) *Adaptive Optics Systems III*, vol. 8447 of *Society of Photo-Optical Instrumentation Engineers (SPIE) Conference Series*, (p. 84473P).
- Davies, R., & Genzel, R. (2010). MICADO: The Multi-adaptive Optics Imaging Camera for Deep Observations. *The Messenger*, 140, 32–33.
- de Juan Ovelar, M., Min, M., Dominik, C., Thalmann, C., Pinilla, P., Benisty, M., & Birnstiel, T. (2013). Imaging diagnostics for transitional discs. , 560, A111.
- Dong, R., Fung, J., & Chiang, E. (2016). HOW SPIRALS AND GAPS DRIVEN BY COMPANIONS IN PROTOPLANETARY DISKS APPEAR IN SCATTERED LIGHT AT ARBITRARY VIEWING ANGLES. *The Astrophysical Journal*, 826(1), 75.
URL <https://doi.org/10.3847/0004-637x/826/1/75>
- Dong, R., Hall, C., Rice, K., & Chiang, E. (2015a). SPIRAL ARMS IN GRAVITATIONALLY UNSTABLE PROTOPLANETARY DISKS AS IMAGED IN SCATTERED LIGHT. *The Astrophysical Journal*, 812(2), L32.
URL <https://doi.org/10.1088/2041-8205/812/2/132>
- Dong, R., Zhu, Z., & Whitney, B. (2015b). OBSERVATIONAL SIGNATURES OF PLANETS IN PROTOPLANETARY DISKS. i. GAPS OPENED BY SINGLE AND MULTIPLE YOUNG PLANETS IN DISKS. *The Astrophysical Journal*, 809(1), 93.
URL <https://doi.org/10.1088/0004-637x/809/1/93>
- Ertel, S., Wolf, S., & Rodmann, J. (2012). Observing planet-disk interaction in debris disks. , 544, A61.
- Isella, A., Benisty, M., Teague, R., Bae, J., Keppler, M., Facchini, S., & Pérez, L. (2019). Detection of continuum submillimeter emission associated with candidate protoplanets. *The Astrophysical Journal*, 879(2), L25.
URL <https://doi.org/10.3847/2041-8213/ab2a12>
- Isella, A., & Turner, N. J. (2018). Signatures of young planets in the continuum emission from protostellar disks. *The Astrophysical Journal*, 860(1), 27.
URL <https://doi.org/10.3847/1538-4357/aabb07>

Keppler, Benisty, M., Müller, A., Henning, Th., van Boekel, R., Cantalloube, F., Ginski, C., van Holstein, R. G., Maire, A.-L., Pohl, A., Samland, M., Avenhaus, H., Baudino, J.-L., Boccaletti, A., de Boer, J., Bonnefoy, M., Chauvin, G., Desidera, S., Langlois, M., Lazzoni, C., Marleau, G.-D., Mordasini, C., Pawellek, N., Stolker, T., Vigan, A., Zurlo, A., Birnstiel, T., Brandner, W., Feldt, M., Flock, M., Girard, J., Gratton, R., Hagelberg, J., Isella, A., Janson, M., Juhasz, A., Kemmer, J., Kral, Q., Lagrange, A.-M., Launhardt, R., Matter, A., Ménard, F., Milli, J., Mollière, P., Olofsson, J., Pérez, L., Pinilla, P., Pinte, C., Quanz, S. P., Schmidt, T., Udry, S., Wahhaj, Z., Williams, J. P., Buenzli, E., Cudel, M., Dominik, C., Galicher, R., Kasper, M., Lannier, J., Mesa, D., Mouillet, D., Peretti, S., Perrot, C., Salter, G., Sissa, E., Wildi, F., Abe, L., Antichi, J., Augereau, J.-C., Baruffolo, A., Baudoz, P., Bazzon, A., Beuzit, J.-L., Blanchard, P., Brems, S. S., Buey, T., De Caprio, V., Carillet, M., Carle, M., Cascone, E., Cheetham, A., Claudi, R., Costille, A., Delboulbé, A., Dohlen, K., Fantinel, D., Feautrier, P., Fusco, T., Giro, E., Gluck, L., Gry, C., Hubin, N., Hugot, E., Jaquet, M., Le Mignant, D., Llored, M., Madec, F., Magnard, Y., Martinez, P., Maurel, D., Meyer, M., Möller-Nilsson, O., Moulin, T., Mugnier, L., Origné, A., Pavlov, A., Perret, D., Petit, C., Pragt, J., Puget, P., Rabou, P., Ramos, J., Rigal, F., Rochat, S., Roelfsema, R., Rousset, G., Roux, A., Salasnich, B., Sauvage, J.-F., Sevin, A., Soenke, C., Stadler, E., Suarez, M., Turatto, M., & Weber, L. (2018). Discovery of a planetary-mass companion within the gap of the transition disk around pds 70. *A&A*, 617, A44.

URL <https://doi.org/10.1051/0004-6361/201832957>

Kley, W. (1999). Mass flow and accretion through gaps in accretion discs. , 303(4), 696–710.

Kraus, A. L., & Ireland, M. J. (2011). LkCa 15: A YOUNG EXOPLANET CAUGHT AT FORMATION? *The Astrophysical Journal*, 745(1), 5.

URL <https://doi.org/10.1088/0004-637x/745/1/5>

Leschinski, K., Czoske, O., KÄ¶hler, R., Mach, M., Zeilinger, W., Verdoes Kleijn, G., Alves, J., Kausch, W., & Przybilla, N. (2016). Simcado: an instrument data simulator package for micado at the e-elt. *Modeling, Systems Engineering, and Project Management for Astronomy VI*.

URL <http://dx.doi.org/10.1117/12.2232483>

Lubow, S. H., & D'Angelo, G. (2006). Gas Flow across Gaps in Protoplanetary Disks. , 641(1), 526–533.

Mayor, M., & Queloz, D. (1995). A Jupiter-mass companion to a solar-type star. , 378(6555), 355–359.

McGregor, P. J., Bloxham, G. J., Boz, R., Davies, J., Doolan, M., Ellis, M., Hart, J., Jones, D. J., Luval, L., Nielsen, J., Parcell, S., Sharp, R., Stevanovic, D., & Young, P. J. (2012). GMT integral-field spectrograph (GMTIFS) conceptual design. In I. S. McLean, S. K. Ramsay, & H. Takami (Eds.) *Ground-based and*

Airborne Instrumentation for Astronomy IV, vol. 8446 of *Society of Photo-Optical Instrumentation Engineers (SPIE) Conference Series*, (p. 84461I).

Mesa, Keppler, M., Cantalloube, F., Rodet, L., Charnay, B., Gratton, R., Langlois, M., Boccaletti, A., Bonnefoy, M., Vigan, A., Flasseur, O., Bae, J., Benisty, M., Chauvin, G., de Boer, J., Desidera, S., Henning, T., Lagrange, A.-M., Meyer, M., Milli, J., Müller, A., Pairet, B., Zurlo, A., Antoniucci, S., Baudino, J.-L., Brown Sevilla, S., Cascone, E., Cheetham, A., Claudi, R. U., Delorme, P., D’Orazi, V., Feldt, M., Hagelberg, J., Janson, M., Kral, Q., Lagadec, E., Lazzoni, C., Ligi, R., Maire, A.-L., Martinez, P., Menard, F., Meunier, N., Perrot, C., Petrus, S., Pinte, C., Rickman, E. L., Rochat, S., Rouan, D., Samland, M., Sauvage, J.-F., Schmidt, T., Udry, S., Weber, L., & Wildi, F. (2019). Vlt/sphere exploration of the young multiplanetary system pds70. *A&A*, *632*, A25.

URL <https://doi.org/10.1051/0004-6361/201936764>

Palla, F. (1996). *The Quest for Evolutionary Diagrams of Young Stellar Objects (Review)*, vol. 465, (p. 143).

Perez, S., Dunhill, A., Casassus, S., Roman, P., Szulágyi, J., Flores, C., Marino, S., & Montesinos, M. (2015). PLANET FORMATION SIGNPOSTS: OBSERVABILITY OF CIRCUMPLANETARY DISKS VIA GAS KINEMATICS. *The Astrophysical Journal*, *811*(1), L5.

URL <https://doi.org/10.1088/2041-8205/811/1/15>

Pollack, J. B., Hubickyj, O., Bodenheimer, P., Lissauer, J. J., Podolak, M., & Greenzweig, Y. (1996). Formation of the Giant Planets by Concurrent Accretion of Solids and Gas. , *124*(1), 62–85.

Quanz, S. P., Amara, A., Meyer, M. R., Girard, J. H., Kenworthy, M. A., & Kasper, M. (2015). Confirmation and Characterization of the Protoplanet HD 100546 b—Direct Evidence for Gas Giant Planet Formation at 50 AU. , *807*(1), 64.

Quillen, A. C., & Trilling, D. E. (1998). Do Proto-jovian Planets Drive Outflows? , *508*(2), 707–713.

Reggiani, M., Christiaens, V., Absil, O., Mawet, D., Huby, E., Choquet, E., Gomez Gonzalez, C. A., Ruane, G., Femenia, B., Serabyn, E., Matthews, K., Barraza, M., Carlomagno, B., Defrère, D., Delacroix, C., Habraken, S., Jolivet, A., Karlsson, M., Orban de Xivry, G., Piron, P., Surdej, J., Vargas Catalan, E., & Wertz, O. (2018). Discovery of a point-like source and a third spiral arm in the transition disk around the Herbig Ae star MWC 758. , *611*, A74.

Reggiani, M., Quanz, S. P., Meyer, M. R., Pueyo, L., Absil, O., Amara, A., Anglada, G., Avenhaus, H., Girard, J. H., Gonzalez, C. C., Graham, J., Mawet, D., Meru, F., Milli, J., Osorio, M., Wolff, S., & Torrelles, J.-M. (2014). DISCOVERY OF a COMPANION CANDIDATE IN THE HD 169142 TRANSITION DISK AND THE POSSIBILITY OF MULTIPLE PLANET FORMATION. *The Astrophysical*

- Journal*, 792(1), L23.
URL <https://doi.org/10.1088/2041-8205/792/1/123>
- Sallum, S., Follette, K. B., Eisner, J. A., Close, L. M., Hinz, P., Kratter, K., Males, J., Skemer, A., Macintosh, B., Tuthill, P., Bailey, V., Defrère, D., Morzinski, K., Rodigas, T., Spalding, E., Vaz, A., & Weinberger, A. J. (2015). Accreting protoplanets in the LkCa 15 transition disk. , 527(7578), 342–344.
- Sanchis, E., Picogna, G., Ercolano, B., Testi, L., & Rosotti, G. (2020). Detectability of embedded protoplanets from hydrodynamical simulations. , 492(3), 3440–3458.
- Shakura, N. I., & Sunyaev, R. A. (1973). Reprint of 1973A&A....24..337S. Black holes in binary systems. Observational appearance. , 500, 33–51.
- Sharp, R., Bloxham, G., Boz, R., Bundy, D., Davies, J., Espeland, B., Fordham, B., Hart, J., Herrald, N., Nielsen, J., Vaccarella, A., Vest, C., Young, P., & McGregor, P. (2016). GMTIFS: The Giant Magellan Telescope integral fields spectrograph and imager. In C. J. Evans, L. Simard, & H. Takami (Eds.) *Ground-based and Airborne Instrumentation for Astronomy VI*, vol. 9908 of *Society of Photo-Optical Instrumentation Engineers (SPIE) Conference Series*, (p. 99081Y).
- Szulágyi, J., Dullemond, C. P., Pohl, A., & Quanz, S. P. (2019). Observability of forming planets and their circumplanetary discs II. à SEDs and near-infrared fluxes. *Monthly Notices of the Royal Astronomical Society*, 487(1), 1248–1258.
- Szulágyi, J., & Garufi, A. (2021). Observability of forming planets and their circumplanetary discs - III. Polarized scattered light in near-infrared. , 506(1), 73–83.
- Szulágyi, J., Masset, F., Lega, E., Crida, A., Morbidelli, A., & Guillot, T. (2016). Circumplanetary disc or circumplanetary envelope? *Monthly Notices of the Royal Astronomical Society*, 460(3), 2853–2861.
URL <https://doi.org/10.1093/mnras/stw1160>
- Szulágyi, J., Morbidelli, A., Crida, A., & Masset, F. (2014). ACCRETION OF JUPITER-MASS PLANETS IN THE LIMIT OF VANISHING VISCOSITY. *The Astrophysical Journal*, 782(2), 65.
URL <https://doi.org/10.1088/0004-637x/782/2/65>
- Szulágyi, J., Plas, G. v. d., Meyer, M. R., Pohl, A., Quanz, S. P., Mayer, L., Daemgen, S., & Tamburello, V. (2017). Observability of forming planets and their circumplanetary discs à I. Parameter study for ALMA. *Monthly Notices of the Royal Astronomical Society*, 473(3), 3573–3583.
- Toomre, A. (1964). On the gravitational stability of a disk of stars. , 139, 1217–1238.
- Wolf, S., & D'Angelo, G. (2005). On the observability of giant protoplanets in circumstellar disks. *The Astrophysical Journal*, 619(2), 1114–1122.
URL <https://doi.org/10.1086/426662>

Wolszczan, A., & Frail, D. A. (1992). A planetary system around the millisecond pulsar PSR1257 + 12. , *355*(6356), 145–147.

Zhang, S., Zhu, Z., Huang, J., Guzmán, V. V., Andrews, S. M., Birnstiel, T., Dullemond, C. P., Carpenter, J. M., Isella, A., Pérez, L. M., Benisty, M., Wilner, D. J., Baruteau, C., Bai, X.-N., & Ricci, L. (2018). The disk substructures at high angular resolution project (DSHARP). VII. the planet–disk interactions interpretation. *The Astrophysical Journal*, *869*(2), L47.

URL <https://doi.org/10.3847/2041-8213/aaf744>

Declaration of originality

The signed declaration of originality is a component of every semester paper, Bachelor's thesis, Master's thesis and any other degree paper undertaken during the course of studies, including the respective electronic versions.

Lecturers may also require a declaration of originality for other written papers compiled for their courses.

I hereby confirm that I am the sole author of the written work here enclosed and that I have compiled it in my own words. Parts excepted are corrections of form and content by the supervisor.

Title of work (in block letters):

Authored by (in block letters):

For papers written by groups the names of all authors are required.

Name(s):

First name(s):

With my signature I confirm that

- I have committed none of the forms of plagiarism described in the '[Citation etiquette](#)' information sheet.
- I have documented all methods, data and processes truthfully.
- I have not manipulated any data.
- I have mentioned all persons who were significant facilitators of the work.

I am aware that the work may be screened electronically for plagiarism.

Place, date

Signature(s)

Xuejing Chen

For papers written by groups the names of all authors are required. Their signatures collectively guarantee the entire content of the written paper.